

## Review of sensing and actuation technologies – from optical MEMS and nanophotonics to photonic nanosystems

Yiming Ma, Weixin Liu, Xinmiao Liu, Nan Wang & Hui Zhang

**To cite this article:** Yiming Ma, Weixin Liu, Xinmiao Liu, Nan Wang & Hui Zhang (2024) Review of sensing and actuation technologies – from optical MEMS and nanophotonics to photonic nanosystems, International Journal of Optomechatronics, 18:1, 2342279, DOI: [10.1080/15599612.2024.2342279](https://doi.org/10.1080/15599612.2024.2342279)

**To link to this article:** <https://doi.org/10.1080/15599612.2024.2342279>



© 2024 The Author(s). Published with license by Taylor & Francis Group, LLC



Published online: 07 May 2024.



[Submit your article to this journal](#)



Article views: 1684



[View related articles](#)



[View Crossmark data](#)



Citing articles: 3 [View citing articles](#)

# Review of sensing and actuation technologies – from optical MEMS and nanophotonics to photonic nanosystems

Yiming Ma<sup>a</sup>, Weixin Liu<sup>b,c</sup>, Xinmiao Liu<sup>b,c</sup>, Nan Wang<sup>a</sup>, and Hui Zhang<sup>d</sup>

<sup>a</sup>School of Microelectronics, Shanghai University, Shanghai, P. R. China; <sup>b</sup>Department of Electrical and Computer Engineering, National University of Singapore, Singapore; <sup>c</sup>Center for Intelligent Sensors and MEMS (CISM), National University of Singapore, Singapore; <sup>d</sup>Department of Electrical and Electronic Engineering, The Hong Kong Polytechnic University, Hong Kong, P. R. China

## ABSTRACT





Entering the era of the Internet of Things (IoT) and fifth-generation (5G) mobile networks, the demand for compact, cost-effective, and high-performance sensors and actuators is skyrocketing. Optical technologies as complements to conventional electrical technologies provide a versatile platform to construct sensors and actuators for widespread applications, showing advantages of high data rate, strong multiplexing capability, fast response, low crosstalk, and immunity to electromagnetic interference. In this paper, we provide a comprehensive review of the development progress of optical sensing and actuation technologies. Their applications in optical detectors, optical sensors (further divided into physical and chemical/biological sensors), and optical communication/computing/imaging are presented. For each category of the applications, progress is introduced following the technology evolution trend from optical microelectromechanical systems (MEMS) and nanophotonics to photonic nanosystems. Future development directions of optical sensing/actuation technologies are also proposed.

## KEYWORDS

Sensors; actuators; optical MEMS; nanophotonics; photonic nanosystems

## 1. Introduction

The rapid development of the Internet of Things (IoT) and fifth-generation (5G) mobile networks is inseparable from a large number of miniature, low-cost, and high-performance sensors and actuators.<sup>[1]</sup> While most sensors and actuators work in the electrical domain,<sup>[2,3]</sup> optical sensors and actuators, where the sensory information and/or the transmitted signal are in the optical domain, become promising complementary techniques.<sup>[4,5]</sup> The boost of IoT and 5G has drastically increased the data volume and thus the requirement of sensors and actuators regarding data processing capability.<sup>[6,7]</sup> However, electronic devices have reached a bottleneck in data rate due to the physical limitation of metallic interconnects. Optical (in particular photonic) devices utilize photons as the information carrier, which allows much higher data rates than electrons. The data transmission bottleneck posted by metallic interconnects can be effectively removed by using optical interconnects, which strongly promotes the development of optical communication and

**CONTACT** Yiming Ma  [yimingma@shu.edu.cn](mailto:yimingma@shu.edu.cn)  School of Microelectronics, Shanghai University, Shanghai, P. R. China; Hui Zhang  [hui-jovie.zhang@polyu.edu.hk](mailto:hui-jovie.zhang@polyu.edu.hk)  Department of Electrical and Electronic Engineering, The Hong Kong Polytechnic University, Hong Kong, P. R. China.

Yiming Ma, Weixin Liu, and Xinmiao Liu contributed equally to this work.

© 2024 The Author(s). Published with license by Taylor & Francis Group, LLC

This is an Open Access article distributed under the terms of the Creative Commons Attribution License (<http://creativecommons.org/licenses/by/4.0/>), which permits unrestricted use, distribution, and reproduction in any medium, provided the original work is properly cited. The terms on which this article has been published allow the posting of the Accepted Manuscript in a repository by the author(s) or with their consent.

## Nomenclature

THz	Terahertz	CD	Circular dichroism
$\alpha_r$	Seebeck coefficient	RCP	Right circular polarized
$\Delta T$	Temperature gradient	LCP	Left circular polarized
$R_{th}$	Thermal resistance	ASIC	Application-specific integrated circuit
$C_{th}$	Heat capacity	FPGA	Field-programmable gate array
$\tau_{th}$	Thermal time constant	MZM	Mach-Zehnder mesh
Q	Quality	PCM	Phase change material
ppm/K	Parts per million per K	GST	Germanium-antimony-tellurides
$M_p$	Effective mass of the metallic pillars	T-TENG	Textile-based triboelectric nanogenerators
$F_c$	Coriolis force	THMI	Triboelectric-human-machine interface
$\Omega_z$	Out-plane rotation	MVM	Matrix-vector multiplication
$v_p$	Longitudinal vibration velocity	DOF	Degrees of freedom
MEMS	Micro-electro-mechanical system	OPA	Optical phased array
IoT	Internet of Things	FoV	Field of view
5G	Fifth-generation	FPSA	Focal plane switch array
MOEMS	Micro-opto-electro-mechanical systems	IMF	Interfacial misfit
Si	Silicon	2D	Two-dimensional
CMOS	Complementary metal-oxide-semiconductor	3D	Three-dimensional
PIC	Photonic integrated circuit	hBN	Hexagonal boron nitride
NEMS	Nano-electro-mechanical systems	UV	Ultraviolet
IR	Infrared	TMD	Transition metal dichalcogenide
MIR	Mid-infrared	BP	Black phosphorus
TCR	Temperature coefficient of resistance	NUS	National University of Singapore
$VO_x$	Vanadium oxide	BPVE	Bulk photovoltaic effect
YbCuO	Yttrium barium copper oxide	TBG	Twisted bilayer graphene
ZnO	Zinc oxide	TDBG	Twisted double bilayer graphene
$TiO_2$	Titanium dioxide	CNN	Convolutional neural network
LWIR	Long-wavelength infrared	BCB	Benzocyclobutene
NEP	Noise-equivalent power	PhCWG	Photonic crystal waveguide
$VO_2$	Vanadium dioxide	SWGWG	Subwavelength grating waveguide
MIM	Metal-insulator-metal	MRR	Micro-ring resonator
TCF	Temperature coefficient of frequency	PCB	Printed circuit board
AlN	Aluminum nitride	FP	Fabry-Pérot
$SiO_2$	Silicon dioxide	PVA	Polyvinyl Alcohol
SNR	Signal-to-noise ratio	PCN	Photonic crystal nanobeam
NIR	Near-infrared	WGM	Whispering gallery mode
Ge	Germanium	SWG	Subwavelength grating
SiGe	Silicon-Germanium	RI	Refractive index
MSM	Metal-semiconductor-metal	$CH_4$	Methane
APD	Avalanche photodetector	$C_8H_{10}$	Xylene
Sn	Tin	$C_7H_9N$	N-methylaniline
DFSL	Dislocation filter superlattice	SOI	Silicon-on-insulator
PCA	Principal component analysis	SNOI	Silicon nitride-on-insulator
SVM	Supporting vector machine	BOX	Buried oxide
RF	Radio frequency	SOS	Silicon-on-sapphire
AO	Acousto-optic	SOCF	Silicon-on-calcium fluoride
MZI	Mach-Zehnder interferometer	GOS	Germanium-on-silicon
SAW	Surface acoustic wave	LoD	Limit of detection
NOEMS	Nano-opto-electro-mechanical system	NDIR	Non-dispersive infrared
vdW	Van der Waals	TDLAS	Tuneable diode laser absorption spectroscopy
PDMS	Polydimethylsiloxane	SEIRA	Surface-enhanced infrared absorption
GSG	Ground-signal-ground	MOF	Metal-organic framework
LiDAR	Light detection and ranging	PEI	Polyethyleneimine
VOA	Variable optical attenuator	PTFE	Polytetrafluoroethylene
PZT	Lead zirconate titanate	AI	Artificial intelligence
SRR	Split ring resonator	HNA	Hook nanoantenna
eSRR	Electrical split ring resonator	WMHNA	Wavelength-multiplexed HNA

computing.<sup>[8–10]</sup> Meanwhile, imaging is important for various IoT applications and naturally suitable to be realized by optical techniques, as the processed signal is in the optical domain.<sup>[11]</sup> At the same time, the use of optical techniques for sensing applications is getting increasing attention because the transmitted optical signal is sensitive to various external stimuli. Compared with traditional electrical sensors, optical sensors provide advantages of fast response, low crosstalk, strong detection multiplexing capability, and immunity to electromagnetic interference.<sup>[12]</sup> Despite the impressive advancement of optical techniques and their widespread applications, to date, the transmitted optical signal normally still needs to be converted to electrical one and then treated and analyzed by well-developed and commercialized electrical instruments. Therefore, optical detectors that transform the optical signal into electrical realm are indispensable.<sup>[13]</sup>

Micro-electro-mechanical system (MEMS) devices (including sensors and actuators) fabricated with microfabrication technology possess the merits of tiny size (typically feature size is at micro or sub-micro level), ease of integration, low cost, and low power consumption. Since their emergence around the 1960s, they have been widely used in many fields.<sup>[4,14]</sup> The first use of MEMS to process (sense or manipulate) optical signals appeared in the late 1970s.<sup>[15,16]</sup> This has now become a thriving field known as optical MEMS, sometimes also called micro-opto-electro-mechanical systems (MOEMS) especially when micro-optics are combined with MEMS.<sup>[17,18]</sup> Following the prosperity of optical MEMS and micro-optics, nanophotonics has attracted great research interests, in which light is confined and interacts with matters at the nanoscale, leading to higher device compactness and on-chip integration capability as well as stronger light-matter interaction.<sup>[19]</sup> Over the past two decades, nanophotonics, especially silicon (Si) nanophotonics, has been intensively developed because of its promising potential to meet the increasing demands for high data transmission capacity.<sup>[20]</sup> One key driving force of Si nanophotonics is the fabrication compatibility with the mature complementary metal-oxide-semiconductor (CMOS) technology, which enables the manufacturing of photonic integrated circuits (PICs) at low costs and high volumes.<sup>[8]</sup> Up to date, the commercialization of Si nanophotonics has been witnessed.<sup>[21]</sup> Nowadays, photonic nanosystems have emerged as an important development direction for optical technologies. Photonic nanosystems feature not only the integration of nanophotonic passive and active components for on-chip operation but also the combination of nanophotonics with other technologies including micro/nano-electro-mechanical systems (MEMS/NEMS), micro/nanofluidics, micro/nanoelectronics, and cutting-edge techniques such as wearable electronics for more functionalities.<sup>[22–25]</sup> The technology evolution trend from optical MEMS to nanophotonics and then to photonic nanosystems has been observed in the development of optical detectors, optical sensors, and optical devices for communication, computing, and imaging applications, as illustrated in Figure 1.<sup>[26–40]</sup>

In this paper, we review the progress of sensing and actuation technologies in the optical domain. The paper is organized according to the applications of optical technologies, i.e., optical detectors, optical sensors (further divided into physical sensors and chemical/biological sensors), and optical communication, computing, and imaging, in sequence. For each category of the applications, progress is reviewed following the technology evolution trend from optical MEMS and nanophotonics to photonic nanosystems. Various representative and pioneering works are enumerated with detailed introductions of their device configurations, working mechanisms, and applications. In the end, we conclude the development of optical technologies and their applications to date and provide our points of view on their future development directions.

## 2. Optical detectors

As discussed above, optical detectors are pivotal optoelectronic components of optical systems for practical applications. Optical detectors make use of different light-induced effects that are readable through electrical measurements. The most widely used optical detection mechanisms are

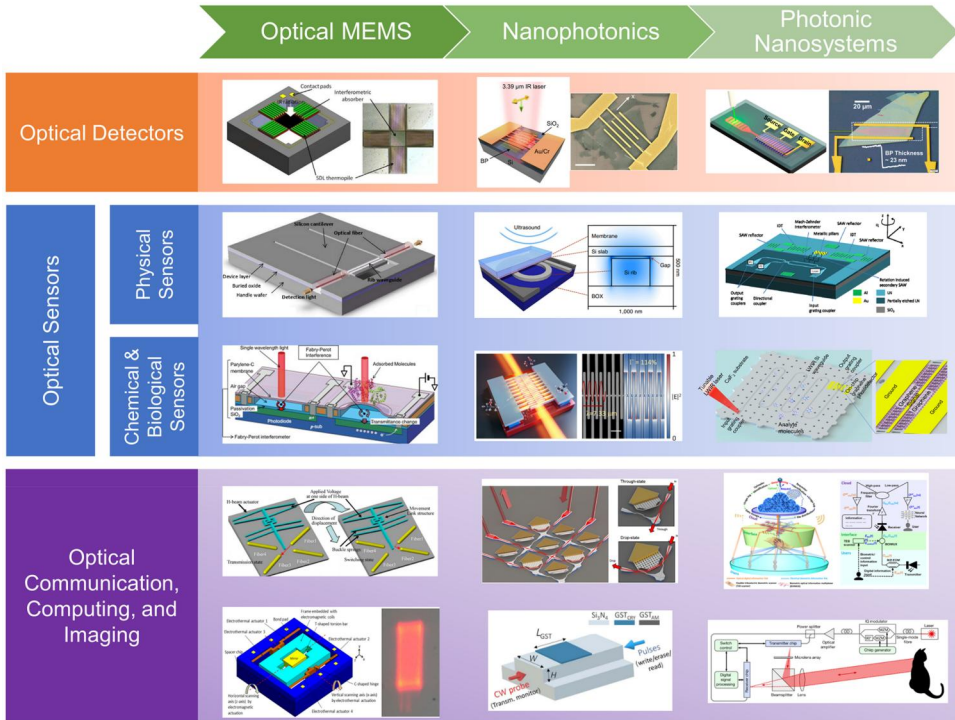


**Figure 1.** Development roadmap of optical sensing and actuation technologies: from optical MEMS and nanophotonics to photonic nanosystems. Reproduced with permissions from Refs. [26–40]

classified according to the nature of the physical effect caused by the incident radiation: in photon-type detectors, the radiation is absorbed within the material by interaction with electrons bound to either lattice atoms or impurity atoms or with free electrons, and the observed electrical output signal results from the changed electronic energy distribution; while in thermal-type detectors, the incident radiation is absorbed to change the material temperature, and the resultant change in some physical property is used to generate an electrical output.<sup>[41]</sup> In this section, both types of detectors are reviewed.

## 2.1. MEMS-based thermal detectors

Thermal effects, depending on the radiant power instead of the photonic nature of the incident radiation, are typically wavelength-independent. Thus, most of the thermal detectors are operated in a wide wavelength range, covering both infrared (IR) and terahertz (THz) spectrum.<sup>[42]</sup> Due to this heating mechanism, the thermal detectors are typically in a suspended configuration that is connected to a heat sink for better heating efficiency. While photon detectors usually require cryogenic cooling for long-wavelength (low-energy) photon detection, thermal detectors are typically uncooled IR sensors that allow for more cost-effective and compact systems.<sup>[41]</sup> MEMS techniques have been widely adopted to construct miniature thermal detectors. Several mechanisms are leveraged to realize radiation thermal detection, including thermoelectric, bolometric, and pyroelectric effects. Thermopile is a group of serial-connected thermocouples formed by two materials with different Seebeck coefficients. The radiation-induced temperature difference between the hot junction and the cold junction will generate thermoelectric voltage, enabling the thermopile-based IR sensor a passive sensor without active



operation power.<sup>[43,44]</sup> The induced thermoelectric voltage  $V_{\text{out}}$  by the temperature gradient  $\Delta T$  is provided as:

$$V_{\text{out}} = N\alpha_r\Delta T \quad (1)$$

where  $N$  is the number of connected thermocouples, and  $\alpha_r$  is the Seebeck coefficient. In recent years thermopiles have undergone the common trend of miniaturization, thus, higher Seebeck coefficients CMOS-compatible materials have been explored to maintain the thermal efficiency in the  $\mu\text{m}$ -scale. Meanwhile, the high-temperature characteristics of thermopiles are also extensively explored, as most of the other IR sensors including bolometers and quantum sensors cannot work properly at high temperatures, which is, nevertheless, required in applications such as oil gas detection. In 2015, Zhou et al. explored polycrystalline Si-based mid-infrared (MIR) thermopile with a CMOS-compatible fabrication process and for high-temperature applications, with the device configuration depicted in Figure 2(a).<sup>[26]</sup> The fabricated thermopile gives the maximum output voltage of 0.59 mV at an ambient temperature of 190 °C and at a wavelength of 3.9  $\mu\text{m}$ , where the responsivity and the detectivity are derived as 425.7 V/W and  $1.25 \times 10^7 \text{ cm}\cdot\text{Hz}/\text{W}$ , respectively.

Bolometers are another kind of the most common thermal sensor that operates by changing the resistance of the sensing layer upon absorbing the IR radiation. The change of the resistance in bolometers then can be detected in an electrical output signal. In such a way, it is desired to adopt bolometric materials with a high-temperature coefficient of resistance (TCR). Currently, several high TCR bolometric materials have been explored for uncooled bolometer applications, among which,  $\text{VO}_x$  and amorphous Si are the most common and well-explored materials with TCR values of about  $-2$  to  $-4\%/K$ .<sup>[45,46]</sup> Other materials such as polycrystalline Si, YbCuO, ZnO,  $\text{TiO}_2$ , carbon nanotubes, and graphene, are also being explored for their suitability as thermal-sensing materials.<sup>[47–51]</sup> To enable bolometers with high detection sensitivity, different device

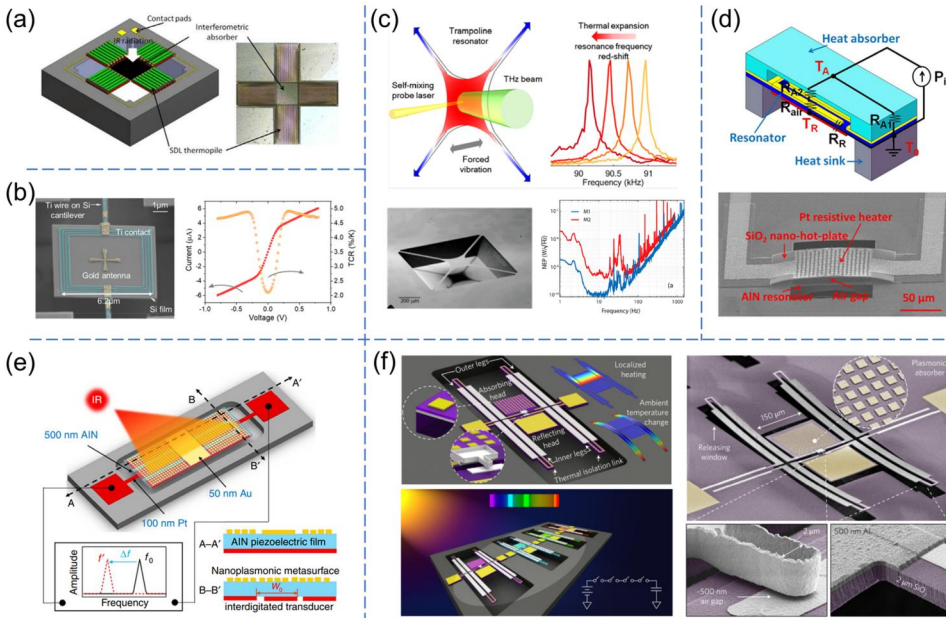


**Figure 2.** MEMS-based thermal detectors. (a) MEMS MIR thermopile. Reproduced with permission from Ref.<sup>[26]</sup>; (b) fast microbolometer for LWIR light detection. Reproduced with permission from Ref.<sup>[56]</sup>; (c) microbolometer for sub-THz detection at room temperature. Reproduced with permission from Ref.<sup>[57]</sup>; (d) AlN piezoelectric resonator-based thermal detector with integrated suspended heat absorbing element. Reproduced with permission from Ref.<sup>[63]</sup>; (e) Plasmonic piezoelectric resonator for spectrally selective IR sensing. Reproduced with permission from Ref.<sup>[66]</sup>; (f) zero-power IR event-based switch. Reproduced with permission from Ref.<sup>[68]</sup>

architectures and various fabrication techniques have been adopted to improve thermal insulation. Generally, thermal insulation in microbolometers can be achieved through two configurations. One is the one-level configuration that consists of a free-standing active membrane supported by thermal insulating legs with sufficient mechanical support but a long thermal conducting path. The other is two-level configurations that fabricate the microbolometers over the electronic circuits with vertical thermal insulating legs. Typically, bolometers in two-level configuration possess a much larger fill factor compared to those in one-level configuration, making two-level bolometers widely adopted for commercial IR focal plane arrays.<sup>[52,53]</sup> To reduce the thermal conductance and improve the sensitivity, thermal isolation structures, which should be robust, compact, and facile to fabricate, are desired. One kind of approach is to maximize the thermal resistance of the device for better thermal isolation. Nevertheless, a large thermal resistance ( $R_{th}$ ) with a high heat capacity ( $C_{th}$ ) also leads to large thermal time constant ( $\tau_{th} = R_{th}C_{th}$ ) values even up to  $\sim 10$  ms.<sup>[54,55]</sup> Consequently, the operating frequencies of most existing bolometers are limited to well below 1 kHz. Further improvement of operation speed requires a low heat capacity in bolometers. Chen et al. developed a microbolometer based on a suspended Si membrane and plasmonic antenna with an ultrasmall heat capacity and high TCR targeting for the long-wavelength infrared (LWIR) range imaging solution, as shown in Figure 2(b).<sup>[56]</sup> The only 220 nm thick membrane results in a small  $C_{th}$ , which further leads to a  $\tau_{th}$  of less than 16  $\mu$ s, over 500 times smaller than that of typical commercial ones. The corresponding operation bandwidth of the microbolometer extends up to 10 kHz. Due to the plasmonic enhancement, the microbolometer exhibits a high peak extrinsic responsivity of 114 mA/W with an active area size of only 6.2  $\mu$ m by 6.2  $\mu$ m. Recently, researchers also brought a bolometer into the application for THz radiation detection, aiming to be the next candidate for cheap THz imaging and relative potential applications. Leonardo et al. developed micromechanical bolometers based on SiN trampoline membranes as broad-range detectors down to sub-THz frequencies, as presented in Figure 2(c).<sup>[57]</sup> The device is based on a Si<sub>3</sub>N<sub>4</sub> trampoline with a 35 nm-thick Cr-Au coating. The heat generated by the absorbed radiation will induce a thermal expansion of the vibrating structure, which further shifts the resonance frequency of the micromechanical resonator bolometer. This device achieved a minimum noise-equivalent power (NEP) of  $\sim 100$  pW·Hz<sup>-1/2</sup> and a detection speed of 40 Hz. On top of this demonstration, addition of VO<sub>2</sub> metasurfaces and metal-insulator-metal (MIM) structures may further increase the device responsivity in the THz range.<sup>[58,59]</sup>

In the past decade, due to the advance of piezoelectric MEMS/NEMS and their mature infrastructures, mechanically resonant thermal sensors have been rapidly developed as a competitive candidate for high-resolution uncooled thermal detections. Principally, piezoelectric resonant sensors with intrinsic high quality (Q) factors and using frequency as the output variable, have advantages including ultra-high sensitivity to the external stimulations and extremely low noise performance.<sup>[60–62]</sup> The resonance frequency is a function of temperature and is given by the temperature coefficient of frequency (TCF)

$$\alpha_T = \frac{1}{f(T)} \frac{\partial f}{\partial T} \quad (2)$$

where  $f(T)$  is the relation between the resonant frequency and the temperature. And the TCF is generally expressed in parts per million per K (ppm/K). This equation allows us to translate the incident thermal radiation to a perceptible frequency shift. Similar to thermopiles and bolometers, good thermal isolation is also required in resonant thermal detectors for a high TCF. As one of the most well-developed piezoelectric materials, aluminum nitride (AlN), which is also highly temperature sensitive, is suitable for the demonstration of high-performance IR thermal detectors. In 2013, Hui et al. presented a miniaturized, fast, and high-resolution AlN thermal detector, as shown in Figure 2(d).<sup>[63]</sup> A SiO<sub>2</sub> heat absorber and a temperature-sensitive AlN nano-plate resonator are perfectly overlapped but separated by a microscale air gap. Thanks to this compact

integration, a fast ( $\sim 10 \mu\text{s}$ ) heat transfer from the absorber to the piezoelectric resonator was achieved and enabled high-resolution thermal power detection (several nW). With the demonstrated low noise performance and high Q factor, the piezoelectric resonator shows great potential for the implementation of fast and high-resolution uncooled thermal detectors. The insufficient light concentration in planer structures with deep subwavelength thickness was also a bottleneck in the development of high-performance resonant IR detectors, due to the lack of highly absorbing materials compatible with standard microfabrication processes and efficient transduction techniques. Fortunately, plasmonic enhancement by metamaterials can also be integrated into resonant sensors for unprecedented absorption efficiency.<sup>[64,65]</sup> As shown in Figure 2(e), Hui et al. proposed a nanomechanical resonator with an integrated plasmonic metasurface to simultaneously tailor electromechanical and optical properties.<sup>[66]</sup> In the proposed resonator, AlN piezoelectric nanoplate functions as both the MIM structure for radiation absorption and the lateral-extensional mode resonator. An array of subwavelength nanoantennas is periodically patterned within the top metal electrode of the device, with its resonant frequency well-designed to maximize its absorption within the spectrum of interest. The authors experimentally demonstrated  $\sim 80\%$  absorption for an optimized spectral bandwidth centered around  $8.8 \mu\text{m}$ , presenting a high thermomechanical coupling between electromagnetic and mechanical resonances in a single ultrathin piezoelectric nanoplate and selective detection of LWIR radiation.

With the advances of IoT and the massive requirements for low-power sensor nodes, it is highly desired to develop sensors with near-zero power consumption. That is, the sensors remain dormant until awakened by a specific physical signature associated with an event of interest, therefore, it can greatly extend the sensor lifetime and result in low costs of deployment and maintenance of unattended sensor networks.<sup>[4,7,67]</sup> In 2017, Qian et al. demonstrated IR digitizing sensors by leveraging micromechanical photoswitches activated by selectively harvested electromagnetic energy, as presented in Figure 2(f).<sup>[68]</sup> The sensors consist of two symmetric released cantilevers with two biomaterial legs. Two membranes were integrated into the center of cantilevers, with one coated by a plasmonic absorber and the other one coated by a gold reflector. The absorbing membrane also carries a Pt tip, while the reflecting membrane carries a contact pad, which is separated by a 500 nm air gap. When IR light with a specific wavelength is received, the temperature will increase and induce a downward bending of the metal tip. While the absorbed IR power exceeds the design threshold, the metal tip will contact the contact pad and turn on the switch. Such zero-power IR sensors that combine zero standby power consumption and a low threshold, can passively monitor the environment until awakened by a specific IR spectral signal with an event of interest and are necessary for the development of wide-deployed sensor networks for IoT applications.

## 2.2. Free-space photodetectors using nanophotonic technologies

Following the development of MEMS-based optical detectors, on-chip detectors are being developed using nanophotonic technologies. Optical detectors of this category were first designed as discrete free-space devices integrated on Si substrates. Unlike MEMS-based detectors which are mostly thermal-type, detectors based on nanophotonic technologies are typically photon-type. In photon-type detectors, efficient photocarrier generation depends on the bandgap of the active material. Photon-type detectors provide overall better performance relative to the thermal type, including higher signal-to-noise ratio (SNR) and faster response.<sup>[69]</sup>

Si has a large indirect bandgap of 1.12 eV, which hampers efficient light detection at attractive near-infrared (NIR) and MIR wavelengths beyond  $1.1 \mu\text{m}$ . Germanium (Ge) has proved to be an excellent complement to Si in modern electronic chips, and the same is seen in chip-scale nanophotonics. Unlike Si, Ge has a quasi-direct energy bandgap of 0.8 eV (corresponding to  $1.55 \mu\text{m}$  wavelength). The moderate 4.2% lattice mismatch between Ge ( $a_{\text{Ge}} = 5.658 \text{ \AA}$ ) and Si ( $a_{\text{Si}} =$



5.431 Å) enables Ge epitaxy on Si. Mainly two approaches have been developed to grow high-quality Ge epitaxial films on Si.<sup>[70]</sup> One is to use a graded SiGe buffer layer to reduce the threading dislocation density in the Ge layer on top, and the other is to directly grow Ge on Si with a two-step deposition technique, in which a thin Ge buffer layer is firstly grown at low temperature to suppress islanding, followed by a high-temperature Ge growth with higher growth rates and better crystal quality. The two-step Ge growth method typically results in a tensile strain of about 0.2%, which shrinks the direct bandgap of Ge, resulting in stronger absorption at 1.55  $\mu\text{m}$  as well as a longer cutoff wavelength.<sup>[71]</sup> These two approaches can be combined, i.e., using SiGe buffer layers before the two-step growth, for better growth quality.<sup>[72]</sup> Since the start of the 21st century, numerous Ge photodetectors integrated on Si substrates with metal-semiconductor-metal (MSM) or p-i-n diode structures have been demonstrated (Figure 3(a)).<sup>[73–76]</sup> In addition, various cutting-edge Ge-on-Si photodetectors have been developed over the past decade, including avalanche photodetectors (APDs) to detect low signal intensities,<sup>[77,78]</sup> photodetectors capable of handling high-power levels,<sup>[79]</sup> as well as photodetectors beyond the Ge cutoff wavelength by alloying Ge with semimetallic Tin (Sn).<sup>[80]</sup> For more details on Ge-on-Si photodetectors, we refer readers to dedicated sources.<sup>[70,81,82]</sup>

Notwithstanding the recent notable developments, GeSn photodetectors are still facing serious limitations. Extending the cutoff wavelength requires increasing Sn composition, which is hindered by the increasing lattice mismatch between GeSn and Si, the low solid solubility of Sn in Ge and Si, and the low thermal stability of GeSn.<sup>[83]</sup> The longest working wavelength of reported GeSn photodetectors is 3.65  $\mu\text{m}$ .<sup>[80]</sup> Currently, the mainstream for MIR (2–20  $\mu\text{m}$ ) photodetection is still narrow-bandgap III-V and II-VI compounds. Nonetheless, their lattice constants are mostly larger than 6 Å, resulting in even larger lattice mismatches with Si as compared to Ge.<sup>[84]</sup> Heterogeneous integration of III-V and II-VI photodetectors on Si substrates is generally by direct epitaxial growth or via bonding techniques.<sup>[85]</sup> For direct epitaxial growth, several delicate methods have been employed together with the common buffer layer method to accommodate

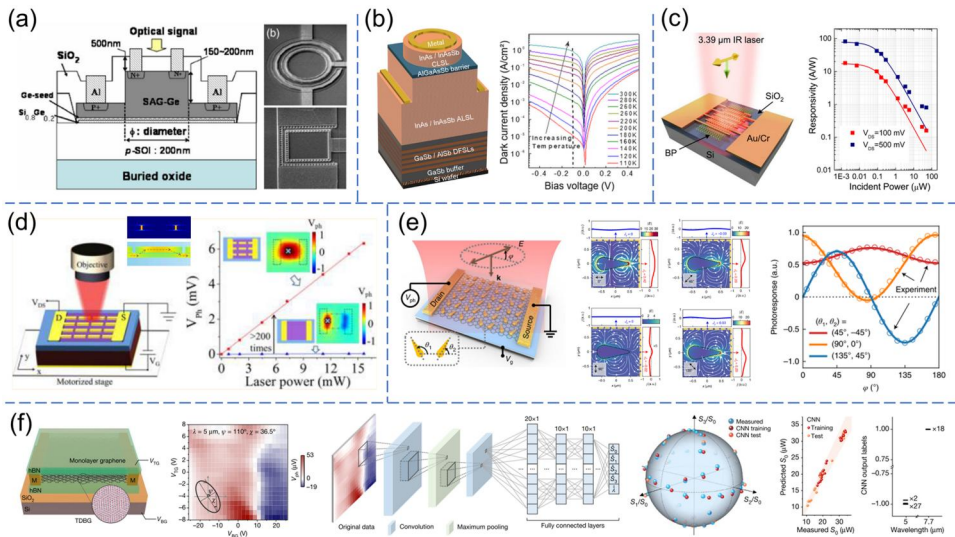


**Figure 3.** Free-space photodetectors using nanophotonic technologies. (a) NIR photodetector based on Ge epitaxy on Si substrate using SiGe buffer layer before two-step growth. Reproduced with permission from Ref.<sup>[76]</sup>; (b) MIR photodetector based on direct epitaxial growth of III-V compounds on Si substrate with lattice mismatch compensation by IMF array, buffer layer, and DFSLs. Reproduced with permission from Ref.<sup>[88]</sup>; (c) BP MIR photodetector. Reproduced with permission from Ref.<sup>[27]</sup>; (d) nano-antenna-enhanced graphene MIR photodetector. Reproduced with permission from Ref.<sup>[109]</sup>; (e) metasurface-mediated graphene MIR polarization detector with configurable polarity transition and covering all possible numbers of polarization ratio. Reproduced with permission from Ref.<sup>[111]</sup>; (f) TDBG MIR photodetector senses full-Stokes polarization, wavelength, and power simultaneously by leveraging tunable BPVE and CNN. Reproduced with permission from Ref.<sup>[119]</sup>

the huge lattice mismatches, such as dislocation filter superlattices (DFSs) and interfacial misfit (IMF) array, as illustrated in Figure 3(b).<sup>[86–88]</sup> In contrast, bonding techniques bypass the lattice mismatch issue and enable more straightforward integration.<sup>[89]</sup> Nevertheless, bonding techniques suffer from low fabrication yield and high fabrication complexity.<sup>[90]</sup> Additionally, photodetectors based on these narrow-bandgap semiconductors usually require cryogenic cooling for low-energy photon detection to minimize thermally generated charge carriers, which otherwise compete with the targeted optically excited carriers by generating excessive noise. Cryogenic cooling inevitably makes these photodetectors bulky, expensive, power-hungry, and delicate.<sup>[69,91]</sup>

Two-dimensional (2D) materials as emerging technologies for on-chip photodetectors have been attracting dramatically increasing research interest. Compared with the above-mentioned traditional three-dimensional (3D) materials, the layered lattice structures enable 2D materials with many exceptional properties. First, quantum confinement in the direction perpendicular to the 2D plane leads to novel electronic and optical properties that are distinctively different from their bulk parental materials. Second, their surfaces are naturally passivated without any dangling bonds, which makes it easy to integrate 2D materials with photonic structures as well as construct vertical heterostructures using different 2D materials, without the conventional lattice mismatch issue. Third, the use of thin layers without surface dangling bonds can also reduce noise resulting from generation-recombination, a strategy that is often not permitted in traditional 3D semiconductors due to surface recombination, making 2D materials more favorable for room-temperature photodetection.<sup>[92,93]</sup> Various 2D materials with different bandgaps can realize a very wide response range across the electromagnetic spectrum. Hexagonal boron nitride (hBN) is an insulator with a large bandgap of  $\sim 6$  eV, enabling solar-blind deep ultraviolet (UV) photodetectors.<sup>[94,95]</sup> Numerous transition metal dichalcogenides (TMDs) with bandgaps typically ranging from 1 to 2 eV cover visible and NIR wavelengths.<sup>[96,97]</sup> Black phosphorus (BP) possesses a narrow bandgap of  $\sim 0.33$  eV in its bulk form, pushing the cutoff wavelength to  $4.13 \mu\text{m}$  in the MIR (Figure 3(c)).<sup>[27,93]</sup> Beyond  $4.13 \mu\text{m}$ , through alloying with arsenic<sup>[98,99]</sup> or exploring the Stark effect by applying a vertical electric field,<sup>[100]</sup> BP's bandgap can be narrowed and its photoresponse has been extended to around  $8 \mu\text{m}$ . Nonetheless, BP suffers from weak air stability. Semimetallic materials (for example, graphene<sup>[101,102]</sup> and several TMDs in their bulk form, such as  $\text{PdSe}_2$ ,<sup>[103,104]</sup>  $\text{PtSe}_2$ ,<sup>[105]</sup>  $\text{PtTe}_2$ ,<sup>[106,107]</sup>  $\text{MoTe}_2$ ,<sup>[108]</sup> etc.) are another suitable choices for photodetection at long wavelengths. Their gapless nature endows them with broadband photoresponse ranging from UV to THz, combined with fast response speed.<sup>[69]</sup>

Similar to MEMS-based detectors, plasmonic enhancement strategies have also been utilized in on-chip detectors using nanophotonic technologies. Yao et al. from Prof. Capasso's group at Harvard University designed metallic nanoantenna structures to simultaneously improve light absorption and photocarrier collection in graphene detectors, as shown in Figure 3(d).<sup>[109]</sup> The coupled nanoantennas concentrate free-space light into the nanoscale deep-subwavelength antenna gaps, where the graphene light interaction is greatly enhanced as a result of the ultrahigh electric field intensity inside the gap. Meanwhile, the metallic nanoantennas were designed to serve as electrodes that collect the generated photocarriers very efficiently. As a result, the MIR nanoantenna-assisted graphene detectors achieved more than 200 times enhancement of responsivity at room temperature compared to devices without nanoantennas. Wei et al. from Prof. Lee's group at National University of Singapore (NUS) utilized non-centrosymmetric metallic nanoantennas in graphene photodetectors to mimic an artificial bulk photovoltaic effect (BPVE).<sup>[110]</sup> The non-centrosymmetric nanoantennas break the symmetry of local field, helping photocarriers to gain momentum and form a shift current that is nonlocal and directional. The BPVE enables not only cascaded photoresponse with high sensitivity but also calibration-free detection of polarization angle with a single device. Wei et al. further optimized the nanoantenna-mediated graphene photodetectors to enable configurable polarity transition.<sup>[111]</sup> As depicted in Figure 3(e), by tuning the orientation of nanoantennas, polarization ratio values vary

from positive (unipolar regime) to negative (bipolar regime), covering all possible numbers ( $1 \rightarrow \infty/-\infty \rightarrow -1$ ). Furthermore, their device achieved subtle measurement of polarization-angle perturbation down to  $0.02^\circ \text{ Hz}^{-1/2}$  in the MIR range. Their works provide a promising platform for miniaturized polarimetry.

Moiré superlattices formed by twisted stacks of 2D materials have been rising rapidly as a hot research topic in recent few years as they feature many novel physical phenomena such as superconductivity,<sup>[112]</sup> ferromagnetism,<sup>[113]</sup> and emerging topological properties.<sup>[114,115]</sup> These unusual electronic features are controlled by the twist angle between the two layers, with potential in the developing field of twistronics. Analogous concepts have recently been explored in photonics.<sup>[116,117]</sup> Prof. Xia's group at Yale University discovered strong MIR photoresponse in small-twist-angle bilayer graphene.<sup>[118]</sup> Compared with monolayer graphene, the Brillouin zone folding in twisted bilayer graphene (TBG) leads to the formation of a superlattice bandgap and substantial modification to the density of states. A maximum extrinsic photoresponsivity of 26 mA/W was achieved at  $12 \mu\text{m}$  when the Fermi level in  $1.81^\circ$  TBG was tuned to its superlattice bandgap. Moreover, the strong photoresponse critically depends on the formation of a superlattice bandgap, and it vanishes in the gapless case with an ultrasmall twist angle ( $<0.5^\circ$ ). Later, the same group reported the observation of tunable MIR BPVE in twisted double bilayer graphene (TDBG), arising from the moiré-induced strong symmetry breaking and quantum geometric contribution.<sup>[119]</sup> The BPVE-type photoresponse depends substantially on the polarization state of the excitation light and is highly tunable by external electric fields. Leveraging this wide tunability in quantum geometric properties, the authors used a convolutional neural network (CNN) to achieve full-Stokes polarimetry together with power and wavelength detection simultaneously, using only one single TDBG device with a subwavelength footprint of merely  $3 \times 3 \mu\text{m}^2$ , as shown in Figure 3(f).

### 2.3. Waveguide-integrated photodetectors for photonic nanosystems

On-chip integration of waveguides and detectors is an essential step toward the realization of chip-scale photonic nanosystems. In addition, waveguide integration also introduces several important performance benefits. First, waveguide integration contributes to the improvement of SNR by suppressing noise. This is because several types of noise (shot noise, Johnson noise, and generation-recombination noise) that often limit detector SNR linearly scale with the active volume of a detector. When light is funneled into the detector via a waveguide (with core index  $n$ ) rather than from free space, the detector active volume and hence noise can be reduced approximately by a factor of  $n^2$  without compromising optical absorption. Such noise mitigation is critical in MIR detectors made of narrow-bandgap semiconductors, which suffer from a much higher noise floor. Second, waveguide-integrated detectors can achieve larger bandwidths than their free-space counterpart. The smaller detector volume diminishes RC delay and carrier transit time. Last but not least, waveguide-integrated detectors decouple the optical absorption path from the carrier transit path and the absorption material thickness. High quantum efficiency requires a sufficiently large optical path length for complete absorption of incident photons, whereas efficient carrier collection requires a short carrier transit path to enhance quantum efficiency and transit-time-limited bandwidth in photovoltaic detectors or to boost photoconductive gain in photoconductors. In free-space detectors, the optical absorption path often coincides with the carrier transit path, which sets a trade-off between optical absorption and carrier collection. In addition, the optical absorption path length is limited by the absorption material thickness. Conversely, in waveguide-integrated detectors, the optical absorption path is decoupled from the absorption material thickness and orthogonal to the carrier transit path, thereby offering more flexibility in the device geometry design for performance optimization.<sup>[22]</sup>

Photodetectors based on nanophotonic technologies are no doubt more favorable for further development of waveguide-integrated detectors as compared with MEMS-based detectors. In the NIR, Ge can be epitaxially grown on Si waveguides in similar ways as on Si substrates. Various types of waveguide-integrated photodetectors based on Ge epitaxy on Si waveguides have been reported, such as butt-coupled MSM,<sup>[120]</sup> butt-coupled p-i-n,<sup>[121]</sup> top-coupled p-i-n,<sup>[122]</sup> bottom-coupled p-i-n (Figure 4(a)),<sup>[123]</sup> APD,<sup>[124]</sup> and GeSn photodetector.<sup>[125]</sup> We also refer readers to these above-mentioned dedicated sources for more details on waveguide-integrated Ge-on-Si photodetectors.<sup>[70,81,82]</sup>

Moving to the MIR, mainly three classes of waveguide-integrated photodetectors have been demonstrated. The first class is heterogeneously integrated narrow-bandgap semiconductors. The delicate direct epitaxial growth methods developed for the integration of narrow-bandgap semiconductors on planar Si substrates are difficult to be implemented on Si waveguides. Thus most of the reported MIR waveguide-integrated narrow-bandgap semiconductor photodetectors rely on benzocyclobutene (BCB) adhesive bonding process, as shown in Figure 4(b).<sup>[126–129]</sup> In addition to the low fabrication yield and high fabrication complexity, BCB absorbs light considerably beyond  $3\text{ }\mu\text{m}$ , thus reducing the optical power reaching the photodetectors.<sup>[130]</sup> The second class is a monolithic detector integration approach that builds on Si itself. While crystalline Si has a band gap energy of  $1.12\text{ eV}$  and is transparent in the MIR, mid-gap states that are optically absorbing in the MIR can be introduced either by substitutional doping<sup>[131]</sup> or by forming lattice defects,<sup>[132]</sup> both of which can be realized through the implantation of proper ions, as illustrated in Figure 4(c). The main disadvantage of this kind of detector is their low responsivity due to the weak extrinsic dopant or defect level mediated absorption. Driving the device at high bias voltage in an avalanche mode markedly boosts its photoresponse but with the penalty of deteriorated noise figures.<sup>[133]</sup> The third class is the emerging 2D materials. As mentioned above, the layered lattice structures enable their direct integration with Si waveguides, making them a promising alternative solution for MIR waveguide-integrated photodetectors. Graphene, the first discovered 2D material, has also been first integrated with Si waveguides for photodetection from NIR to MIR since 2013.<sup>[134–140]</sup> Waveguide-integrated photodetectors using various TMDs,<sup>[141–143]</sup>

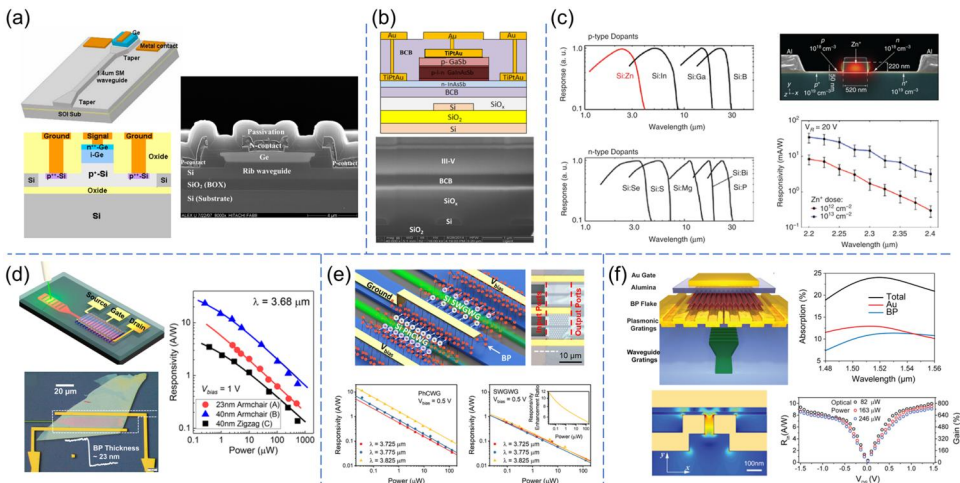


**Figure 4.** Waveguide-integrated photodetectors for photonic nanosystems. (a) NIR Si waveguide-integrated Ge photodetector fabricated by Ge epitaxy on Si. Reproduced with permission from Ref.<sup>[123]</sup>; (b) MIR Si waveguide-integrated photodetector based on adhesively bonded III-V compounds. Reproduced with permission from Ref.<sup>[128]</sup>; (c) ion-implanted Si MIR waveguide photodiode. Reproduced with permission from Ref.<sup>[131]</sup>; (d) MIR Si waveguide-integrated BP photodetector. Reproduced with permission from Ref.<sup>[33]</sup>; (e) slow-light-enhanced waveguide-integrated BP MIR photodetector. Reproduced with permission from Ref.<sup>[150]</sup>; (f) BP photodetector based on a 3D integration platform of Si photonics and plasmonics. Reproduced with permission from Ref.<sup>[145]</sup>

BP,<sup>[144–146]</sup> and 2D material heterostructures<sup>[147,148]</sup> have been reported as well. Huang et al. demonstrated the first waveguide-integrated photodetector for the MIR beyond 3  $\mu\text{m}$  by integrating BP photodetectors with Si grating couplers, as shown in Figure 4(d).<sup>[33]</sup> Responsivity of 23 A/W at 3.68  $\mu\text{m}$  and 2 A/W at 4  $\mu\text{m}$  were achieved with 1 V bias under room temperature. The responsivity is among the highest in the reported waveguide-integrated IR detectors. Nevertheless, this high responsivity was obtained at the expense of a long device length of 80  $\mu\text{m}$ .

Further miniaturization of the photodetector is expected to improve the operation speed, SNR, and internal quantum efficiency, as well as reduce the total energy consumption and insertion loss.<sup>[145,149]</sup> Inevitably, undesired weaker photoresponse is accompanied by the reduced light-matter interaction length. To maintain a high responsivity in the waveguide-integrated photodetector with a reduced footprint, Ma et al. proposed a method utilizing the slow light effect in photonic crystal waveguide (PhCWG), as shown in Figure 4(e).<sup>[150]</sup> Slow light with remarkably low group velocity spatially compresses optical energy, resulting in enhanced light-matter interaction.<sup>[151,152]</sup> At 3.825  $\mu\text{m}$  with a group index of 103.3, the responsivity was enhanced by more than tenfold in the BP photodetector integrated on a 10  $\mu\text{m}$  long PhCWG, as compared with the counterpart integrated on a subwavelength grating waveguide (SWG WG) without slow light effect. At a 0.5 V bias, the BP (40 nm Zigzag) PhCWG photodetector achieves a responsivity of 11.31 A/W. Compared with the 40 nm zigzag device in the previous work by Huang et al. under similar conditions of wavelength and power,<sup>[33]</sup> a comparable responsivity was achieved with half of the applied voltage bias and one-eighth of the device length. In comparison with previously reported BP waveguide photodetectors,<sup>[144–146]</sup> this work presents a device that maintains high responsivity with low voltage bias and small device footprint even when working beyond the roll-off wavelength ( $\sim 3.6 \mu\text{m}$ ) and near the cutoff wavelength (4.13  $\mu\text{m}$ ) of BP. Besides slow light waveguides, optical resonators such as microring resonators (MRRs) and photonic crystal cavities can also enhance the light-matter interaction and have been demonstrated to improve the performance of integrated photodetectors.<sup>[140,142,153]</sup> Plasmonic enhancement has also been utilized in waveguide-integrated photodetectors by integrating plasmonic structures with dielectric waveguides (Figure 4(f))<sup>[135,138,139,145,154,155]</sup> or using plasmonic waveguides.<sup>[156,157]</sup> Metallic plasmonic structures can enhance light-matter interaction over a bandwidth much broader than dielectric optical resonators, while introducing high ohmic loss and severely reducing the light that can be absorbed by the photodetection material.

### 3. Optical sensors

Optical sensors have been attracting more and more research interest due to their advantages of fast response, low crosstalk, strong detection multiplexing capability, and immunity to electromagnetic interference. Optical sensors have been widely studied for both physical and chemical/biological (i.e., molecular) sensing applications. Technical evolution from optical MEMS to nanophotonics and then to photonic nanosystems has also been witnessed for higher compactness and integration level, better sensing performances, and more functionalities. Table 1 summarizes the most explored sensing mechanisms, typically employed structures, and major performance

**Table 1.** Summary of optical sensors.

Sensing mechanism	Optical structure		Performance parameter
	Optical MEMS	Nanophotonics & photonic nanosystems	
Resonance wavelength shift	Fiber resonator, Fabry-Pérot cavity	Photonic crystal cavity, microring/microdisk resonator	Sensitivity, limit of detection, resolution, response time
Intensity change	Fiber	Waveguide, nanoantenna	



parameters of optical sensors. It is worth noting that resonance wavelength shift can also be detected as intensity change in the sideband-resolved regime.

### 3.1. Optical-MEMS-based physical, chemical, and biological sensors

The use of optical transmission as sensing and readout signal for pressure and displacement detection has been popular due to its sensitivity to the finest disturbance caused by the environment, while at the same time being immune to electromagnetic interference.<sup>[4,19,158,159]</sup> Depending on the sensing mechanism, the readout can be either from the optical intensity change or resonance wavelength shift due to the movement of the MEMS component. Due to the fabrication limitation in the early days, the optical MEMS sensors are relatively bulky, and the signal detection relies on a photodetector placed nearby or transmission by optical fiber to avoid excessive signal loss. Figure 5(a) depicts an optical micro-machined microphone with a sub-15 dBA noise floor using a grating-based optical-interferometric readout.<sup>[160]</sup> The optical emitters and detector are integrated onto a printed circuit board (PCB) with a MEMS diaphragm consisting of a diffraction grating etched near the center. When the system is subject to an external sound pressure excitation, the gap between the diaphragm and grating will be changed, and subsequently, the intensities of the beams will be modulated. The fabricated device is reported to reach a thermal-mechanical noise floor of 14.2 dBA and an SNR of over 80 dB. The use of a fully passive MEMS diaphragm and optical interferometric readout avoids some problems of traditional capacitive MEMS acoustic sensors, such as electrostatic pull-in that degrades the sensor performance. As such, a few other works have reported similar configurations for microphone and accelerometer applications.<sup>[161,162]</sup> Another type of optical MEMS physical sensor utilizes optical fiber for long-distance remote sensing. Compared with the previous type, a small portion of the

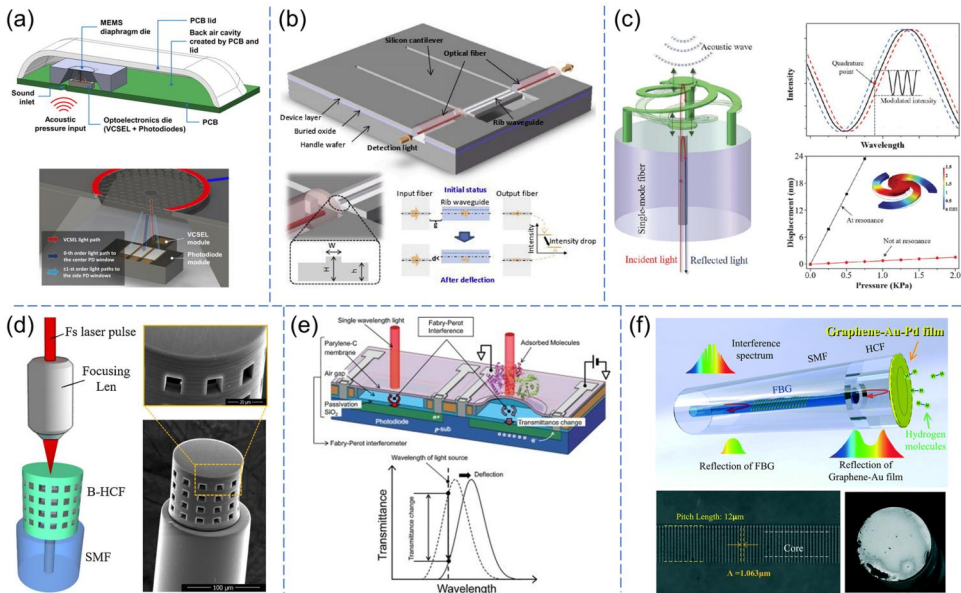


**Figure 5.** Optical-MEMS-based physical, chemical, and biological sensors. (a) Optical micromachined microphone with integrated light source and detector. Reproduced with permission from Ref.<sup>[160]</sup>; (b) micro-cantilever-based high sensitivity all-optical acoustic pressure sensor with integrated waveguide. Reproduced with permission from Ref.<sup>[34]</sup>; (c) fiber-tip acoustic sensor with 3D-printed suspended optomechanical microresonator. Reproduced with permission from Ref.<sup>[165]</sup>; (d) fiber-optic-based humidity sensor with 3D-printed FP nanocavity. Reproduced with permission from Ref.<sup>[166]</sup>; (e) surface stress sensor based on MEMS FP interferometer for biosensing. Reproduced with permission from Ref.<sup>[35]</sup>; (f) fiber optic sensor based on FP interferometer with fiber Bragg grating and nanofilm for hydrogen detection. Reproduced with permission from Ref.<sup>[171]</sup>

waveguide is integrated into the MEMS membrane, where the light is coupled through the fiber ends. The movement of the membrane will cause the light intensity to change. As shown in [Figure 5\(b\)](#), Li et al. demonstrated an all-optical acoustic pressure sensor based on a micro-optomechanical cantilever.<sup>[34]</sup> The cantilever with an integrated rib waveguide at the tip was designed with the natural frequency near the target acoustic frequency so that mechanical resonance enhances the weak acoustic pressure detection. As a result, it achieved experimentally a detection sensitivity of 8.34 V/Pa with a minimum detectable pressure of 35 nPa/Hz<sup>1/2</sup> at 150 Hz. The use of a cantilever with optical fiber for detection has certainly simplified the system complexity whilst still maintaining sufficient accuracy. In addition to acoustic sensing, contact force and vibration sensing have also been demonstrated in the literature.<sup>[163,164]</sup> The advancement of high-precision additive manufacturing in recent years has provided alternate solutions to compact optical MEMS physical sensors as well. As shown in [Figure 5\(c\)](#), a 3D-printed spirally-suspended optomechanical microresonator is fabricated at the tip of an optical fiber, forming a Fabry-Pérot (FP) interferometer for acoustic sensing.<sup>[165]</sup> The use of in situ additive manufacturing has provided more flexibility and compatibility for sensor integration on different platforms. The presented acoustic sensor has achieved a high sensitivity of 118.3 mV/Pa and a low noise equivalent acoustic signal level of 0.328  $\mu\text{Pa}/\text{Hz}^{1/2}$  at the audio frequency range. A similar 3D-printed FP nanocavity at the tip of fiber has been demonstrated for humidity sensing, as shown in [Figure 5\(d\)](#).<sup>[166]</sup> The castle-style nanocavity with periodically etched holes was filled with Polyvinyl Alcohol (PVA) to increase the contact area of water vapor for enhanced sensitivity. The relative humidity was measured based on the interference spectrum wavelength shift. The proposed device experimentally achieved a sensitivity of 248.9 pm/%RH in the relative humidity range of 46%RH to 75%RH.

In addition to physical sensing, chemical and biological molecule sensing have also been demonstrated with optical MEMS sensors. Usually, the sensing of substances is performed by measuring the mechanical deformation of the membrane/cantilever that has been surface functionalized to interact with specific molecules.<sup>[167–170]</sup> [Figure 5\(e\)](#) depicts an optical MEMS-based surface strain sensor for label-free biosensing.<sup>[35]</sup> A perylene-C membrane is coated with amino-methyl to immobilize the antibodies via electrostatic coupling. When the membrane has attracted the target antibodies, the surface stress will change, and the resulted deformation will be captured by the transmittance change in the FP sensor. Such a sensor holds the potential for a universal biochemical sensing platform with different coating materials. Gas sensing is another important application for optical MEMS sensors. [Figure 5\(f\)](#) shows a fiber optic hydrogen sensor based on an FP interferometer with fiber Bragg grating and a graphene-Au-Pd nanofilm as an absorbing membrane.<sup>[171]</sup> The Au-Pd film is chosen to ensure the high reflectivity of the optical signal and Pd film is used for the absorption of hydrogen to create reversible expansion. A nonlinear wavelength shift of 290 pm is recorded between the hydrogen concentration of 0 and 4.5 vol%, with a response time of 4.3 s.

### 3.2. Nanophotonic physical, chemical, and biological sensors

#### 3.2.1. Nanophotonic physical sensors

A major category of nanophotonic physical sensors is optomechanical sensors. In the past few decades, optomechanics has drawn great interest for precise physical sensing due to its ultrahigh sensitivity and the possibility to detect motion at or even below the standard quantum limit.<sup>[172]</sup> Typically, the optomechanical system involves an optomechanical cavity, in which the optical field is well confined at the nanoscale, enabling a strong interaction between the optical field and mechanical objects. In this cavity optomechanical system, the mechanical motion translates into perturbation of cavity mode and therefore shifts the optical cavity resonance. As a result of both high mechanical and optical Q factors, the optomechanical cavity is exquisitely sensitive to

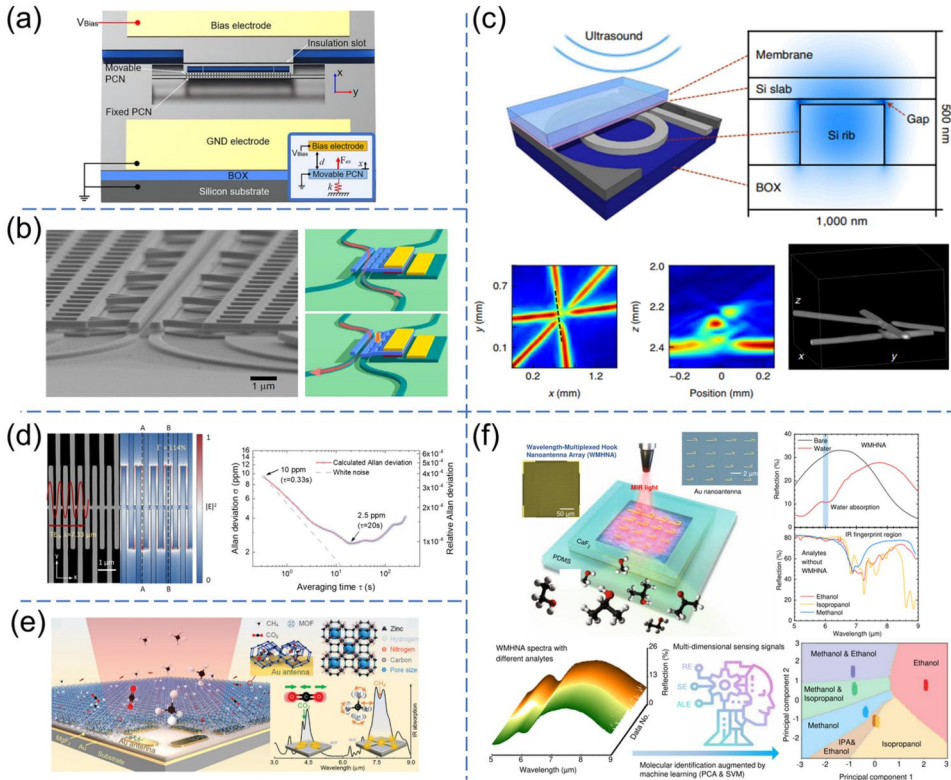


**Figure 6.** Nanophotonic physical, chemical, and biological sensors. (a) Nanoscale optomechanical electrometer using PCN cavities. Reproduced with permission from Ref.<sup>[180]</sup>; (b) Integrated nano-optomechanical displacement sensor. Reproduced with permission from Ref.<sup>[181]</sup>; (c) Si waveguide-based optomechanical ultrasound sensor for ultrasonography and photoacoustic tomography. Reproduced with permission from Ref.<sup>[36]</sup>; (d) suspended Si SWG comb waveguide with larger-than-unity external optical field confinement for ultrasensitive LWIR gas spectroscopy. Reproduced with permission from Ref.<sup>[37]</sup>; (e) metallic-nanoantenna-based SEIRA platform with multiple resonances and MOF coating for enhanced simultaneous sensing of multiple gases. Reproduced with permission from Ref.<sup>[216]</sup>; (f) SEIRA platform leveraging WMHNAs and machine learning for high-accuracy molecular recognition from mixtures. Reproduced with permission from Ref.<sup>[227]</sup>

mechanical motion, and the footprint of the sensors is also greatly reduced. Based on ultrasensitive motion detection, precision sensing of various physical stimuli, including acceleration,<sup>[173,174]</sup> rotation,<sup>[175,176]</sup> and force,<sup>[177,178]</sup> have been realized in the optomechanical systems. Recently, research efforts have also been made to bring optomechanical systems into electrical voltage or charge detection. Most of the previous MOEMS mainly leverage electrostatic force as actuation for mechanical switching or optical reconfiguration.<sup>[179]</sup> Alternatively, one can measure the electric voltage through the resonance shift of the optomechanical cavity. As shown in Figure 6(a), Xia et al. proposed a nanoscale optomechanical electrometer for electric voltage detection, which consists of two coupled photonic crystal nanobeam (PCN) cavities with one working as a movable perturbation-sensitive mechanical resonator.<sup>[180]</sup> The optomechanical coupling occurs when the other fixed PCN cavity is radiation driven by the pump light. Consequently, both the optical gradient force and electrostatic force are feasible to enable in-plane mechanical movement of the entire suspended structure, with a narrow gap separation of 150 nm between two PCN cavities. Particularly, when the optomechanical electrometer is driven above the threshold power, it will turn into a self-sustained oscillation state with a greatly enhanced SNR. Under this operation condition, a sensitivity of  $0.014 \text{ Hz/mV}^2$  with a fine resolution of  $1.37 \text{ mV}^2 \cdot \text{Hz}^{-1/2}$  was achieved. Optical read-out of motion in optomechanical systems also leads to compact and integrated optical motion sensors with broadband spectral resonances. In 2020, Liu et al. reported a

broadband nano-optomechanical displacement sensor as presented in Figure 6(b).<sup>[181]</sup> It mainly consists of four evanescently coupled waveguides to form a nanomechanical directional coupler, with two suspended ones on top. The light can precisely probe the vertical displacement of top waveguides by measuring the relative transmission from the two output waveguides. The directional coupler before displacement can support a superposition of symmetric and anti-symmetric supermodes and interferes constructively at the cross port after traveling for a beating length in the directional coupler. With a reduced vertical gap, the propagation constants of the supermodes change and therefore make the interference destructive, resulting in increased transmission from through the port. Based on this three-dimensional directional coupler with on-chip waveguide photodiode, a  $30 \text{ fm} \cdot \text{Hz}^{-1/2}$  imprecision along with  $>50 \text{ dB}$  displacement dynamic range are experimentally achieved. Meanwhile, due to this cavity-free design, the optical bandwidth is ultrabroad even above  $80 \text{ nm}$ , eliminating the requirement for tunable lasers and making it insensitive to frequency noise.

Optomechanical systems have also been employed in ultrasound sensors with both improved sensitivity and miniaturized size. In 2019, Basiri-Esfahani et al. introduced cavity optomechanical ultrasound sensing, demonstrating an ultralow noise equivalent pressure of  $8\text{--}300 \text{ } \mu\text{Pa} \cdot \text{Hz}^{-1/2}$  at kilohertz to megahertz frequencies with a dynamic range above  $120 \text{ dB}$ .<sup>[182]</sup> The cavity optomechanical acoustic sensor consists of a silica microdisk optical cavity which is evanescently coupled to a tapered optical fiber. Light is intensively confined in a whispering gallery mode (WGM) around the periphery of the suspended disk and the mechanical eigenmodes can be resonantly driven via an acoustic field. With the small mask of the microdisk and thin supporting spokes, this sensor has two to three orders of improved sensitivity as compared to traditional air-coupled or liquid-coupled ultrasound sensors.<sup>[60,183,184]</sup> In 2021, Westerveld et al. demonstrated photoacoustic tomography using an ultrasensitive Si optomechanical ultrasound sensor, as presented in Figure 6(c).<sup>[36]</sup> The sensor is based on a small ring resonator with a radius of  $10 \text{ } \mu\text{m}$ , with a narrow  $15 \text{ nm}$  gap between the optomechanical waveguide and a slab part of the waveguide hovering above the rib part on a large suspended membrane. The laser wavelength was stepped across the optical resonance of the ring resonator, which recorded both the average optical transmission and the sensor information of the ultrasound pulse. The sensor demonstrated both broadband detection ( $3\text{--}30 \text{ MHz}$ ) and high sensitivity ( $\text{NEP}$  below  $1.3 \text{ mPa} \cdot \text{Hz}^{-1/2}$ ) simultaneously. Based on the prominent ultrasound detection capability of the sensor, the authors further demonstrated a one-dimensional array of ten sensors with ring resonators in slightly different radii, which are all coupled to the same bus waveguide. As a result, the resonances are almost evenly distributed over their free spectral range of  $\sim 17 \text{ nm}$  and can be applied in raster-scan photoacoustic tomographic imaging. 2D reconstructed photoacoustic images of one suture at various depths show a good SNR up to a large depth of  $15 \text{ mm}$ , with a suture diameter of around  $40 \text{ } \mu\text{m}$ . For more details on optomechanical sensors, we refer readers to some relevant topical reviews.<sup>[19,158]</sup>

### 3.2.2. Nanophotonic chemical and biological sensors

Nanophotonic chemical and biological sensors can be classified into waveguide and free-space configurations. Compared with free-space configuration, waveguides implement long optical path-lengths on chips, thus are more favorable in sensor miniaturization and their on-chip integration with other components including microfluidics, light sources, photodetectors, and optoelectronic circuits.<sup>[19]</sup> However, most of the waveguides probe analytes via evanescent fields, resulting in a weak light-matter interaction limited to a fraction of that for a free-space beam. Therefore, various strategies have been developed to strengthen the light-matter interaction and thus improve the performances of waveguide sensors, such as using TM mode,<sup>[185]</sup> thinner waveguide,<sup>[186]</sup> suspended waveguide,<sup>[187]</sup> slot waveguide,<sup>[188]</sup> subwavelength grating (SWG) waveguide,<sup>[189]</sup> slow light effect,<sup>[190]</sup> etc. Different strategies can be combined for more improvement, such as



subwavelength multibox waveguide combining slot and SWG structures,<sup>[191]</sup> and photonic crystal slot waveguide combining slot and slow light effect.<sup>[192]</sup>

In addition to the development of various performance improvement strategies, another important development trend for waveguide sensors is migrating the working wavelengths from NIR to MIR. Chemical and biological molecules perturb the evanescent field and modify the cladding refractive index (RI) and/or induce an additional optical absorption. Accordingly, waveguide chemical and biological sensors can be generally classified into RI-based sensors and absorption-based sensors. RI-based sensors can neither differentiate nor identify unlabeled analytes effectively without modification of sensor surfaces, because different species that coexist in a sample register nearly indistinguishable shifts of RI when interacting with the evanescent field. Conversely, absorption-based sensors leverage the characteristic (fingerprint) absorptions of molecules, in which the characteristic absorption wavelengths are determined by the vibration frequencies of their contained chemical bonds. Consequently, absorption-based sensors possess intrinsic molecular selectivity without the need for analyte labeling or sensor surface functionalization. Despite a few absorption-based waveguide sensors demonstrated in the NIR, some drawbacks are inevitable. Firstly, the number of molecular fingerprints is limited in the NIR. Only sensing of substances that are rich in the C–H bond such as methane (CH<sub>4</sub>), xylene (C<sub>8</sub>H<sub>10</sub>), and N-methylaniline (C<sub>7</sub>H<sub>9</sub>N) has been demonstrated.<sup>[185,192,193]</sup> Secondly, the absorption originating from these NIR fingerprints is weaker compared to the MIR counterparts, leading to an inferior sensing performance.<sup>[194]</sup> The MIR spanning 2 to 20  $\mu\text{m}$  in the electromagnetic wave spectrum is an ideal wavelength range for absorption-based waveguide sensors as it contains the primary absorption fingerprints of most chemical bonds, including C–H, C–O, C–C, C=C, O–H, N–O, etc.<sup>[22]</sup> MIR absorption-based waveguide sensors have been built on the common silicon-on-insulator (SOI) and silicon nitride-on-insulator (SNOI) platforms.<sup>[195,196]</sup> However, the working wavelengths of these platforms are only up to  $\sim 4\mu\text{m}$  due to the severe absorption from the buried oxide (BOX) layer. To extend the working wavelength so as to leverage more molecular fingerprints, various alternative waveguide platforms have been developed and utilized to construct absorption-based sensors, such as suspended Si,<sup>[197]</sup> silicon-on-sapphire (SOS),<sup>[198]</sup> silicon-on-calcium fluoride (SOCF),<sup>[199]</sup> germanium-on-silicon (GOS),<sup>[200]</sup> etc.

Efforts have also been made to improve the sensitivity of MIR absorption-based waveguide sensors. A strategy is to employ enrichment coatings, which, however, sacrifice versatility and response speed.<sup>[201]</sup> Another is to optimize the waveguide configuration for stronger light-matter interaction. The light-matter interaction strength of the waveguide can be captured through the external optical field confinement factor  $\Gamma$ .<sup>[202]</sup> The limit of detection (LoD) depends on not only the light-matter interaction strength given by  $\Gamma$  but also the interaction length limited by propagation loss. Several alternatives to conventional strip waveguides have been proposed for more optical field delocalization into air claddings and thus higher  $\Gamma$ , such as suspended thin waveguide,<sup>[197]</sup> suspended slot waveguide,<sup>[203]</sup> pedestal waveguide,<sup>[204]</sup> etc. Liu et al. from Prof. Lee's group at NUS developed a suspended Si waveguide platform with SWG cladding operating in 6.4–6.8  $\mu\text{m}$  by locally removing the BOX layer of the SOI wafer.<sup>[205]</sup> Through engineering the effective RI of the SWG cladding by tailoring its period and duty cycle, a high  $\Gamma$  of 24.3% was achieved while maintaining a low propagation loss of 3.9 dB/cm. Using a 28.4-mm-long waveguide, they realized toluene vapor sensing with a low 3- $\sigma$  LoD of 75 ppm (corresponding to a 1- $\sigma$  LoD of 25 ppm) and a short response time of 0.8 s. It is worth noting that  $\Gamma$  accounts for both field distribution and waveguide dispersion, which makes a  $\Gamma$  larger than unity (corresponding to free-space beam) possible. Recently, by leveraging strong TM field delocalization at small waveguide thickness with a moderate dispersion, Vlk et al. demonstrated a  $\Gamma$  of 107% at 2.566  $\mu\text{m}$  with a propagation loss of 6.8 dB/cm in a suspended tantalum pentoxide rib waveguide.<sup>[206]</sup> Correspondingly, they realized a 7 ppm 1- $\sigma$  LoD for acetylene gas with a 20-mm-long waveguide. However, the vertically wide distributed mode requires a large gap separation of 20  $\mu\text{m}$  between



the waveguide and the substrate, which not only results in a mechanically fragile high-aspect-ratio membrane structure but also is hard to implement on conventional waveguide platforms due to insulator thickness constraints. More recently, Liu et al. further proposed an SWG comb waveguide design, still on the suspended Si platform.<sup>[37]</sup> The extraordinary optical field confinement is enabled by large longitudinal electric field discontinuity at periodic high-index-contrast Si/air interfaces in the SWG, together with its unique features in RI engineering. By optimizing the period and duty cycle of the SWG, they realized a  $\Gamma$  of 113% with a low propagation loss of 4.7 dB/cm at 7.33  $\mu\text{m}$ . Using an SWG comb waveguide of only 10 mm in length, they realized acetone vapor sensing with a low 1- $\sigma$  LoD of 2.5 ppm, as shown in Figure 6(e). Even higher  $\Gamma$  enabled by strong dispersion in slow light PhCWGs have been claimed.<sup>[207,208]</sup> Nevertheless, their performance is limited by high propagation loss and is susceptible to fabrication errors.

In the field of free-space sensors, traditional non-dispersive infrared (NDIR) and tunable diode laser absorption spectroscopy (TDLAS) sensors typically employ huge gas cells or optical multipass cells/cavities to implement long free-space optical path so as to increase the probability of absorption by sparse target molecules, resulting in bulky volume and slow response time.<sup>[12]</sup> A promising approach to miniaturize sensors in free-space configuration has attracted intense research interest since a decade ago, which is surface-enhanced infrared absorption (SEIRA).<sup>[209]</sup> SEIRA is typically performed by metallic optical resonators (nanoantennas). Same as in the above-mentioned plasmonic enhancement of optical detectors, metallic nanoantennas convert incoming far-field energy into highly confined subwavelength near-fields via plasmon excitation.<sup>[64,65]</sup> Various nanoantenna structures have been reported for sensing applications, for example, split-ring resonator,<sup>[210]</sup> nanorod,<sup>[211]</sup> nanoslit,<sup>[212]</sup> bow-tie,<sup>[213]</sup> and MIM-based perfect absorber.<sup>[214]</sup> Arrays containing nanoantennas of different geometries or dimensions provide multiple resonances over a broad spectral range and have been utilized to simultaneously detect multiple analytes, as shown in Figure 6(e).<sup>[215–217]</sup> Nonetheless, the sensitivity enhancement in current nanoantenna designs normally relies on stronger mutual coupling of nanoantennas using nanogap or larger overlap between light and molecules by undercut, thus facing a trade-off between performance and fabrication cost.<sup>[218,219]</sup> Loss engineering of nanoantennas has been applied to overcome this bottleneck. Wei et al. presented novel crooked nanoantennas based on loss engineering.<sup>[220]</sup> Compared with the common straight nanorod antennas, the crooked nanoantennas enhance molecule signals by 25 times, enabling a transmissive CO<sub>2</sub> sensor with sensitivities up to 0.067% ppm<sup>-1</sup>. Zhou et al. proposed a dual-phase strategy that leverages loss-induced different Fano-resonant phases to access both destructive and constructive signals of molecular vibration, which enhances molecule signals by 4.2 times and leads to a low LoD of 13 ppm in CO<sub>2</sub> sensing.<sup>[221]</sup> Various enrichment coatings have been employed in nanoantenna sensors to further improve the sensitivity, such as metal-organic framework (MOF) (Figure 6(e)),<sup>[216]</sup> polyethyleneimine (PEI),<sup>[215]</sup> polytetrafluoroethylene (PTFE),<sup>[222]</sup> and MOF-PEI hybrid film.<sup>[223]</sup>

Parallel with the sensor design optimization, another development direction being investigated to improve sensor performances is the employment of advanced data analysis methods. Artificial intelligence (AI) techniques, as emerging and appealing methodologies for data analysis, have been recently utilized in plasmonic nanoantenna sensors to deal with the raw multiplexed sensing data and enhance molecule discrimination capabilities.<sup>[224–226]</sup> Ren et al. proposed a loss engineering method to optimize the damping rate by reducing radiative loss using hook nanoantennas (HNAs).<sup>[227]</sup> With the spectral multiplexing of the HNAs from gradient dimension, the wavelength-multiplexed HNAs (WMHNAs) serve as ultrasensitive vibrational probes in a continuous ultra-broadband spectral range from 6 to 9  $\mu\text{m}$ . Leveraging the multi-dimensional features captured by WMHNA, they developed a machine learning method combining principal component analysis (PCA) and supporting vector machine (SVM) to extract complementary physical and chemical information from molecules. The proof-of-concept demonstration of molecular recognition from mixed alcohols (methanol, ethanol, and isopropanol) shows 100% identification

accuracy from the microfluidic integrated WMHNAs, as shown in Figure 6(i). AI data analysis methods can also be employed in waveguide sensors. Li et al. demonstrated label-free multicomponent chemical analysis using a single MRR to perform refractometric sensing of the mixture and a neural network model to predict the compositions.<sup>[228]</sup> High prediction accuracy was achieved with a low root-mean-squared error ranging only from 0.13 to 2.28 mg/mL. The predicted concentrations of each component in the testing dataset almost all fell within the 95% prediction bands. Zhou et al. presented an AI-enhanced SWG waveguide sensing platform for aqueous mixture analysis in the MIR.<sup>[229]</sup> With the sensitivity-improved SWG waveguide and the assistance of machine learning, the MIR absorption spectra of a ternary mixture in water could be successfully distinguished and decomposed to single-component spectra for predicting concentration. Classification accuracies of 98.88% for 64 mixing ratios and 92.86% for four concentrations below the limit of detection (972 ppm, based on  $3\text{-}\sigma$ ) with steps of 300 ppm were realized. Besides, the mixture concentration prediction with root-mean-squared error varying from 0.107 vol% to 1.436 vol% was also achieved.

### 3.3. Photonic physical, chemical, and biological sensing nanosystems

#### 3.3.1. Photonic physical sensing nanosystems

While optomechanical cavities provide access for signal transduction between the optical and mechanical domains, it is also of interest to bring the radio frequency (RF) active tuning into the optomechanical cavity systems for more functionalities and enhanced sensitivity. Piezoelectric-driven and electrostatic-driven are two mainstream approaches to probing the optomechanical cavity and provide the extra bridge for energy exchange between phonon and photon.<sup>[230]</sup> By leveraging the interaction between stimulated acoustic phonons and pump photons, electro-optomechanical sensing platforms offers superior capabilities for inertial sensing without moving element, with greatly enhanced reliability of the sensors. As shown in Figure 7(a), an acousto-optic (AO) gyroscope is proposed with a photonic Mach-Zehnder interferometer (MZI) structure and two inherently matched piezoelectric surface acoustic wave (SAW) resonators.<sup>[38]</sup> While current MEMS-based inertial sensors are typically vulnerable to shock due to a large released mass, this AO gyroscope enables the realization of a large unreleased mass and wide bandwidth operation, with the rotational signal acquired from the induced Coriolis force  $F_c$  by checkerboard-shaped metallic pillars. The  $F_c$  can be expressed as:

$$F_c = -2M_p\Omega_z \times v_p \quad (3)$$

where  $M_p$  is the effective mass of the metallic pillars,  $\Omega_z$  is the out-plane rotation, and  $v_p$  is the longitudinal vibration velocity. The induced force is orthogonal to the wave propagation direction, which is then read by the push-pull MZI structure with different phase shifts in two arms. This AO gyroscope shows a sensitivity of 48 nV/(°/s) and an angular random walk of  $60^\circ/\text{h}^{-1/2}$ , indicating the promising potential of this new class of gyroscopes that combines the advantages of both conventional vibrating gyroscopes and optical gyroscopes. Recent research works also find the potential of low-dimensional materials, such as graphene, carbon nanotubes, and semiconducting nanowires, to be employed in mechanical resonators for further reduction of inertial mass.<sup>[231,232]</sup> With the unique properties in the atom-layered thick and ultralow mass low-dimensional materials, high-precision force and mass sensing can be achieved. Nevertheless, the sensitivity of such sensors is often limited by measurement imprecision and thermo-mechanical noise. As shown in Figure 7(b), Weber et al. investigated the force sensitivity of multilayer graphene mechanical resonators coupled to superconducting cavities.<sup>[233]</sup> The multilayer graphene flake is clamped between poly topping and niobium support electrodes, hanging over and coupled to a superconducting LC cavity through the capacitance. A DC voltage is applied to control the

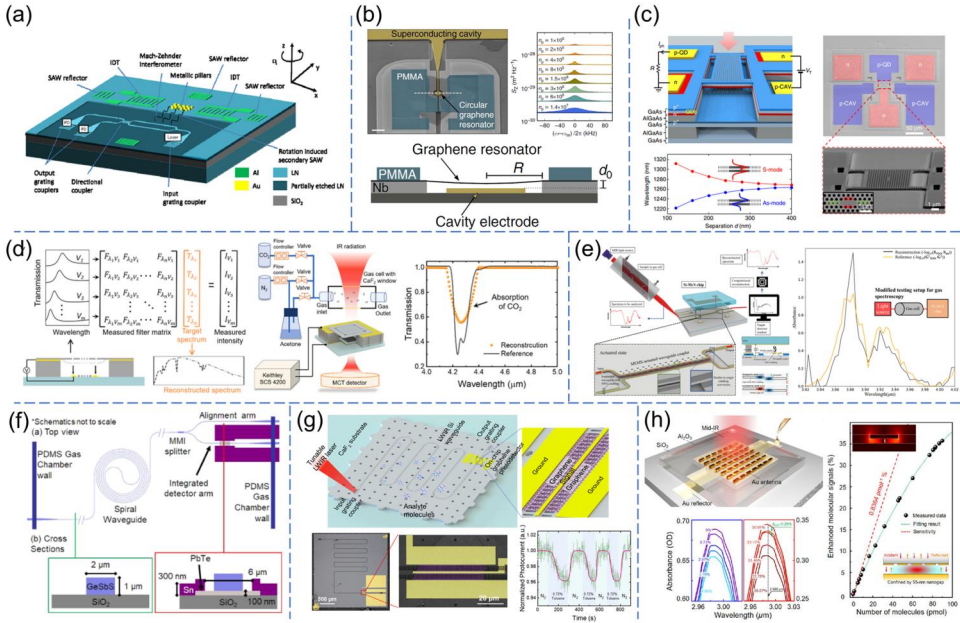


**Figure 7.** Photonic physical, chemical, and biological sensing nanosystems. (a) AO gyroscope consisting of a photonic MZI and two inherently matched piezoelectric SAW resonators. Reproduced with permission from Ref.<sup>[38]</sup>; (b) optomechanical mass sensor featuring multilayer graphene mechanical resonator coupled to superconducting cavity. Reproduced with permission from Ref.<sup>[233]</sup>; (c) integrated nano-opto-electro-mechanical sensor for spectrometry and nanometrology. Reproduced with permission from Ref.<sup>[234]</sup>; (d) MIR computational free-space spectrometer based on MEMS-tunable FP PCS filter. Reproduced with permission from Ref.<sup>[249]</sup>; (e) MIR computational waveguide spectrometer based on MEMS-reconfigurable directional coupler. Reproduced with permission from Ref.<sup>[258]</sup>; (f) MIR chalcogenide glass waveguide sensor monolithically integrated with a PbTe detector. Reproduced with permission from Ref.<sup>[260]</sup>; (g) heterogeneously integrated graphene photodetector, Si waveguide sensor, and CaF<sub>2</sub> substrate for on-chip zero-bias LWIR spectroscopic sensing. Reproduced with permission from Ref.<sup>[39]</sup>; (h) nanoantenna SEIRA platform with integrated nanofluidic channel fabricated by wafer bonding. Reproduced with permission from Ref.<sup>[264]</sup>

separation between the graphene mechanical resonator and the superconducting cavity. With the increased cavity pump photon population  $n_p$ , the imprecision force noise firstly decreased at low  $n_p$  and increased at high  $n_p$ , which is mainly attributed to the enhanced damping caused by the optomechanical back-action. Consequently, the best force sensitivity in this device is  $390 \pm 30$  zN·Hz<sup>-1/2</sup> by operating at a low pump photon condition of  $4 \times 10^5$  and the careful design of thermal anchoring. While optomechanical sensors enable extraordinary sensitivity with miniaturized optomechanical cavities and are promising for the development of chip-scale integrated sensing systems, their practice applications are still hampered by the difficulty of integrating tuning and read-out structures. In 2017, Zobenica et al. presented a nano-opto-electro-mechanical system (NOEMS) that combines three functionalities of transduction, actuation, and detection on a single chip, to demonstrate a high-resolution spectrometer with only a micrometer-scale footprint.<sup>[234]</sup> As depicted in Figure 7(c), the spectrometer consists of two evanescently coupled photonic crystal membranes with a gap of 240 nm, which support two degenerated cavity modes splitting into combined symmetric and antisymmetric modes. The gap between two membranes can be actively tuned with different applied DC voltage, providing a large resonance wavelength tuning range in the cavity. Meanwhile, a layer of InAs quantum dots is grown at the center of the upper membrane, and the optical read-out is done by measuring the photocurrent from the photodiode. With this integrated optomechanical sensor that embodies the features of direct wavelength and displacement detection, the authors demonstrated a spectrometer that successfully measured a narrow gas absorption line (16 pm). Moreover, further integration of the optomechanical sensing platform with a light source will open the way to fully integrated sensor systems requiring no

external optical connections. For more information on the electro-optomechanical sensing systems, we also refer readers to the above-mentioned topical reviews.<sup>[19,158]</sup>

### 3.3.2. Photonic chemical and biological sensing nanosystems

Spectrometers play a crucial role in spectroscopic sensing applications when using broadband light incidence and detection. A variety of miniaturized spectrometer designs have been unveiled over the past three decades.<sup>[235]</sup> According to their working principles, the reported on-chip spectrometers can be classified into four main categories. The first three categories are (i) those that feature dispersive optics to split light toward spatially separated detectors,<sup>[127,236]</sup> (ii) those that use narrowband filters to preferentially transmit particular spectral components to different detectors<sup>[237,238]</sup> or use a single tunable filter together with a single detector,<sup>[239]</sup> and (iii) Fourier transform spectrometers based around an interferometer array<sup>[240]</sup> or a single tunable interferometer,<sup>[241]</sup> in which the interferograms are collected by a detector array in a single capture or by a single detector over time, respectively. In the past decade, a fourth category has emerged as a new paradigm of miniaturized spectrometers. “Reconstructive” or “computational” spectrometers use complex algorithms to approximate or “reconstruct” an incident light spectrum from precalibrated spectral response information encoded within a set of broadband filters<sup>[242–244]</sup> or detectors.<sup>[245,246]</sup> Such systems can harness not only technological advances in hardware but also the development of new computational approaches, in particular those based on compressive sensing<sup>[247]</sup> and machine learning.<sup>[248]</sup> Very recently, this paradigm has also been reported to be performed by a single tunable filter, interferometer, or detector, in which the distinctive spectral response characteristics are encoded over time, enabling further miniaturization of the spectrometers. Chang et al. from Prof. Lee’s group at NUS developed an MIR computational spectrometer based on a MEMS-tunable FP PCS filter, as shown in Figure 7(d).<sup>[249]</sup> The normalized transmission of the filter as a function of both applied voltage and wavelength was learned and discretized into a matrix. Any unknown spectrum was then reconstructed by solving the matrix equation shown in Figure 7(d). The absorption spectra of CO<sub>2</sub> around 4.26  $\mu\text{m}$  and acetone around 5.75  $\mu\text{m}$  were successfully reconstructed. Yuan et al. from Prof. Xia’s group at Yale University demonstrated a wavelength-scale MIR spectrometer utilizing a single tunable BP photodetector based on the Stark effect.<sup>[250]</sup> The photodetector responsivity as a function of both applied biasing displacement field and wavelength was learned and discretized into a matrix. With an active area footprint of only  $9 \times 16 \mu\text{m}^2$ , the spectrometer realized a moderate resolution of  $\sim 90 \text{ nm}$  in the wavelength range from 4 to 7  $\mu\text{m}$ . The CO<sub>2</sub> absorption fingerprint was also successfully captured by this spectrometer. Later, Yoon et al. reported a computational spectrometer based on a single van der Waals (vdW) junction with an electrically tunable transport-mediated spectral response.<sup>[251]</sup> A MoS<sub>2</sub>/WSe<sub>2</sub> heterojunction was chosen because of its distinct spectral response due to the gate-tunable photovoltaic effect from the visible to the NIR. A high spectral resolution of 3 nm and a broad operation bandwidth from 405 to 845 nm were achieved. Single-detector computational spectrometers similarly leveraging voltage-tunable photoresponse have also been realized by ReS<sub>2</sub>/Au/WSe<sub>2</sub> heterojunction in the NIR,<sup>[252]</sup> BP/MoS<sub>2</sub> heterojunction in the MIR,<sup>[253]</sup> and AlGaAs/GaAs p-graded-n junction in the visible/NIR.<sup>[254]</sup> Advances have also been witnessed in waveguide-based computational spectrometers in recent two years. Spectrometers utilizing a single tunable waveguide structure such as a photonic molecule consisting of two identical MRRs,<sup>[255]</sup> a six-stage cascaded MZI,<sup>[256]</sup> and a multimode cavity formed by a waveguide array and delay lines,<sup>[257]</sup> are demonstrated with pm-level resolution and broad bandwidth of over 100 nm in the NIR. Nonetheless, these works rely on power-consuming thermo-optic tuning. Electrostatic MEMS enables effective tuning with ultralow power consumption. Qiao et al. presented an MIR spectrometer using an electrostatic-MEMS-reconfigurable directional coupler as shown in Figure 7(e).<sup>[258]</sup> The transmission at the through/drop port is a function of both applied voltage and wavelength. The spectrometer features a large bandwidth of 350 nm and a fine

resolution of 3 nm. Using it, the broadband absorption spectrum of  $\text{N}_2\text{O}$  from 3.82 to 4.02  $\mu\text{m}$  was retrieved. Although the spectroscopic sensing demonstrations in the above-mentioned works were performed using external gas cells, spectroscopic sensing nanosystems featuring on-chip integration of sensors and spectrometers can be envisioned, especially for the waveguide-based scheme.

Besides spectrometers, another way to implement spectroscopy is to use tunable light sources. A fully integrated photonic chip sensor for NIR trace gas spectroscopy was demonstrated by IBM in 2019.<sup>[259]</sup> This sensor comprises a heterogeneously integrated III-V laser/detector chip coupled to a Si external cavity for broadband tuning, a long waveguide element ( $>20\text{ cm}$ ) for ambient methane sensing, and a sealed methane reference cell for real-time calibration. Within the external cavity (prior to the Bragg reflector), a phase-heater and microring tuning element provide synchronized tuning to maintain broadband tunability ( $>2\text{ nm}$ ) while maintaining single-mode lasing operation. Full-stack testing of the integrated sensor chip yielded sub-100  $\text{ppmv}\cdot\text{Hz}^{-1/2}$  sensitivity. Moving to the MIR, the integration progress was first observed at the detector part. Su et al. demonstrated an MIR chalcogenide glass waveguide sensor monolithically integrated with a PbTe detector, as illustrated in Figure 7(f).<sup>[260]</sup> The PbTe channel, metal contacts, and chalcogenide glass waveguide were deposited and patterned orderly by liftoff procedures on a Si substrate. Using a 5-mm-long spiral waveguide and biasing the detector at 100  $\mu\text{A}$  current, the integrated sensing system realized absorption spectroscopic sensing of methane gas with an LoD of 1% at its absorption peak of 3.31  $\mu\text{m}$  wavelength. Nonetheless, chalcogenides are generally not considered compatible with CMOS foundry processes. For Si photonics, the MIR waveguide sensors with integrated detectors were first witnessed by flip-chip bonding of MEMS thermopile IR detector onto SOI waveguide sensors.<sup>[195]</sup> On-chip spectroscopic sensing of  $\text{N}_2\text{O}$  at around 3.89  $\mu\text{m}$  was demonstrated and an LoD of 0.18% was estimated. For wavelengths beyond 4  $\mu\text{m}$ , the development of waveguide-integrated photodetectors faces challenges from both waveguide platforms and photodetection technologies. For waveguide platforms, although the suspended Si platform can fully leverage Si's transparency window up to 8  $\mu\text{m}$ , the suspended structures pose difficulties in following processes and further integration. For photodetection technologies, graphene is a suitable choice for waveguide-integrated photodetectors at long MIR wavelengths as discussed above. The gapless nature endows graphene with high-speed broadband photoresponse from UV to THz while also resulting in a large dark current when bias is applied. Zero-bias operation is thus preferred, which, however, sacrifices the photocarrier collection efficiency. Additionally, graphene's absorption becomes weaker at longer IR wavelengths as the photon energy decreases. Thus, a strategy is desired to improve the performance of graphene photodetectors to meet the requirement of MIR on-chip sensing systems. Ma et al. developed waveguide-integrated zero-bias photodetectors operating beyond 6  $\mu\text{m}$  based on heterogeneous integration of graphene photodetectors and Si waveguides on  $\text{CaF}_2$  substrates, as shown in Figure 7(g).<sup>[39]</sup> To address the waveguide platform issue, a simple transfer printing method utilizing a microstructured polydimethylsiloxane (PDMS) stamp was developed to facilitate the transfer of large-scale membranes containing waveguides from the SOI device layer onto  $\text{CaF}_2$  substrates with high yield. The transfer-printed SOCF waveguides show low losses in the broad wavelength range of 6.3–7.1  $\mu\text{m}$ . The photodetection technology issue was addressed by employing waveguide-integrated graphene photodetectors with a ground-signal-ground (GSG) electrode configuration. The signal electrode on top of the waveguide not only enables zero-bias photodetection by locally changing graphene's doping level and forming p-p<sup>+</sup> junctions at its both sides but also provides plasmonic enhancement of the electric field as two hot spots its both sides. The overlap leads to a significant performance improvement of the graphene photodetector. The graphene photodetector achieved a broadband responsivity of  $\sim 8\text{ mA/W}$ , which is comparable with those of NIR counterparts. They further integrated the graphene photodetector with a SOCF folded waveguide and demonstrated on-chip absorption sensing using toluene as an example. 0.72% toluene was experimentally detected.



The above results pave the way to the realization of chip-scale, low-cost, and low-power-consumption MIR spectroscopic sensing systems. Nevertheless, more efforts are needed to integrate light sources and/or spectrometers with the sensors and detectors.

The integration of microfluidics with sensors is also important. Microfluidic channels not only deliver liquid and gas analytes to the vicinity of sensors but also confine the analytes to enhance their interaction with the external optical fields of the sensors. Microfluidics, typically made of PDMS and fabricated by standard soft lithography and mold-replica techniques, has been widely adopted in both free-space and waveguide sensors.<sup>[19,23,261]</sup> Nonetheless, the light-matter interaction enhancement provided by microfluidics is limited as both the hot spots of plasmonic sensors and the evanescent fields of dielectric sensors are at the scale of only tens to hundreds of nanometers. To overcome this bottleneck, the concept of hybrid plasmonics-nanofluidics has been proposed and demonstrated to be effective.<sup>[262,263]</sup> Recently, Xu et al. developed a nanoantenna SEIRA platform with an integrated nanofluidic channel, as shown in Figure 7(h).<sup>[264]</sup> The nanofluidic channel was fabricated using a low-temperature interfacial heterogeneous direct bonding technique to bond  $\text{Al}_2\text{O}_3$  with  $\text{SiO}_2$  at the wafer level. The transition layer thickness, which is also the maximum error for nanogaps caused by the bonding, is only 3.3 nm. Thus, the nanometer-scale gap distance can be precisely controlled by the  $\text{SiO}_2$  etching depth. With a 55 nm nanogap, A small acetone concentration change of 0.29% was distinguished and an ultrahigh sensitivity ( $0.8364 \text{ pmol}^{-1}\%$ ) was achieved. The nanofluidic techniques can also be potentially employed in waveguide sensors to improve their sensing performances.

#### 4. Optical communication, computing, and imaging

In addition to the above-reviewed sensing applications, communication, computing, and imaging are other important application categories of optical devices in the IoT and 5G era, and often share similar technologies during the evolution from optical MEMS and nanophotonics to photonic nanosystems.

##### 4.1. Optical MEMS for communication, computing, and imaging applications

Optical beam steering is critical in various applications including optical communication,<sup>[17,265]</sup> imaging,<sup>[266,267]</sup> light detection and ranging (LiDAR),<sup>[268]</sup> optical coherence tomography,<sup>[269]</sup> and laser machining.<sup>[270]</sup> Principally, optical beam steering requires the dynamical forming or orienting of a focused or collimated laser beam. For many applications, beam scanning over a 2D angular range is required. For example, in LiDAR applications, beam scanning is required to reconstruct the 3D images with accurate distance information; in optical communications, the variable optical attenuator (VOA) is used to maintain a flattened gain profile after the multiplexed signal has been demultiplexed.

Current beam steering technologies rely mostly on MEMS-based tuning, through either electrothermal,<sup>[271,272]</sup> electrostatic,<sup>[273,274]</sup> piezoelectric,<sup>[275,276]</sup> electromagnetic,<sup>[277,278]</sup> or hybrid mechanisms.<sup>[279,280]</sup> The MEMS approach for beam steering typically has unrivaled advantages in terms of size, speed, and cost over other types of laser scanners, making them commercial-ready and ideal for a wide range of applications. One of the most common approaches to enable MEMS actuation is the electrothermal method, known for its large displacement and high force output. While well-studied U-shaped and V-beam actuators only allow one directional displacement without self-maintained states,<sup>[281–283]</sup> Chen et al. proposed a novel latched H-beam actuator to demonstrate two-way motion and bi-stable actuation for optical switch application, as presented in Figure 8(a).<sup>[40]</sup> The electrical load can be applied to one side of the H-beam, which will deform to generate an elongation along the designed direction. The bi-stable function is enabled by the buckle spring beams on both sides of the device which are anchored on the

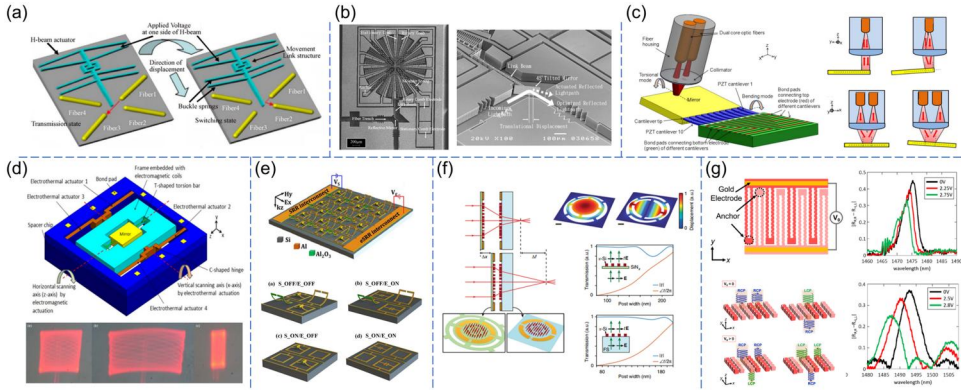


**Figure 8.** Optical MEMS for communication, computing, and imaging applications. (a) Electrothermal MEMS optical switch. Reproduced with permission from Ref.<sup>[40]</sup>; (b) MEMS VOA using electrostatic rotary comb actuators. Reproduced with permission from Ref.<sup>[284]</sup>; (c) piezoelectric MEMS 3D VOA with combined rotational and translational effects. Reproduced with permission from Ref.<sup>[285]</sup>; (d) hybrid electromagnetic and electrothermal MEMS 2D scanning mirror. Reproduced with permission from Ref.<sup>[28]</sup>; (e) MEMS reconfigurable interpixelated metasurface for independent tuning of multiple resonances in the THz. Reproduced with permission from Ref.<sup>[298]</sup>; (f) MEMS-tunable dielectric metasurface lens. Reproduced with permission from Ref.<sup>[299]</sup>; (g) MEMS-tunable chiral metasurfaces. Reproduced with permission from Ref.<sup>[300]</sup>

substrate. The buckle spring can maintain its original arched shape unless enough force is applied to overcome the energy barrier for the state transition. With such H-beam actuators,  $2 \times 2$  optical switches are demonstrated with a switching time of 5 ms under a 25 V DC pulse and an insertion loss of 0.8 dB. Another well-deployed actuation mechanism for VOA is electrostatic actuation. In 2006, Yeh et al. proposed a MEMS VOA using electrostatic rotary comb actuators, as presented in Figure 8(b).<sup>[284]</sup> While axial comb actuators are commonly used in a majority of the planar configurations, the rotary comb actuators may achieve a wider attenuation range in faster dynamic response and lower driving voltages. The rotation angles of the VOA are determined by the balance between electrostatic torques from the comb actuators and mechanical torques stored at the deformed springs. By utilizing  $45^\circ$  tilted mirrors and mender springs, this rotary VOA exhibits attenuation above 40 dB and a switching time of 3 ms, given the required DC voltage of only 4.2 V. Piezoelectric actuation has also been applied to achieve large mechanical displacements or rotation angles in VOA. By leveraging lead zirconate titanate (PZT) cantilever beams, Koh et al. demonstrated a 3D MEMS VOA with combined rotational and translational effects, as depicted in Figure 8(c).<sup>[285]</sup> With multilayers of Pt/Ti/PZT/Pt/Ti deposited as electrode materials on top of Si beams, the cantilevers will bend under the DC bias. In this PZT 3D MEMS VOA, ten individual PZT cantilevers are arranged in parallel along one side of the Si mirror. As a result, both bending mode and torsional mode can be achieved by applying balanced or imbalanced biasing voltages, enabling the mirror to rotate along both the  $x$ - and  $y$ -axes. Particularly, the bending mode of this VOA only requires a bias of 1 V to achieve a 40 dB dynamic range, whereas 1.8 V for the same amount of attenuation during the torsional mode. Straightforwardly, 2D raster scanning applications by the same piezoelectric-driven mirror were investigated.<sup>[275,276]</sup> Furthermore, Koh et al. proposed a simplified design featuring a single S-shaped PZT piezoelectric actuator, which can also be operated at both bending and torsional modes. 2D scanning mirrors based on this design have also been demonstrated.<sup>[286,287]</sup> Hybrid actuation mechanisms, i.e., the combination of two or more of the actuation mechanisms, can enable unique and sophisticated functions in optical beam steering. Figure 8(d) presents an approach demonstrating 2D scanning using a single mirror with integrated electrothermal and electromagnetic actuation mechanisms.<sup>[28]</sup> The electromagnetic actuation is adopted for the fast-scanning axis due to its low driving voltage and CMOS compatibility. The electrothermal actuation is adopted for the slow-scanning axis due to its large static or dynamic displacement characteristics. As a result, an

optical scan angle of  $\pm 1.5^\circ$  for the 74 Hz vertical scan at 12 mW for electrothermal actuation and that of  $\pm 10^\circ$  for the horizontal scan frequency of 202 Hz at 1.26 mA and 1 V bias voltage for electromagnetic actuation. Similarly, 3D VOA applications based on the same hybrid-driven mirror were also demonstrated.<sup>[288,289]</sup>

On top of the MEMS mirror-based beam steering technologies, recently flourishing tunable metasurfaces hold the promise of integrated beam steering devices with high tuning speed and a wide tuning range. The combination of advanced MEMS technology with metasurfaces has enabled various applications, ranging from fundamental functions, such as the modulation of intensity,<sup>[290]</sup> wavelength,<sup>[291]</sup> bandwidth,<sup>[292]</sup> and electromagnetically induced transparency (EIT),<sup>[293]</sup> to more sophisticated devices, such as beam scanner,<sup>[294]</sup> tunable waveplate,<sup>[295]</sup> and resonant cloaking.<sup>[296]</sup> The tunability of metasurfaces also provides a new degree of freedom to manipulate the light-matter interaction in the subwavelength regime.<sup>[297]</sup> In 2015, Pitchappa et al. reported a microelectromechanically reconfigurable interpixelated metasurface for independent tuning of multiple resonances in the THz spectral region, as shown in Figure 8(e).<sup>[298]</sup> An electrically isolated split ring resonator (SRR) and an electrical split ring resonator (eSRR) are arranged to form the metamaterial supercell. Each of the unit cells is independently addressed and can be programmed. Both the magnetic resonance and electrical resonance can be excited due to both asymmetry and symmetry existing in the metamaterial supercell, with the resonance at 0.59 and 0.45 THz, respectively. To achieve active reconfiguration, the SRRs are partially released and their position can be electrostatically controlled by the DC bias. Active switching of either magnetic or electrical resonance only, or simultaneous switching of both, has been experimentally demonstrated, while the electrical resonance can be switched from 0.45 to 0.4 THz, the magnetic resonance can be switched from 0.59 to 0.35 THz. With both tuning of SRR and eSRR, the excitation of both magnetic and electrical resonance is located at 0.375 THz. This programmable metasurface has immense potential to demonstrate tunable filters, spatial light modulators, or gradient metamaterials. In the optical regime, all-dielectric metasurfaces offering a dissipationless alternative to current metallic ones to manipulate light at the nanoscale, are very versatile for wavefront control and beam steering. In 2018, Arbabi et al. demonstrated MEMS-tunable dielectric metasurface doublets, as shown in Figure 8(f), with one stationary metasurface on a glass substrate and a moving metasurface on a SiN<sub>x</sub> membrane.<sup>[299]</sup> The moving membrane can be electrostatically actuated to change the distance between the two metasurfaces, forming a focal length-tunable varifocal lens. With the well-designed high-contrast dielectric metasurfaces, the lens achieved more than 4% change in the optical power upon a 1- $\mu$ m movement of the moving membrane. The potential scanning frequency can reach a few kHz, which is suitable for applications in ultra-compact optical systems. Active control of metasurfaces can also offer numerous new opportunities for diverse optical engineering such as tuning of guided-mode resonances or optical polarization. In 2021, Kwon et al. demonstrated active control of strong chiroptical responses in dielectric metasurfaces with reflective circular dichroism (CD).<sup>[300]</sup> As presented in Figure 8(g), the metasurfaces are composed of two sets of doped Si nanostructures, which can be electrostatic force-driven to change the gap size between two neighboring beams in different sets. When the structure is at its initial state, the right circular polarized (RCP) light will transmit without a flip of the handedness, while the left circular polarized (LCP) light will transmit with reversal of handedness. When the bias is applied, the chiroptical properties of the metasurfaces will be continuously modulated, consequently, exhibiting negligible chiroptical responses at the target wavelength. The devices enable continuous control of CD by induced electrostatic forces from 0.45 to 0.01 with an electrical bias below 3 V.

#### 4.2. Nanophotonics for communication, computing, and imaging applications

Advancing from optical MEMS for communication and imaging applications, where MEMS-actuated mirrors are the dominating configuration, the advancement in on-chip integrated

nanophotonics has made the device more compact and scalable over the past several years. Among these nanophotonic devices, large-scale photonic switches are one of the essential building blocks in modern-day communication networks, computing units, and data centers that process a high amount of data flow. **Figure 9(a)** shows large-scale Si photonic switches based on moveable directional couplers.<sup>[29]</sup> A total of  $50 \times 50$  photonic switches working in the NIR wavelength range can be individually actuated by an electrostatic MEMS cantilever, achieving arbitrary light rerouting. The actuation voltage required is 14 V and the switching time is  $2.5 \mu\text{s}$ , while the extinction ratio is 26 dB. However, due to the thermal-induced metal bending of the cantilever, inevitable fabrication deviations between devices will lead to non-uniform actuation voltage required at every single switch, and ultimately increase the control difficulties of the system. As a result, the same group demonstrated an even larger photonic switch array consisting of  $64 \times 64$  switches with MEMS-actuated vertical adiabatic couplers, as shown in **Figure 9(b)**.<sup>[301]</sup> The improved vertical couplers with stoppers can control the light coupling more precisely and robustly. Consequently, the switching speed has increased to  $0.91 \mu\text{s}$  and the extinction ratio reaches 60 dB over a wide operation bandwidth of 300 nm. The use of electrostatic actuation for MEMS photonic switch operation has seen more applications and configurations in recent years, due to the excellence in low power, fast operation speed, and scalability.<sup>[302–304]</sup> While most of the MEMS photonic switches have been developed for NIR operation, it is important to extend the working wavelengths to MIR to further complete the functional device library of PICs. Qiao et al. demonstrated the first MEMS photonic switch in MIR wavelengths of  $3.85\text{--}4.05 \mu\text{m}$ .<sup>[305]</sup> Due to the device dimension upscaling to transmit the MIR signal, a flip-chip bonding technique was adopted to create a larger vertical space for actuation. The fabricated device has achieved an actuation voltage of 90 V and a response time of  $8.9 \mu\text{s}$  with a  $-20 \text{ dB}$  bandwidth of 100 nm. In addition to switches, tunable power couplers, phase shifters, and add-drop filters have also been realized through the integration of Si photonics and electrostatic MEMS actuators,<sup>[306,307]</sup> driven by the European Horizon 2020 project MORPHIC (Mems-basemoreO-power Reconfigurable PHotonic ICs) aiming to develop a platform for programmable PICs.<sup>[308]</sup> Like the evolution of

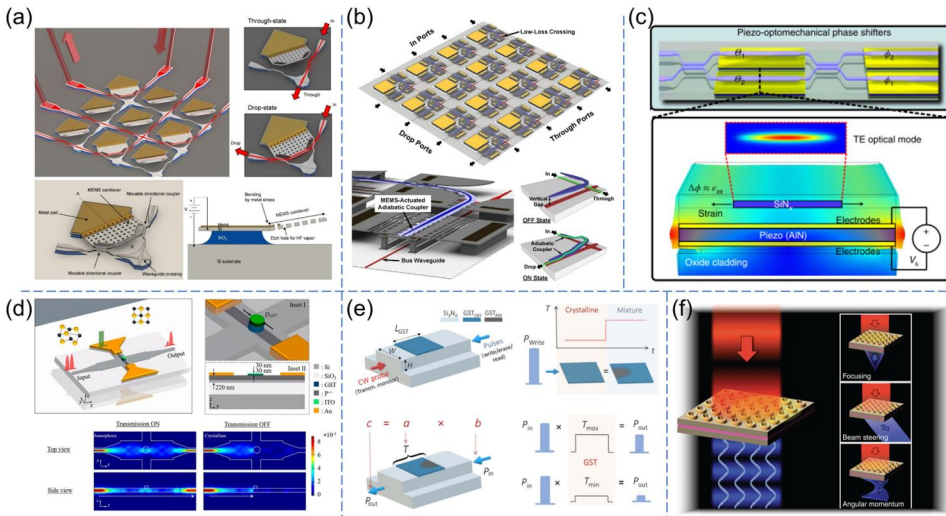


**Figure 9.** Nanophotonics for communication and imaging applications. (a) NIR  $50 \times 50$  photonic switches with MEMS-actuated directional couplers. Reproduced with permission from Ref.<sup>[29]</sup>; (b) NIR  $64 \times 64$  photonic switches with MEMS-actuated vertical adiabatic couplers. Reproduced with permission from Ref.<sup>[301]</sup>; (c) MIR photonic switch with MEMS-tunable waveguide coupler and fabricated by flip-chip bonding. Reproduced with permission from Ref.<sup>[305]</sup>; (d) PCM-based multilevel photonic memristive switch. Reproduced with permission from Ref.<sup>[313]</sup>; (e) photonic in-memory computing using a waveguide-integrated PCM cell. Reproduced with permission from Ref.<sup>[30]</sup>; (f) optical phased-array sources based on nonlinear metamaterial nanocavities for various beam-shaping applications. Reproduced with permission from Ref.<sup>[322]</sup>



electronic integrated circuits from application-specific integrated circuits (ASICs) to field-programmable gate arrays (FPGAs), programmable PICs have emerged as a powerful technology for advanced applications including high-speed communication, neuromorphic computing, and quantum information processing.<sup>[309]</sup> Besides electrostatic actuation, piezoelectric actuation is another demonstrated MEMS tuning mechanism for programmable PICs.<sup>[310]</sup> Dong et al. introduced a large-scale programmable Mach-Zehnder mesh (MZM) platform made in a 200 nm CMOS foundry.<sup>[311]</sup> The MZM is composed of MZIs with piezo-optomechanical phase shifters as illustrated in Figure 9(c). An applied voltage across the AlN piezoelectric actuator results in strain imparted to the optical waveguide, enabling low-loss propagation with phase modulation at greater than 100 MHz in the visible-NIR wavelengths. Moreover, the vanishingly low hold-power consumption of the piezoelectric actuators enables these PICs to operate at cryogenic temperatures, paving the way for a fully integrated device architecture for a range of quantum applications.

In recent years, a novel type of photonic switch based on phase change material (PCM) has gained research interest due to its miniaturization and nonvolatility. One common PCM being widely explored is germanium-antimony-tellurides (GST), which can be changed between amorphous and crystalline states under external excitation.<sup>[312]</sup> Figure 9(d) has reported a multi-level optical memristive switch using PCM.<sup>[313]</sup> A small dot of GST is deposited on top of a photonic multimode interferometer with p-doped Si as conducting channel. When the GST is changed to the amorphous state under an external voltage pulse, the insertion loss could reach 4 dB while the transmission contrast between amorphous and crystalline states could reach 18.59 dB. Moreover, the transmission could be further divided into multiple states depending on the amorphous level of the GST, thus achieving multilevel switching. PCM multilevel memristive switch is further utilized to realize in-memory computing.<sup>[30]</sup> Figure 9(e) sketches the operation principle. The device relies on the near-field coupling between the propagating optical mode inside the waveguide and a GST segment placed on top of the waveguide to absorb enough energy to crystallize or amorphize. Because most PCMs have a nonnegligible imaginary RI in the visible and NIR wavelength range, light is attenuated in different amounts depending on the phase configuration of the material, which gives rise to differentiable transmitted signals, thus encoding information. A write pulse  $P_{\text{Write}}$  is used to program a specific level of transmittance  $T$  of the device, which relies on the multilevel conditioning of the material. A second low-energy read pulse  $P_{\text{in}}$  propagates through the device, experiencing a transmittance given by the current phase configuration of the GST cell as conditioned by the pulse  $P_{\text{Write}}$ , but does not induce any change to the material. The power of the pulse of  $P_{\text{in}}$  at the output port,  $P_{\text{out}} = T(P_{\text{Write}}) \times P_{\text{in}}$ , is the result of the multiplication  $a \times b$  by mapping the multiplicand  $a$  to  $T$  and the multiplier  $b$  to  $P_{\text{in}}$ . The idea of multiplication using a single PCM memory cell is subsequently extended to demonstrate matrix-vector operations using multiple PCM memory cells. More usage of different PCMs on different photonic devices has been reported to realize nonvolatile reconfigurable photonics,<sup>[314,315]</sup> with demonstrations ranging from basic switch,<sup>[316]</sup> memory,<sup>[317]</sup> and synapse<sup>[318]</sup> functions, to advanced applications such as convolutional processing<sup>[319]</sup> and neuromorphic computing.<sup>[320]</sup>

Apart from the waveguide-based nanophotonic devices for on-chip communication and computing applications, nanoantenna-based nanophotonic devices have brought advancements to free-space communication and imaging applications. Dregely et al. demonstrated tunable optical beam steering with plasmonic nanoantennas.<sup>[321]</sup> Using the photoluminescence technique, the distance dependence of the power transmission over the nanoantennas transmitter was quantified, and directional control over a wide angle of  $29^\circ$  was achieved through adjustment of the incident wavefront. Not only the direction of optical power can be altered, but Wolf et al. have also proposed nonlinear metamaterial nanocavities with the capability of producing arbitrary beam shape and polarization, as shown in Figure 9(f).<sup>[322]</sup> Through optical pumping of the nanocavity, a localized, phase-locked, and nonlinear resonant polarization is induced as a source for higher-



order resonance. By changing the nanocavity design, two second harmonic phased-array sources have been demonstrated around  $5\ \mu\text{m}$  wavelength for different optical functions, one as a beam splitter, and the other as a polarizing beam splitter.

#### 4.3. Photonic nanosystems for communication, computing, and imaging applications

On top of the individual nanophotonic devices, there are more integrated photonic nanosystems for real-world communication, computing, and imaging applications that have been demonstrated over the past few years. The synergy between photonic nanosystems and self-sustainable wearable electronics has brought a new dimension to the research field of wearable photonics.<sup>[323,324]</sup> Owing to the high-speed and robust photonic signal transmission, the signals from wearable electronics can be coupled with optical signals for more versatile applications such as robust nanophotonic human-machine interfaces and optical-biometric encryptions. Specifically, textile-based triboelectric nanogenerators (T-TENG) which can be fully integrated into daily worn clothes offer unique advantages of large output voltage, broad material versatility, cost-effectiveness, and good scalability,<sup>[325–328]</sup> and could significantly promote the development of the next generation wearable photonics. Dong et al. from Prof. Lee's group at NUS first demonstrated self-sustainable photonic modulation and continuous force sensing with a wearable triboelectric/AlN nano-energy-nano-system, as shown in Figure 10(a).<sup>[329]</sup> The high-voltage output from T-TENG matches well with the need to boost the efficiency of AlN modulators due to its moderate Pockels effect. At the same time, the AlN modulator could enable the open circuit operation mode of T-TENG, which makes it possible for continuous force sensing regardless of operating speeds. With such integration, optical Morse code transmission and human motion monitoring were demonstrated. On top of the force sensing, a wearable triboelectric-human-machine interface (THMI) with robust nanophotonic readout has been demonstrated.<sup>[330]</sup> Due to the conventional electrical readout in pulsed signals of THMI, there are inevitable losses and unstable information transfer processes.<sup>[331]</sup> The use of electro-optic-based AlN readout with negligible charge flow nature has brought unique advantages to the THMIs such as high-speed, stable,

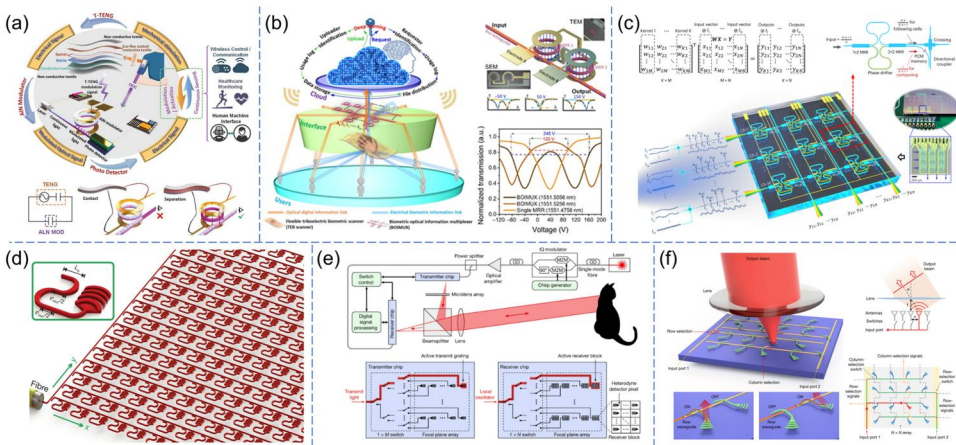


**Figure 10.** Photonic nanosystems for communication, computing, and imaging applications. (a) Integrated wearable photonic system with self-sustainable photonic modulation and continuous force sensing using T-TENG and AlN photonic MRR. Reproduced with permission from Ref.<sup>[329]</sup>; (b) biometrics-protected optical communication enabled by deep learning-enhanced triboelectric/photonic synergistic interface. Reproduced with permission from Ref.<sup>[31]</sup>; (c) photonic tensor core for in-memory computing using continuous-time data representation. Reproduced with permission from Ref.<sup>[337]</sup>; (d) large-scale active-controlled nanophotonic phased array working in the NIR with  $64 \times 64$  optical nanoantennas. Reproduced with permission from Ref.<sup>[342]</sup>; (e) universal solid-state 3D imaging sensor on Si photonics platform. Reproduced with permission from Ref.<sup>[32]</sup>; (f) Si photonics LiDAR based on MEMS platform with  $128 \times 128$  electrostatically actuated FPSA. Reproduced with permission from Ref.<sup>[353]</sup>

real-time, and low-loss information transfer. As a result, the practical application of a smart glove with continuous real-time robotics control and VR/AR interaction has been validated. Since wearable sensors carry lots of personalized information such as motion habits that can be uniquely associated with specific users, it is, therefore, an ideal candidate for biometric encryption of optical data transmission. At the same time, due to privacy concerns over facial recognition data protection, contact-based biometrics such as gloves and smart mats are favored so that more privacy can be controlled.<sup>[332–334]</sup> Together with the help of deep learning algorithms, biometrics-protected optical communication by triboelectric/photonic synergistic interface was presented, as shown in Figure 10(b).<sup>[31]</sup> The optical signal was loaded with biometric information at zero power consumption, and through multiplexing and demultiplexing process with a deep learning algorithm, the identification of 15 different users was demonstrated at an accuracy of 95% irrespective of biometric information data types. Such integration technology has certainly broadened the applications of secured smart home control and secure communication while offering a low-cost and easy-to-access solution.

As discussed in the last section, photonic matrix-vector multiplication (MVM) is emerging as a next-generation alternative to electronic MVM with the advantages of low latency, low energy consumption, and high degrees of freedom (DOFs).<sup>[335]</sup> In the past decade, photonic MVM using PICs has flourished.<sup>[336]</sup> In all the reported PIC-based MVM processors, two DOFs are accessible by the input data, that is, space and wavelength, allowing a 2D array input. Very recently, Dong et al. demonstrated a computing architecture in hardware that allows 3D array inputs for higher-dimensional MVM by adding an additional RF DOF.<sup>[337]</sup> Figure 10(c) conceptually illustrates the data architecture and working principle of the photonic tensor core for in-memory computing using continuous-time data representation. The RF modulation of photonic signals is introduced to increase parallelization, adding an additional dimension to the data alongside spatially distributed nonvolatile PCM memories and wavelength multiplexing. Higher-dimensional processing is leveraged to configure such a system to an architecture compatible with edge computing frameworks. This system achieves a parallelism of 100, two orders higher than implementations using only the spatial and wavelength degrees of freedom, providing a viable path for ultraparallel photonic computing to deal with the surging computational load imposed by IoT and 5G.

The advancement from optical MEMS and nanophotonics to photonic nanosystems has also been witnessed in imaging technologies. Apart from MEMS mirror, optical phased array (OPA) is another popular technology for beam steering. Initially only demonstrated in one-dimension or small-scale two-dimensions,<sup>[338–341]</sup> OPA has certainly seen larger-scale integration with compact chip size. Figure 10(d) depicts a large-scale nanophotonic phased array working in NIR wavelengths.<sup>[342]</sup> The array consists of  $64 \times 64$  optical nanoantennas that have been precisely balanced in power and aligned in phase to generate radiation patterns in the far field. Furthermore, dynamic beam steering and shaping have been demonstrated with an  $8 \times 8$  array through thermal-optic tuning. Further integration of phased arrays with detector arrays to form a full 3D imaging system has been validated by Rogers et al. in Figure 10(e).<sup>[32]</sup> Owing to the advancements in monolithic integration of photonic and electronic circuits, the detector array has achieved an accuracy of 3.1 mm at a distance of 75 m while consuming only 4 mW light power. The system can be highly scalable and with the size of a consumer camera sensor, it could yield resolutions over 20 megapixels. With previously reported 3D imaging systems having a limited resolution of fewer than 20 pixels due to difficulties in providing the electrical and photonic connections at every pixel,<sup>[343–345]</sup> this work has certainly been a leap in terms of integration level by combining the optical heterodyne detector array with integrated electrical readout architecture to achieve over 20 times enhancement in resolution. On-chip integrated solid-state LiDAR has been a research frontier for photonic beam-steering devices with requirements of high speed, large field of view (FoV), and high resolution. Within the two common architectures of OPA and focal plane switch array (FPSA), the former type requires precise amplitude and phase control of the

optical antennas to achieve random access beam scanning.<sup>[346–349]</sup> The FPSA on the other hand could be easily integrated with a small footprint due to the camera-like optical system where multiple pixels could share a common LiDAR ranging unit.<sup>[345,350–352]</sup> Zhang et al. have recently demonstrated a MEMS-based Si photonics LiDAR with 16384 pixels, as shown in [Figure 10\(f\)](#).<sup>[353]</sup> The whole system consists of a  $128 \times 128$  FPSA of monolithically integrated grating antennas and MEMS-actuated photonic switches. The fabricated LiDAR has a wide FoV of  $70^\circ \times 70^\circ$ , a fine addressing resolution of  $0.6^\circ \times 0.6^\circ$ , and a narrow beam divergence of  $0.050^\circ \times 0.049^\circ$ . In addition, the device has a random-access beam addressing operation speed of sub-MHz and a 3D imaging resolution of 1.7 cm. The exceptional performance and CMOS compatibility have certainly paved the way for mass-produced commercial-ready 3D imaging sensors that can be used for autonomous vehicles, drones, robots, AR headsets, and smartphones. In addition to 3D imaging sensing applications, the FPSA can also be used in other applications that require optical beam steering, such as free-space optical communication and trapped-ion quantum computing.

## 5. Conclusion and outlook

Recent progress in the development of optical sensing and actuation technologies for diversified applications is comprehensively reviewed in this paper. The technology evolution trend from optical MEMS to nanophotonics and then to photonic nanosystems is clearly observed, pushing the improvement of device compactness, system integration level, performance, and functionality for the IoT and 5G era. The development milestones of optical sensing and actuation technologies surveyed in this review help us to foresee future development directions mainly as the next two points:

One is further improvement of the system integration level. Despite the impressive progress made in photonic nanosystems, large space remains for their development toward practical applications. Starting from free-space optical MEMS, many advancements have been witnessed in the integration of MEMS with photonic waveguide devices and PICs. However, the demonstrations are still limited to basic functional blocks and photonic ASICs for specific applications. Therefore, more efforts are needed for the realization of generic programmable PICs or photonic FPGAs to deploy sensors and actuators on a large scale and with low cost.<sup>[354,355]</sup> Compared with the well-developed NIR, the system-level development in the attractive MIR wavelength range significantly lags behind. Although various 2D materials have shown great potential for MIR waveguide-integrated photodetectors, wafer-scale synthesis and waveguide integration remain challenges for 2D materials.<sup>[356–358]</sup> Moreover, the MIR waveguide integration of other active components such as light sources and modulators is relatively stagnant as compared with photodetectors, hindering the realization of fully integrated MIR photonic nanosystems.<sup>[22,359,360]</sup> Although the synergy between photonic nanosystems and wearable electronics has brought a new dimension to the research field of wearable photonics, the reported works as reviewed in [section 4.3](#) still use discrete rigid photonic chips, optoelectronic components, and wearable electronic devices. Their integration into a wearable stand-alone working system remains an essential step toward practical applications. When integrated into the wearable system, the comfortability and stability under strain/stress need to be considered for photonic and optoelectronic components, for which the emerging flexible/stretchable photonics and optoelectronics could be useful.<sup>[25,361,362]</sup>

The other is synergy between optical sensing/actuation technologies and other advanced technologies for higher performances and more functionalities toward widespread applications. As reviewed in [sections 2.2](#) and [3.2.2](#), AI techniques, as emerging and appealing methodologies for data analysis, have been recently utilized to improve the intelligence of photodetectors for multi-property detection and chemical sensors for mixture sensing. More advanced AI techniques and models can be utilized and applied to add intelligence to more applications including but not

limited to physical sensing, communication, and imaging. Besides, as discussed in sections 4.2 and 4.3, high-performance implementations of neural networks have been realized by PICs. Therefore, the combination and even on-chip integration of nanophotonic sensors and neural networks are envisioned for edge computation in sensor networks. Furthermore, AI techniques can also be employed for the inverse design of nanophotonic devices. After being trained with random initial populations of nanostructure geometries and their known spectra, the deep neural networks are able to predict the spectral response of new nanostructure designs, as well as design new nanostructures based on the wanted spectral response.<sup>[224,363]</sup> In addition to AI techniques, the synergy between optical sensing/actuation technologies and various state-of-the-art technologies can be explored, such as NOEMS,<sup>[364]</sup> quantum photonics,<sup>[365]</sup> topological photonics,<sup>[366]</sup> 3D printing,<sup>[367]</sup> just to name a few, to bring optical technologies and their applications to a brand new era.

## Funding

This work was supported by Ministry of Education (MOE) Singapore Academic Research Fund Tier 2 (MOE-T2EP50220-0014), Advanced Research and Technology Innovation Centre (ARTIC) (A-0005947-20-00), and Hong Kong Polytechnic University Grant (P0046236).

## References

- [1] Shafique, K.; Khawaja, B.A.; Sabir, F.; Qazi, S.; Mustaqim, M. Internet of things (IoT) for next-generation smart systems: A review of current challenges, future trends and prospects for emerging 5G-IoT scenarios. *IEEE Access* **2020**, *8*, 23022–23040. DOI: [10.1109/ACCESS.2020.2970118](https://doi.org/10.1109/ACCESS.2020.2970118).
- [2] Le, X.; Shi, Q.; Vachon, P.; Ng, E.J.; Lee, C. Piezoelectric MEMS—evolution from sensing technology to diversified applications in the 5g/internet of things (IoT) era. *J. Micromech. Microeng.* **2022**, *32*, 014005. DOI: [10.1088/1361-6439/ac3ab9](https://doi.org/10.1088/1361-6439/ac3ab9).
- [3] Lee, S.; Shi, Q.; Lee, C. From flexible electronics technology in the era of IoT and artificial intelligence toward future implanted body sensor networks. *APL Mater.* **2019**, *7*, 031302.
- [4] Zhu, J.; Liu, X.; Shi, Q.; He, T.; Sun, Z.; Guo, X.; Liu, W.; Sulaiman, O.; Bin, Dong, B.; Lee, C. Development trends and perspectives of future sensors and MEMS/NEMS. *Micromachines* **2019**, *11*, 7. DOI: [10.3390/mi11010007](https://doi.org/10.3390/mi11010007).
- [5] Xiao, Z.; Liu, W.; Xu, S.; Zhou, J.; Ren, Z.; Lee, C. Recent progress in silicon-based photonic integrated circuits and emerging applications. *Adv. Opt. Mater.* **2023**, *11*, 2301028. DOI: [10.1002/adom.202301028](https://doi.org/10.1002/adom.202301028).
- [6] Gubbi, J.; Buyya, R.; Marusic, S.; Palaniswami, M. Internet of things (IoT): A vision, architectural elements, and future directions. *Futur. Gener. Comput. Syst.* **2013**, *29*, 1645–1660. DOI: [10.1016/j.future.2013.01.010](https://doi.org/10.1016/j.future.2013.01.010).
- [7] Zhang, Z.; Wen, F.; Sun, Z.; Guo, X.; He, T.; Lee, C. Artificial intelligence-enabled sensing technologies in the 5G/internet of things era: From virtual reality/augmented reality to the digital twin. *Adv. Intell. Syst.* **2022**, *4*, 2100228.
- [8] Tsybeskov, L.; Lockwood, D.J.; Ichikawa, M. Silicon photonics: CMOS going optical. *Proc. IEEE* **2009**, *97*, 1161–1165. DOI: [10.1109/JPROC.2009.2021052](https://doi.org/10.1109/JPROC.2009.2021052).
- [9] Miller, D.A.B. Physical reasons for optical interconnection. *Int. J. Optoelectron.* **1997**, *11*, 155–168.
- [10] Nahmias, M.A.; De Lima, T.F.; Tait, A.N.; Peng, H.T.; Shastri, B.J.; Prucnal, P.R. Photonic multiply-accumulate operations for neural networks. *IEEE J. Select. Topics Quantum Electron.* **2020**, *26*, 1–18. DOI: [10.1109/JSTQE.2019.2941485](https://doi.org/10.1109/JSTQE.2019.2941485).
- [11] Patterson, P.R.; Hah, D.; Lee, M.M.C.; Tsai, J.C.; Wu, M.C. Recent advances in optical MEMS devices and systems. *Proc. SPIE* **2002**, *4788*, 1–8. DOI: [10.1117/12.453712](https://doi.org/10.1117/12.453712).
- [12] Hodgkinson, J.; Tatam, R.P. Optical gas sensing: A review. *Meas. Sci. Technol.* **2013**, *24*, 012004. DOI: [10.1088/0957-0233/24/1/012004](https://doi.org/10.1088/0957-0233/24/1/012004).
- [13] Yang, W.; Chen, J.; Zhang, Y.; Zhang, Y.; He, J.; Fang, X. Silicon-compatible photodetectors: Trends to monolithically integrate photosensors with chip technology. *Adv. Funct. Mater.* **2019**, *29*, 1808182.
- [14] Haroun, A.; Le, X.; Gao, S.; Dong, B.; He, T.; Zhang, Z.; Wen, F.; Xu, S.; Lee, C. Progress in micro/nano sensors and nanoenergy for future AIoT-based smart home applications. *Nano Ex.* **2021**, *2*, 022005. DOI: [10.1088/2632-959X/abf3d4](https://doi.org/10.1088/2632-959X/abf3d4).

- [15] Petersen, K.E. Micromechanical light modulator array fabricated on silicon. *Appl. Phys. Lett.* **1977**, *31*, 521–523. DOI: [10.1063/1.89761](https://doi.org/10.1063/1.89761).
- [16] Petersen, K.E. Silicon torsional scanning mirror. *IBM J. Res. Dev.* **1980**, *24*, 631–637. DOI: [10.1147/rd.245.0631](https://doi.org/10.1147/rd.245.0631).
- [17] Wu, M.C.; Solgaard, O.; Ford, J.E. Optical MEMS for lightwave communication. *J. Lightwave Technol.* **2006**, *24*, 4433–4454. DOI: [10.1109/JLT.2006.886405](https://doi.org/10.1109/JLT.2006.886405).
- [18] Zhou, G.; Lim, Z.H.; Qi, Y.; Chau, F.S.; Zhou, G. MEMS gratings and their applications. *Int. J. Optomechatronics* **2021**, *15*, 61–86. DOI: [10.1080/15599612.2021.1892248](https://doi.org/10.1080/15599612.2021.1892248).
- [19] Ma, Y.; Dong, B.; Lee, C. Progress of infrared guided-wave nanophotonic sensors and devices. *Nano Converg.* **2020**, *7*, 12.
- [20] Jalali, B.; Fathpour, S. Silicon photonics. *J. Lightwave Technol.* **2006**, *24*, 4600–4615. DOI: [10.1109/JLT.2006.885782](https://doi.org/10.1109/JLT.2006.885782).
- [21] Gunn, C. CMOS photonics for high-speed interconnects. *IEEE Micro* **2006**, *26*, 58–66. DOI: [10.1109/MM.2006.32](https://doi.org/10.1109/MM.2006.32).
- [22] Lin, H.; Luo, Z.; Gu, T.; Kimerling, L.C.; Wada, K.; Agarwal, A.; Hu, J. Mid-infrared integrated photonics on silicon: A perspective. *Nanophotonics* **2017**, *7*, 393–420. DOI: [10.1515/nanoph-2017-0085](https://doi.org/10.1515/nanoph-2017-0085).
- [23] Estevez, M.C.; Alvarez, M.; Lechuga, L.M. Integrated optical devices for lab-on-a-chip biosensing applications. *Laser. Photon. Rev.* **2012**, *6*, 463–487. DOI: [10.1002/lpor.201100025](https://doi.org/10.1002/lpor.201100025).
- [24] Du, H.; Chau, F.S.; Zhou, G. Mechanically-tunable photonic devices with on-chip integrated MEMS/NEMS actuators. *Micromachines* **2016**, *7*, 69. DOI: [10.3390/mi7040069](https://doi.org/10.3390/mi7040069).
- [25] Shi, Q.; Dong, B.; He, T.; Sun, Z.; Zhu, J.; Zhang, Z.; Lee, C. Progress in wearable electronics/photonics—moving toward the era of artificial intelligence and internet of things. *InfoMat* **2020**, *2*, 1131–1162. DOI: [10.1002/inf2.12122](https://doi.org/10.1002/inf2.12122).
- [26] Zhou, H.; Kropelnicki, P.; Lee, C. CMOS compatible midinfrared wavelength-selective thermopile for high temperature applications. *J. Microelectromech. Syst.* **2015**, *24*, 144–154. DOI: [10.1109/JMEMS.2014.2322675](https://doi.org/10.1109/JMEMS.2014.2322675).
- [27] Guo, Q.; Pospischil, A.; Bhuiyan, M.; Jiang, H.; Tian, H.; Farmer, D.; Deng, B.; Li, C.; Han, S.J.; Wang, H.; Xia, Q.; Ma, T.P.; Mueller, T.; Xia, F. Black phosphorus mid-infrared photodetectors with high gain. *Nano Lett.* **2016**, *16*, 4648–4655. DOI: [10.1021/acs.nanolett.6b01977](https://doi.org/10.1021/acs.nanolett.6b01977).
- [28] Koh, K.H.; Lee, C. A two-dimensional MEMS scanning mirror using hybrid actuation mechanisms with low operation voltage. *J. Microelectromech. Syst.* **2012**, *21*, 1124–1135. DOI: [10.1109/JMEMS.2012.2196497](https://doi.org/10.1109/JMEMS.2012.2196497).
- [29] Han, S.; Seok, T.J.; Quack, N.; Yoo, B.-W.; Wu, M.C. Large-scale silicon photonic switches with movable directional couplers. *Optica* **2015**, *2*, 370–375. DOI: [10.1364/OPTICA.2.000370](https://doi.org/10.1364/OPTICA.2.000370).
- [30] Ríos, C.; Youngblood, N.; Cheng, Z.; Le Gallo, M.; Pernice, W.H.P.; Wright, C.D.; Sebastian, A.; Bhaskaran, H. In-memory computing on a photonic platform. *Sci. Adv.* **2019**, *5*, eaau5759. DOI: [10.1126/sciadv.aau5759](https://doi.org/10.1126/sciadv.aau5759).
- [31] Dong, B.; Zhang, Z.; Shi, Q.; Wei, J.; Ma, Y.; Xiao, Z.; Lee, C. Biometrics-protected optical communication enabled by deep learning-enhanced triboelectric/photonic synergistic interface. *Sci. Adv.* **2022**, *8*, eabl9874. DOI: [10.1126/sciadv.abl9874](https://doi.org/10.1126/sciadv.abl9874).
- [32] Rogers, C.; Piggott, A.Y.; Thomson, D.J.; Wiser, R.F.; Opris, I.E.; Fortune, S.A.; Compston, A.J.; Gondarenko, A.; Meng, F.; Chen, X.; Reed, G.T.; Nicolaescu, R. A universal 3D imaging sensor on a silicon photonics platform. *Nature* **2021**, *590*, 256–261. DOI: [10.1038/s41586-021-03259-y](https://doi.org/10.1038/s41586-021-03259-y).
- [33] Huang, L.; Dong, B.; Guo, X.; Chang, Y.; Chen, N.; Huang, X.; Liao, W.; Zhu, C.; Wang, H.; Lee, C.; Ang, K.-W. Waveguide-integrated black phosphorus photodetector for mid-infrared applications. *ACS Nano* **2019**, *13*, 913–921. DOI: [10.1021/acs.nano.8b08758](https://doi.org/10.1021/acs.nano.8b08758).
- [34] Li, W.; Wang, Z.; Feng, C.; Li, Q.; Yu, H. High sensitivity all-optical acoustic pressure sensor based on resonant micro-opto-mechanical cantilever with integrated rib waveguide. *Sens. Actuat. A Phys.* **2019**, *285*, 300–307. DOI: [10.1016/j.sna.2018.11.035](https://doi.org/10.1016/j.sna.2018.11.035).
- [35] Takahashi, K.; Oyama, H.; Misawa, N.; Okumura, K.; Ishida, M.; Sawada, K. Surface stress sensor using MEMS-based Fabry-Perot interferometer for label-free biosensing. *Sens. Actuat. B Chem.* **2013**, *188*, 393–399. DOI: [10.1016/j.snb.2013.06.106](https://doi.org/10.1016/j.snb.2013.06.106).
- [36] Westerveld, W.J.; Mahmud-Ul-Hasan, M.; Shnaiderman, R.; Ntziachristos, V.; Rottenberg, X.; Severi, S.; Rochus, V. Sensitive, small, broadband and scalable optomechanical ultrasound sensor in silicon photonics. *Nat. Photonics* **2021**, *15*, 341–345. DOI: [10.1038/s41566-021-00776-0](https://doi.org/10.1038/s41566-021-00776-0).
- [37] Liu, W.; Ma, Y.; Liu, X.; Zhou, J.; Xu, C.; Dong, B.; Lee, C. Larger-than-unity external optical field confinement enabled by metamaterial-assisted comb waveguide for ultrasensitive long-wave infrared gas spectroscopy. *Nano Lett.* **2022**, *22*, 6112–6120. DOI: [10.1021/acs.nanolett.2c01198](https://doi.org/10.1021/acs.nanolett.2c01198).
- [38] Mahmoud, M.; Mahmoud, A.; Cai, L.; Khan, M.; Mukherjee, T.; Bain, J.; Piazza, G. Novel on chip rotation detection based on the acousto-optic effect in surface acoustic wave gyroscopes. *Opt. Express* **2018**, *26*, 25060–25075. DOI: [10.1364/OE.26.025060](https://doi.org/10.1364/OE.26.025060).



- [39] Ma, Y.; Chang, Y.; Dong, B.; Wei, J.; Liu, W.; Lee, C. Heterogeneously integrated graphene/silicon/halide waveguide photodetectors toward chip-scale zero-bias long-wave infrared spectroscopic sensing. *ACS Nano* **2021**, *15*, 10084–10094. DOI: [10.1021/acsnano.1c01859](https://doi.org/10.1021/acsnano.1c01859).
- [40] Chen, W.C.; Lee, C.; Wu, C.Y.; Fang, W. A new latched  $2 \times 2$  optical switch using bi-directional movable electrothermal H-beam actuators. *Sens. Actuat. A Phys.* **2005**, *123–124*, 563–569. DOI: [10.1016/j.sna.2005.04.033](https://doi.org/10.1016/j.sna.2005.04.033).
- [41] Rogalski, A. Infrared detectors: Status and trends. *Prog. Quantum Electron.* **2003**, *27*, 59–210. DOI: [10.1016/S0079-6727\(02\)00024-1](https://doi.org/10.1016/S0079-6727(02)00024-1).
- [42] Graf, A.; Arndt, M.; Sauer, M.; Gerlach, G. Review of micromachined thermopiles for infrared detection. *Meas. Sci. Technol.* **2007**, *18*, R59–R75. DOI: [10.1088/0957-0233/18/7/R01](https://doi.org/10.1088/0957-0233/18/7/R01).
- [43] Xie, J.; Lee, C.; Wang, M.F.; Tsai, J.M. Microstructures for characterization of seebeck coefficient of doped polysilicon films. *Microsyst. Technol.* **2011**, *17*, 77–83. DOI: [10.1007/s00542-010-1183-9](https://doi.org/10.1007/s00542-010-1183-9).
- [44] Wu, H.; Emadi, A.; Sarro, P.M.; de Graaf, G.; Wolffenbuttel, R.F. A surface micromachined thermopile detector array with an interference-based absorber. *J. Micromech. Microeng.* **2011**, *21*, 074009. DOI: [10.1088/0960-1317/21/7/074009](https://doi.org/10.1088/0960-1317/21/7/074009).
- [45] Kumar, R.T.R.; Karunagaran, B.; Mangalaraj, D.; Narayandass, S.K.; Manoravi, P.; Joseph, M.; Gopal, V. Study of a pulsed laser deposited vanadium oxide based microbolometer array. *Smart Mater. Struct.* **2003**, *12*, 188–192. DOI: [10.1088/0964-1726/12/2/305](https://doi.org/10.1088/0964-1726/12/2/305).
- [46] Schimert, T.; Hanson, C.; Brady, J.; Fagan, T.; Taylor, M.; McCardel, W.; Gooch, R.; Gohlke, M.; Syllaos, A.J. Advances in small-pixel, large-format  $\alpha$ -Si bolometer arrays. *Proc. SPIE* **2009**, *7298*, 72980T. DOI: [10.1117/12.818576](https://doi.org/10.1117/12.818576).
- [47] Yadav, P.V.K.; Yadav, I.; Ajitha, B.; Rajasekar, A.; Gupta, S.; Ashok Kumar Reddy, Y. Advancements of uncooled infrared microbolometer materials: A review. *Sens. Actuat. A Phys.* **2022**, *342*, 113611. DOI: [10.1016/j.sna.2022.113611](https://doi.org/10.1016/j.sna.2022.113611).
- [48] Kesim, Y.E.; Battal, E.; Tanrikulu, M.Y.; Okyay, A.K. An all-ZnO microbolometer for infrared imaging. *Infrared. Phys. Technol.* **2014**, *67*, 245–249. DOI: [10.1016/j.infrared.2014.07.023](https://doi.org/10.1016/j.infrared.2014.07.023).
- [49] Ryzhii, V.; Otsuji, T.; Ryzhii, M.; Ryabova, N.; Yurchenko, S.O.; Mitin, V.; Shur, M.S. Graphene terahertz uncooled bolometers. *J. Phys. D Appl. Phys.* **2013**, *46*, 065102. DOI: [10.1088/0022-3727/46/6/065102](https://doi.org/10.1088/0022-3727/46/6/065102).
- [50] Banerjee, A.; Satoh, H.; Elamran, D.; Sharma, Y.; Hiromoto, N.; Inokawa, H. Performance improvement of on-chip integrable terahertz microbolometer arrays using nanoscale meander titanium thermistor. *J. Appl. Phys.* **2019**, *125*, 214502.
- [51] Liu, D.; Lu, W.; Lei, S.; Chen, Z. Low-noise readout circuit for thermo-electrical cooler-less uncooled microbolometer infrared imager. *Electron. Lett* **2016**, *52*, 705–706. DOI: [10.1049/el.2015.3407](https://doi.org/10.1049/el.2015.3407).
- [52] Ambrosio, R.; Moreno, M.; Mireles, J.; Torres, A.; Kosarev, A.; Heredia, A. An overview of uncooled infrared sensors technology based on amorphous silicon and silicon germanium alloys. *Phys. Status Solidi (c)* **2010**, *7*, 1180–1183. DOI: [10.1002/pssc.200982781](https://doi.org/10.1002/pssc.200982781).
- [53] Judy, J.W. Microelectromechanical systems (MEMS): Fabrication, design and applications. *Smart Mater. Struct.* **2001**, *10*, 1115–1134. DOI: [10.1088/0964-1726/10/6/301](https://doi.org/10.1088/0964-1726/10/6/301).
- [54] Kimata, M. Uncooled infrared focal plane arrays. *IEEJ Trans. Electr. Eng.* **2018**, *13*, 4–12. DOI: [10.1002/tee.22563](https://doi.org/10.1002/tee.22563).
- [55] Yu, L.; Guo, Y.; Zhu, H.; Luo, M.; Han, P.; Ji, X. Low-cost microbolometer type infrared detectors. *Micromachines* **2020**, *11*, 800. DOI: [10.3390/mi11090800](https://doi.org/10.3390/mi11090800).
- [56] Chen, C.; Li, C.; Min, S.; Guo, Q.; Xia, Z.; Liu, D.; Ma, Z.; Xia, F. Ultrafast silicon nanomembrane microbolometer for long-wavelength infrared light detection. *Nano Lett.* **2021**, *21*, 8385–8392. DOI: [10.1021/acs.nanolett.1c02972](https://doi.org/10.1021/acs.nanolett.1c02972).
- [57] Vicarelli, L.; Tredicucci, A.; Pitanti, A. Micromechanical bolometers for subterahertz detection at room temperature. *ACS Photonics* **2022**, *9*, 360–367. DOI: [10.1021/acsp Photonics.1c01273](https://doi.org/10.1021/acsp Photonics.1c01273).
- [58] Zhang, X.; Li, H.; Wei, Z.; Qi, L. Metamaterial for polarization-incident angle independent broadband perfect absorption in the terahertz range. *Opt. Mater. Express* **2017**, *7*, 3294. DOI: [10.1364/OME.7.003294](https://doi.org/10.1364/OME.7.003294).
- [59] Song, Z.; Zhang, J. Achieving broadband absorption and polarization conversion with a vanadium dioxide metasurface in the same terahertz frequencies. *Opt. Express* **2020**, *28*, 12487–12497. DOI: [10.1364/OE.391066](https://doi.org/10.1364/OE.391066).
- [60] Sun, C.; Shi, Q.; Hasan, D.; Yazici, M.S.; Zhu, M.; Ma, Y.; Dong, B.; Liu, Y.; Lee, C. Self-powered multi-functional monitoring system using hybrid integrated triboelectric nanogenerators and piezoelectric micro-sensors. *Nano Energy* **2019**, *58*, 612–623. DOI: [10.1016/j.nanoen.2019.01.096](https://doi.org/10.1016/j.nanoen.2019.01.096).
- [61] Chen, X.; Liu, X.; Wang, T.; Le, X.; Ma, F.; Lee, C.; Xie, J. Piezoelectric micromachined ultrasonic transducers with low thermoelastic dissipation and high quality factor. *J. Micromech. Microeng.* **2018**, *28*, 057001. DOI: [10.1088/1361-6439/aab1bc](https://doi.org/10.1088/1361-6439/aab1bc).
- [62] Wang, T.; Kobayashi, T.; Lee, C. Highly sensitive piezoelectric micromachined ultrasonic transducer operated in air. *Micro Nano Lett.* **2016**, *11*, 558–562. DOI: [10.1049/mnl.2016.0207](https://doi.org/10.1049/mnl.2016.0207).

- [63] Hui, Y.; Rinaldi, M. Fast and high resolution thermal detector based on an aluminum nitride piezoelectric microelectromechanical resonator with an integrated suspended heat absorbing element. *Appl. Phys. Lett.* **2013**, *102*, 093501.
- [64] Ren, Z.; Chang, Y.; Ma, Y.; Shih, K.; Dong, B.; Lee, C. Leveraging of MEMS technologies for optical meta-materials applications. *Adv. Opt. Mater.* **2020**, *8*, 1900653. DOI: [10.1002/adom.201900653](https://doi.org/10.1002/adom.201900653).
- [65] Dong, B.; Ma, Y.; Ren, Z.; Lee, C. Recent progress in nanoplasmonics-based integrated optical micro/nano-systems. *J. Phys. D Appl. Phys.* **2020**, *53*, 213001. DOI: [10.1088/1361-6463/ab77db](https://doi.org/10.1088/1361-6463/ab77db).
- [66] Hui, Y.; Gomez-Diaz, J.S.; Qian, Z.; Alù, A.; Rinaldi, M. Plasmonic piezoelectric nanomechanical resonator for spectrally selective infrared sensing. *Nat. Commun.* **2016**, *7*, 11249. DOI: [10.1038/ncomms11249](https://doi.org/10.1038/ncomms11249).
- [67] Shi, Q.; Yang, Y.; Sun, Z.; Lee, C. Progress of advanced devices and internet of things systems as enabling technologies for smart homes and health care. *ACS Mater. Au* **2022**, *2*, 394–435. DOI: [10.1021/acsmaterialsau.2c00001](https://doi.org/10.1021/acsmaterialsau.2c00001).
- [68] Qian, Z.; Kang, S.; Rajaram, V.; Cassella, C.; McGruer, N.E.; Rinaldi, M. Zero-power infrared digitizers based on plasmonically enhanced micromechanical photoswitches. *Nat. Nanotechnol.* **2017**, *12*, 969–973. DOI: [10.1038/nnano.2017.147](https://doi.org/10.1038/nnano.2017.147).
- [69] Liu, J.; Xia, F.; Xiao, D.; García de Abajo, F.J.; Sun, D. Semimetals for high-performance photodetection. *Nat. Mater.* **2020**, *19*, 830–837. DOI: [10.1038/s41563-020-0715-7](https://doi.org/10.1038/s41563-020-0715-7).
- [70] Michel, J.; Liu, J.; Kimerling, L.C. High-performance Ge-on-Si photodetectors. *Nat. Photon.* **2010**, *4*, 527–534. DOI: [10.1038/nphoton.2010.157](https://doi.org/10.1038/nphoton.2010.157).
- [71] Liu, J.; Cannon, D.D.; Wada, K.; Ishikawa, Y.; Jongthammanurak, S.; Danielson, D.T.; Michel, J.; Kimerling, L.C. Tensile strained Ge p-i-n photodetectors on Si platform for C and L band telecommunications. *Appl. Phys. Lett.* **2005**, *87*, 011110.
- [72] Loh, T.H.; Nguyen, H.S.; Tung, C.H.; Trigg, A.D.; Lo, G.Q.; Balasubramanian, N.; Kwong, D.L.; Tripathy, S. Ultrathin low temperature SiGe buffer for the growth of high quality Ge epilayer on Si(100) by ultra-high vacuum chemical vapor deposition. *Appl. Phys. Lett.* **2007**, *90*, 092108.
- [73] Jutzi, M.; Berroth, M.; Wohl, G.; Oehme, M.; Kasper, E. Ge-on-Si vertical incidence photodiodes with 39-GHz bandwidth. *IEEE Photon. Technol. Lett.* **2005**, *17*, 1510–1512. DOI: [10.1109/LPT.2005.848546](https://doi.org/10.1109/LPT.2005.848546).
- [74] Rouvière, M.; Vivien, L.; Le Roux, X.; Mangeney, J.; Crozat, P.; Hoarau, C.; Cassan, E.; Pascal, D.; Laval, S.; Fédéli, J.-M.; Damlencourt, J.-F.; Hartmann, J.M.; Kolev, S. Ultrahigh speed germanium-on-silicon-on-insulator photodetectors for 1.31 and 1.55  $\mu\text{m}$  operation. *Appl. Phys. Lett.* **2005**, *87*, 231109.
- [75] Oehme, M.; Werner, J.; Kasper, E.; Jutzi, M.; Berroth, M. High bandwidth Ge p-i-n photodetector integrated on Si. *Appl. Phys. Lett.* **2006**, *89*, 071117.
- [76] Loh, T.H.; Nguyen, H.S.; Murthy, R.; Yu, M.B.; Loh, W.Y.; Lo, G.Q.; Balasubramanian, N.; Kwong, D.L.; Wang, J.; Lee, S.J. Selective epitaxial germanium on silicon-on-insulator high speed photodetectors using low-temperature ultrathin Si<sub>0.8</sub>Ge<sub>0.2</sub> buffer. *Appl. Phys. Lett.* **2007**, *91*, 2005–2008.
- [77] Kang, Y.; Liu, H.-D.; Morse, M.; Panizza, M.J.; Zadka, M.; Litski, S.; Sarid, G.; Pauchard, A.; Kuo, Y.-H.; Chen, H.-W.; Zaoui, W.S.; Bowers, J.E.; Beling, A.; McIntosh, D.C.; Zheng, X.; Campbell, J.C. Monolithic germanium/silicon avalanche photodiodes with 340 GHz gain-bandwidth product. *Nat. Photon.* **2009**, *3*, 59–63. DOI: [10.1038/nphoton.2008.247](https://doi.org/10.1038/nphoton.2008.247).
- [78] Vines, P.; Kuzmenko, K.; Kirdoda, J.; Dumas, D.C.S.; Mirza, M.M.; Millar, R.W.; Paul, D.J.; Buller, G.S. High performance planar germanium-on-silicon single-photon avalanche diode detectors. *Nat. Commun.* **2019**, *10*, 1086. DOI: [10.1038/s41467-019-08830-w](https://doi.org/10.1038/s41467-019-08830-w).
- [79] Li, X.; Peng, L.; Liu, Z.; Liu, X.; Zheng, J.; Zuo, Y.; Xue, C.; Cheng, B. High-power back-to-back dual-absorption germanium photodetector. *Opt. Lett.* **2020**, *45*, 1358–1361. DOI: [10.1364/OL.388011](https://doi.org/10.1364/OL.388011).
- [80] Tran, H.; Pham, T.; Margetis, J.; Zhou, Y.; Dou, W.; Grant, P.C.; Grant, J.M.; Al-Kabi, S.; Sun, G.; Soref, R.A.; Tolle, J.; Zhang, Y.H.; Du, W.; Li, B.; Mortazavi, M.; Yu, S.Q. Si-based GeSn photodetectors toward mid-infrared imaging applications. *ACS Photon.* **2019**, *6*, 2807–2815. DOI: [10.1021/acsp Photonics.9b00845](https://doi.org/10.1021/acsp Photonics.9b00845).
- [81] Wang, J.; Lee, S. Ge-photodetectors for Si-based optoelectronic integration. *Sensors* **2011**, *11*, 696–718. DOI: [10.3390/s110100696](https://doi.org/10.3390/s110100696).
- [82] Benedikovic, D.; Virot, L.; Aubin, G.; Hartmann, J.-M.; Amar, F.; Le Roux, X.; Alonso-Ramos, C.; Cassan, É.; Marris-Morini, D.; Fédéli, J.-M.; Boeuf, F.; Szelag, B.; Vivien, L. Silicon-germanium receivers for short-wave-infrared optoelectronics and communications. *Nanophotonics* **2021**, *10*, 1059–1079. DOI: [10.1515/nanoph-2020-0547](https://doi.org/10.1515/nanoph-2020-0547).
- [83] Moutanabbir, O.; Assali, S.; Gong, X.; O'Reilly, E.; Broderick, C.A.; Marzban, B.; Witzens, J.; Du, W.; Yu, S.-Q.; Chelnokov, A.; Buca, D.; Nam, D. Monolithic infrared silicon photonics: The rise of (Si)GeSn semiconductors. *Appl. Phys. Lett.* **2021**, *118*, 110502.
- [84] Rogalski, A.; Martyniuk, P.; Kopytko, M. InAs/GaSb type-II superlattice infrared detectors: Future prospect. *Appl. Phys. Rev.* **2017**, *4*, 031304.
- [85] Ren, A.; Yuan, L.; Xu, H.; Wu, J.; Wang, Z. Recent progress of III–V quantum dot infrared photodetectors on silicon. *J. Mater. Chem. C* **2019**, *7*, 14441–14453. DOI: [10.1039/C9TC05738B](https://doi.org/10.1039/C9TC05738B).

- [86] Wu, J.; Jiang, Q.; Chen, S.; Tang, M.; Mazur, Y.I.; Maidaniuk, Y.; Benamara, M.; Semtsiv, M.P.; Masselink, W.T.; Sablon, K.A.; Salamo, G.J.; Liu, H. Monolithically integrated InAs/GaAs quantum dot mid-infrared photodetectors on silicon substrates. *ACS Photon.* **2016**, *3*, 749–753. DOI: [10.1021/acsphotonics.6b00076](https://doi.org/10.1021/acsphotonics.6b00076).
- [87] Jia, B.W.; Tan, K.H.; Loke, W.K.; Wicaksono, S.; Lee, K.H.; Yoon, S.F. Monolithic integration of InSb photodetector on silicon for mid-infrared silicon photonics. *ACS Photon.* **2018**, *5*, 1512–1520. DOI: [10.1021/acsphotonics.7b01546](https://doi.org/10.1021/acsphotonics.7b01546).
- [88] Delli, E.; Letka, V.; Hodgson, P.D.; Repiso, E.; Hayton, J.P.; Craig, A.P.; Lu, Q.; Beanland, R.; Krier, A.; Marshall, A.R.J.; Carrington, P.J. Mid-infrared InAs/InAsSb superlattice nBn photodetector monolithically integrated onto silicon. *ACS Photon.* **2019**, *6*, 538–544. DOI: [10.1021/acsphotonics.8b01550](https://doi.org/10.1021/acsphotonics.8b01550).
- [89] Ren, Z.; Xu, J.; Le, X.; Lee, C. Heterogeneous wafer bonding technology and thin-film transfer technology-enabling platform for the next generation applications beyond 5G. *Micromachines* **2021**, *12*, 946. DOI: [10.3390/mi12080946](https://doi.org/10.3390/mi12080946).
- [90] Rogalski, A.; Antoszewski, J.; Faraone, L. Third-generation infrared photodetector arrays. *J. Appl. Phys.* **2009**, *105*, 091101.
- [91] Norton, P. HgCdTe infrared detectors. *Opto-Electron. Rev.* **2002**, *10*, 159–174.
- [92] Xia, F.; Wang, H.; Xiao, D.; Dubey, M.; Ramasubramaniam, A. Two-dimensional material nanophotonics. *Nat. Photon.* **2014**, *8*, 899–907. DOI: [10.1038/nphoton.2014.271](https://doi.org/10.1038/nphoton.2014.271).
- [93] Bullock, J.; Amani, M.; Cho, J.; Chen, Y.Z.; Ahn, G.H.; Adinolfi, V.; Shrestha, V.R.; Gao, Y.; Crozier, K.B.; Chueh, Y.L.; Javey, A. Polarization-resolved black phosphorus/molybdenum disulfide mid-wave infrared photodiodes with high detectivity at room temperature. *Nat. Photon* **2018**, *12*, 601–607. DOI: [10.1038/s41566-018-0239-8](https://doi.org/10.1038/s41566-018-0239-8).
- [94] Liu, H.; Meng, J.; Zhang, X.; Chen, Y.; Yin, Z.; Wang, D.; Wang, Y.; You, J.; Gao, M.; Jin, P. High-performance deep ultraviolet photodetectors based on few-layer hexagonal boron nitride. *Nanoscale* **2018**, *10*, 5559–5565. DOI: [10.1039/c7nr09438h](https://doi.org/10.1039/c7nr09438h).
- [95] Tan, B.; Yang, H.; Hu, Y.; Gao, F.; Wang, L.; Dai, M.; Zhang, S.; Shang, H.; Chen, H.; Hu, P. Synthesis of high-quality multilayer hexagonal boron nitride films on Au foils for ultrahigh rejection ratio solar-blind photodetection. *ACS Appl. Mater. Interfaces* **2020**, *12*, 28351–28359. DOI: [10.1021/acsami.0c00449](https://doi.org/10.1021/acsami.0c00449).
- [96] Choi, W.; Choudhary, N.; Han, G.H.; Park, J.; Akinwande, D.; Lee, Y.H. Recent development of two-dimensional transition metal dichalcogenides and their applications. *Mater. Today* **2017**, *20*, 116–130. DOI: [10.1016/j.mattod.2016.10.002](https://doi.org/10.1016/j.mattod.2016.10.002).
- [97] Wang, J.; Fang, H.; Wang, X.; Chen, X.; Lu, W.; Hu, W. Recent progress on localized field enhanced two-dimensional material photodetectors from ultraviolet-visible to infrared. *Small* **2017**, *13*, 1700894. DOI: [10.1002/sml.201700894](https://doi.org/10.1002/sml.201700894).
- [98] Long, M.; Gao, A.; Wang, P.; Xia, H.; Ott, C.; Pan, C.; Fu, Y.; Liu, E.; Chen, X.; Lu, W.; Nilges, T.; Xu, J.; Wang, X.; Hu, W.; Miao, F. Room temperature high-detectivity mid-infrared photodetectors based on black arsenic phosphorus. *Sci. Adv.* **2017**, *3*, e1700589. DOI: [10.1126/sciadv.1700589](https://doi.org/10.1126/sciadv.1700589).
- [99] Yuan, S.; Shen, C.; Deng, B.; Chen, X.; Guo, Q.; Ma, Y.; Abbas, A.; Liu, B.; Haiges, R.; Ott, C.; Nilges, T.; Watanabe, K.; Taniguchi, T.; Sinai, O.; Naveh, D.; Zhou, C.; Xia, F. Air-stable room-temperature mid-infrared photodetectors based on hBN/black arsenic phosphorus/hBN heterostructures. *Nano Lett.* **2018**, *18*, 3172–3179. DOI: [10.1021/acs.nanolett.8b00835](https://doi.org/10.1021/acs.nanolett.8b00835).
- [100] Chen, X.; Lu, X.; Deng, B.; Sinai, O.; Shao, Y.; Li, C.; Yuan, S.; Tran, V.; Watanabe, K.; Taniguchi, T.; Naveh, D.; Yang, L.; Xia, F. Widely tunable black phosphorus mid-infrared photodetector. *Nat. Commun.* **2017**, *8*, 1672. DOI: [10.1038/s41467-017-01978-3](https://doi.org/10.1038/s41467-017-01978-3).
- [101] Hsu, A.L.; Herring, P.K.; Gabor, N.M.; Ha, S.; Shin, Y.C.; Song, Y.; Chin, M.; Dubey, M.; Chandrakasan, A.P.; Kong, J.; Jarillo-Herrero, P.; Palacios, T. Graphene-based thermopile for thermal imaging applications. *Nano Lett.* **2015**, *15*, 7211–7216. DOI: [10.1021/acs.nanolett.5b01755](https://doi.org/10.1021/acs.nanolett.5b01755).
- [102] Cai, X.; Sushkov, A.B.; Suess, R.J.; Jadidi, M.M.; Jenkins, G.S.; Nyakiti, L.O.; Myers-Ward, R.L.; Li, S.; Yan, J.; Gaskill, D.K.; Murphy, T.E.; Drew, H.D.; Fuhrer, M.S. Sensitive room-temperature terahertz detection via the photothermoelectric effect in graphene. *Nat. Nanotechnol.* **2014**, *9*, 814–819. DOI: [10.1038/nnano.2014.182](https://doi.org/10.1038/nnano.2014.182).
- [103] Dai, M.; Wang, C.; Ye, M.; Zhu, S.; Han, S.; Sun, F.; Chen, W.; Jin, Y.; Chua, Y.; Wang, Q.J. High-performance, polarization-sensitive, long-wave infrared photodetection via photothermoelectric effect with asymmetric Van Der Waals contacts. *ACS Nano* **2022**, *16*, 295–305. DOI: [10.1021/acsnano.1c06286](https://doi.org/10.1021/acsnano.1c06286).
- [104] Dong, Z.; Yu, W.; Zhang, L.; Mu, H.; Xie, L.; Li, J.; Zhang, Y.; Huang, L.; He, X.; Wang, L.; Lin, S.; Zhang, K. Highly efficient, ultrabroad PdSe<sub>2</sub> phototransistors from visible to terahertz driven by muti-physical mechanism. *ACS Nano* **2021**, *15*, 20403–20413. DOI: [10.1021/acsnano.1c08756](https://doi.org/10.1021/acsnano.1c08756).
- [105] Sefidmooye Azar, N.; Bullock, J.; Shrestha, V.R.; Balendhran, S.; Yan, W.; Kim, H.; Javey, A.; Crozier, K.B. Long-wave infrared photodetectors based on 2D platinum diselenide atop optical cavity substrates. *ACS Nano* **2021**, *15*, 6573–6581. DOI: [10.1021/acsnano.0c09739](https://doi.org/10.1021/acsnano.0c09739).

- [106] Xu, H.; Guo, C.; Zhang, J.; Guo, W.; Kuo, C.; Lue, C.S.; Hu, W.; Wang, L.; Chen, G.; Politano, A.; Chen, X.; Lu, W. PtTe 2-based type-II dirac semimetal and its Van Der Waals heterostructure for sensitive room temperature terahertz photodetection. *Small* **2019**, *15*, e1903362. DOI: [10.1002/smll.201903362](https://doi.org/10.1002/smll.201903362).
- [107] Zeng, L.; Wu, D.; Jie, J.; Ren, X.; Hu, X.; Lau, S.P.; Chai, Y.; Tsang, Y.H. Van Der Waals epitaxial growth of mosaic-like 2D platinum ditelluride layers for room-temperature mid-infrared photodetection up to 10.6  $\mu\text{m}$ . *Adv. Mater.* **2020**, *32*, e2004412. DOI: [10.1002/adma.202004412](https://doi.org/10.1002/adma.202004412).
- [108] Lai, J.; Liu, X.; Ma, J.; Wang, Q.; Zhang, K.; Ren, X.; Liu, Y.; Gu, Q.; Zhuo, X.; Lu, W.; Wu, Y.; Li, Y.; Feng, J.; Zhou, S.; Chen, J.-H.; Sun, D. Anisotropic broadband photoresponse of layered type-II Weyl semimetal MoTe 2. *Adv. Mater.* **2018**, *30*, e1707152.
- [109] Yao, Y.; Shankar, R.; Rauter, P.; Song, Y.; Kong, J.; Loncar, M.; Capasso, F. High-responsivity mid-infrared graphene detectors with antenna-enhanced photocarrier generation and collection. *Nano Lett.* **2014**, *14*, 3749–3754. DOI: [10.1021/nl500602n](https://doi.org/10.1021/nl500602n).
- [110] Wei, J.; Li, Y.; Wang, L.; Liao, W.; Dong, B.; Xu, C.; Zhu, C.; Ang, K.; Qiu, C.; Lee, C. Zero-bias mid-infrared graphene photodetectors with bulk photoresponse and calibration-free polarization detection. *Nat. Commun.* **2020**, *11*, 6404. DOI: [10.1038/s41467-020-20115-1](https://doi.org/10.1038/s41467-020-20115-1).
- [111] Wei, J.; Xu, C.; Dong, B.; Qiu, C.-W.; Lee, C. Mid-infrared semimetal polarization detectors with configurable polarity transition. *Nat. Photon.* **2021**, *15*, 614–621. DOI: [10.1038/s41566-021-00819-6](https://doi.org/10.1038/s41566-021-00819-6).
- [112] Cao, Y.; Fatemi, V.; Fang, S.; Watanabe, K.; Taniguchi, T.; Kaxiras, E.; Jarillo-Herrero, P. Unconventional superconductivity in magic-angle graphene superlattices. *Nature* **2018**, *556*, 43–50. DOI: [10.1038/nature26160](https://doi.org/10.1038/nature26160).
- [113] Sharpe, A.L.; Fox, E.J.; Barnard, A.W.; Finney, J.; Watanabe, K.; Taniguchi, T.; Kastner, M.A.; Goldhaber-Gordon, D. Emergent ferromagnetism near three-quarters filling in twisted bilayer graphene. *Science* **2019**, *365*, 605–608. DOI: [10.1126/science.aaw3780](https://doi.org/10.1126/science.aaw3780).
- [114] Ma, C.; Wang, Q.; Mills, S.; Chen, X.; Deng, B.; Yuan, S.; Li, C.; Watanabe, K.; Taniguchi, T.; Du, X.; Zhang, F.; Xia, F. Moiré band topology in twisted bilayer graphene. *Nano Lett.* **2020**, *20*, 6076–6083. DOI: [10.1021/acs.nanolett.0c02131](https://doi.org/10.1021/acs.nanolett.0c02131).
- [115] Wu, F.; Lovorn, T.; Tutuc, E.; Martin, I.; MacDonald, A.H. Topological insulators in twisted transition metal dichalcogenide homobilayers. *Phys. Rev. Lett.* **2019**, *122*, 086402. DOI: [10.1103/PhysRevLett.122.086402](https://doi.org/10.1103/PhysRevLett.122.086402).
- [116] Ni, G.X.; Wang, H.; Jiang, B.-Y.; Chen, L.X.; Du, Y.; Sun, Z.Y.; Goldflam, M.D.; Frenzel, A.J.; Xie, X.M.; Fogler, M.M.; Basov, D.N. Soliton superlattices in twisted hexagonal boron nitride. *Nat. Commun.* **2019**, *10*, 4360. DOI: [10.1038/s41467-019-12327-x](https://doi.org/10.1038/s41467-019-12327-x).
- [117] Hu, G.; Ou, Q.; Si, G.; Wu, Y.; Wu, J.; Dai, Z.; Krasnok, A.; Mazon, Y.; Zhang, Q.; Bao, Q.; Qiu, C.W.; Alù, A. Topological polaritons and photonic magic angles in twisted  $\alpha$ -MoO<sub>3</sub> bilayers. *Nature* **2020**, *582*, 209–213. DOI: [10.1038/s41586-020-2359-9](https://doi.org/10.1038/s41586-020-2359-9).
- [118] Deng, B.; Ma, C.; Wang, Q.; Yuan, S.; Watanabe, K.; Taniguchi, T.; Zhang, F.; Xia, F. Strong mid-infrared photoresponse in small-twist-angle bilayer graphene. *Nat. Photon.* **2020**, *14*, 549–553. DOI: [10.1038/s41566-020-0644-7](https://doi.org/10.1038/s41566-020-0644-7).
- [119] Ma, C.; Yuan, S.; Cheung, P.; Watanabe, K.; Taniguchi, T.; Zhang, F.; Xia, F. Intelligent infrared sensing enabled by tunable Moiré quantum geometry. *Nature* **2022**, *604*, 266–272. DOI: [10.1038/s41586-022-04548-w](https://doi.org/10.1038/s41586-022-04548-w).
- [120] Vivien, L.; Rouvière, M.; Fédéli, J.-M.; Marris-Morini, D.; Damlencourt, J.F.; Mangeney, J.; Crozat, P.; El Melhaoui, L.; Cassan, E.; Le Roux, X.; Pascal, D.; Laval, S. High speed and high responsivity germanium photodetector integrated in a silicon-on-insulator microwaveguide. *Opt. Express* **2007**, *15*, 9843–9848. DOI: [10.1364/oe.15.009843](https://doi.org/10.1364/oe.15.009843).
- [121] Feng, D.; Liao, S.; Dong, P.; Feng, N.-N.; Liang, H.; Zheng, D.; Kung, C.-C.; Fong, J.; Shafiha, R.; Cunningham, J.; Krishnamoorthy, A.V.; Asghari M. High-speed Ge photodetector monolithically integrated with large cross-section silicon-on-insulator waveguide. *Appl. Phys. Lett.* **2009**, *95*, 261105.
- [122] Ahn, D.; Hong, C.; Liu, J.; Giziewicz, W.; Beals, M.; Kimerling, L.C.; Michel, J.; Chen, J.; Kärtner, F.X. High performance, waveguide integrated Ge photodetectors. *Opt. Express* **2007**, *15*, 3916–3921. DOI: [10.1364/oe.15.003916](https://doi.org/10.1364/oe.15.003916).
- [123] Yin, T.; Cohen, R.; Morse, M.M.; Sarid, G.; Chetrit, Y.; Rubin, D.; Paniccia, M.J. 31 GHz Ge n-i-p waveguide photodetectors on silicon-on-insulator substrate. *Opt. Express* **2007**, *15*, 13965–13971. DOI: [10.1364/oe.15.013965](https://doi.org/10.1364/oe.15.013965).
- [124] Assefa, S.; Xia, F.; Vlasov, Y.A. Reinventing germanium avalanche photodetector for nanophotonic on-chip optical interconnects. *Nature* **2010**, *464*, 80–84. DOI: [10.1038/nature08813](https://doi.org/10.1038/nature08813).
- [125] Huang, Y.-H.; Chang, G.-E.; Li, H.; Cheng, H.H. Sn-based waveguide p-i-n photodetector with strained GeSn/Ge multiple-quantum-well active layer. *Opt. Lett.* **2017**, *42*, 1652–1655. DOI: [10.1364/OL.42.001652](https://doi.org/10.1364/OL.42.001652).

- [126] Hattasan, N.; Gassenq, A.; Cerutti, L.; Rodriguez, J.-B.; Tournie, E.; Roelkens, G. Heterogeneous integration of GaInAsSb p-i-n photodiodes on a silicon-on-insulator waveguide circuit. *IEEE Photon. Technol. Lett.* **2011**, *23*, 1760–1762. DOI: [10.1109/LPT.2011.2169244](https://doi.org/10.1109/LPT.2011.2169244).
- [127] Ryckeboer, E.; Gassenq, A.; Muneeb, M.; Hattasan, N.; Pathak, S.; Cerutti, L.; Rodriguez, J.B.; Tournié, E.; Bogaerts, W.; Baets, R.; Roelkens, G. Silicon-on-insulator spectrometers with integrated GaInAsSb photodiodes for wide-band spectroscopy from 1510 to 2300 nm. *Opt. Express* **2013**, *21*, 6101–6108. DOI: [10.1364/OE.21.006101](https://doi.org/10.1364/OE.21.006101).
- [128] Muneeb, M.; Ruocco, A.; Malik, A.; Pathak, S.; Ryckeboer, E.; Sanchez, D.; Cerutti, L.; Rodriguez, J.B.; Tournié, E.; Bogaerts, W.; Smit, M.K.; Roelkens, G. Silicon-on-insulator shortwave infrared wavelength meter with integrated photodiodes for on-chip laser monitoring. *Opt. Express* **2014**, *22*, 27300–27308. DOI: [10.1364/OE.22.027300](https://doi.org/10.1364/OE.22.027300).
- [129] Wang, R.; Sprengel, S.; Muneeb, M.; Boehm, G.; Baets, R.; Amann, M.-C.; Roelkens, G. 2  $\mu$ m Wavelength range InP-based type-II quantum well photodiodes heterogeneously integrated on silicon photonic integrated circuits. *Opt. Express* **2015**, *23*, 26834–26841. DOI: [10.1364/OE.23.026834](https://doi.org/10.1364/OE.23.026834).
- [130] Roelkens, G.; Dave, U.; Gassenq, A.; Hattasan, N.; Chen Hu, Kuyken, B.; Leo, F.; Malik, A.; Muneeb, M.; Ryckeboer, E.; Sanchez, D.; Uvin, S.; Wang, R.; Hens, Z.; Baets, R.; Shimura, Y.; Gencarelli, F.; Vincent, B.; Loo, R.; Van Campenhout, J.; Cerutti, L.; Rodriguez, J.-B.; Tournie, E.; Xia, C.; Nedeljkovic, M.; Mashanovich, G.; Li, S.; Healy, N.; Peacock, A.C.; Xiaoping, L.; Osgood, R.; Green, W.M.J. Silicon-based photonic integration beyond the telecommunication wavelength range. *IEEE J. Sel. Top. Quantum Electron.* **2014**, *20*, 8201511.
- [131] Grote, R.R.; Souhan, B.; Ophir, N.; Driscoll, J.B.; Bergman, K.; Bahkru, H.; Green, W.M.J.; Osgood, R.M. Extrinsic photodiodes for integrated mid-infrared silicon photonics. *Optica* **2014**, *1*, 264–267. DOI: [10.1364/OPTICA.1.000264](https://doi.org/10.1364/OPTICA.1.000264).
- [132] Souhan, B.; Grote, R.R.; Chen, C.P.; Huang, H.-C.; Driscoll, J.B.; Lu, M.; Stein, A.; Bakhru, H.; Bergman, K.; Green, W.M.J.; Osgood, R.M. Si+-implanted Si-wire waveguide photodetectors for the mid-infrared. *Opt. Express* **2014**, *22*, 27415–27424. DOI: [10.1364/OE.22.027415](https://doi.org/10.1364/OE.22.027415).
- [133] Ackert, J.J.; Thomson, D.J.; Shen, L.; Peacock, A.C.; Jessop, P.E.; Reed, G.T.; Mashanovich, G.Z.; Knights, A.P. High-speed detection at two micrometres with monolithic silicon photodiodes. *Nat. Photon.* **2015**, *9*, 393–396. DOI: [10.1038/nphoton.2015.81](https://doi.org/10.1038/nphoton.2015.81).
- [134] Gan, X.; Shiue, R.J.; Gao, Y.; Meric, I.; Heinz, T.F.; Shepard, K.; Hone, J.; Assefa, S.; Englund, D. Chip-integrated ultrafast graphene photodetector with high responsivity. *Nat. Photon.* **2013**, *7*, 883–887. DOI: [10.1038/nphoton.2013.253](https://doi.org/10.1038/nphoton.2013.253).
- [135] Pospischil, A.; Humer, M.; Furchi, M.M.; Bachmann, D.; Guider, R.; Fromherz, T.; Mueller, T. CMOS-compatible graphene photodetector covering all optical communication bands. *Nat. Photon.* **2013**, *7*, 892–896. DOI: [10.1038/nphoton.2013.240](https://doi.org/10.1038/nphoton.2013.240).
- [136] Wang, X.; Cheng, Z.; Xu, K.; Tsang, H.K.; Xu, J.-B. High-responsivity graphene/silicon-heterostructure waveguide photodetectors. *Nat. Photon.* **2013**, *7*, 888–891. DOI: [10.1038/nphoton.2013.241](https://doi.org/10.1038/nphoton.2013.241).
- [137] Schuler, S.; Schall, D.; Neumaier, D.; Dobusch, L.; Bethge, O.; Schwarz, B.; Krall, M.; Mueller, T. Controlled generation of a p-n junction in a waveguide integrated graphene photodetector. *Nano Lett.* **2016**, *16*, 7107–7112. DOI: [10.1021/acs.nanolett.6b03374](https://doi.org/10.1021/acs.nanolett.6b03374).
- [138] Muench, J.E.; Ruocco, A.; Giambra, M.A.; Miseikis, V.; Zhang, D.; Wang, J.; Watson, H.F.Y.; Park, G.C.; Akhavan, S.; Soriano, V.; Midrio, M.; Tomadin, A.; Coletti, C.; Romagnoli, M.; Ferrari, A.C.; Goykhman, I. Waveguide-integrated, plasmonic enhanced graphene photodetectors. *Nano Lett.* **2019**, *19*, 7632–7644. DOI: [10.1021/acs.nanolett.9b02238](https://doi.org/10.1021/acs.nanolett.9b02238).
- [139] Guo, J.; Li, J.; Liu, C.; Yin, Y.; Wang, W.; Ni, Z.; Fu, Z.; Yu, H.; Xu, Y.; Shi, Y.; Ma, Y.; Gao, S.; Tong, L.; Dai, D. High-performance silicon – graphene hybrid plasmonic waveguide photodetectors beyond 1.55  $\mu$ m. *Light Sci. Appl.* **2020**, *9*, 29.
- [140] Schuler, S.; Muench, J.E.; Ruocco, A.; Balci, O.; Thourhout, D.V.; Soriano, V.; Romagnoli, M.; Watanabe, K.; Taniguchi, T.; Goykhman, I.; Ferrari, A.C.; Mueller, T. High-responsivity graphene photodetectors integrated on silicon microring resonators. *Nat. Commun.* **2021**, *12*, 3733. DOI: [10.1038/s41467-021-23436-x](https://doi.org/10.1038/s41467-021-23436-x).
- [141] Bie, Y.Q.; Grosso, G.; Heuck, M.; Furchi, M.M.; Cao, Y.; Zheng, J.; Bunandar, D.; Navarro-Moratalla, E.; Zhou, L.; Efetov, D.K.; Taniguchi, T.; Watanabe, K.; Kong, J.; Englund, D.; Jarillo-Herrero, P. A MoTe2-based light-emitting diode and photodetector for silicon photonic integrated circuits. *Nat. Nanotechnol.* **2017**, *12*, 1124–1129. DOI: [10.1038/nnano.2017.209](https://doi.org/10.1038/nnano.2017.209).
- [142] Maiti, R.; Patil, C.; Saadi, M.A.S.R.; Xie, T.; Azadani, J.G.; Uluutku, B.; Amin, R.; Briggs, A.F.; Miscuglio, M.; Van Thourhout, D.; Solares, S.D.; Low, T.; Agarwal, R.; Bank, S.R.; Sorger, V.J. Strain-engineered high-responsivity MoTe2 photodetector for silicon photonic integrated circuits. *Nat. Photon.* **2020**, *14*, 578–584. DOI: [10.1038/s41566-020-0647-4](https://doi.org/10.1038/s41566-020-0647-4).



- [143] Parhizkar, S.; Precht, M.; Giesecke, A.L.; Suckow, S.; Wahl, S.; Lukas, S.; Hartwig, O.; Negm, N.; Quellmalz, A.; Gylfason, K.; Schall, D.; Wuttig, M.; Duesberg, G.S.; Lemme, M.C. Two-dimensional platinum diselenide waveguide-integrated infrared photodetectors. *ACS Photon.* **2022**, *9*, 859–867. DOI: [10.1021/acsp Photonics.1c01517](https://doi.org/10.1021/acsp Photonics.1c01517).
- [144] Youngblood, N.; Chen, C.; Koester, S.J.; Li, M. Waveguide-integrated black phosphorus photodetector with high responsivity and low dark current. *Nat. Photon.* **2015**, *9*, 247–252. DOI: [10.1038/nphoton.2015.23](https://doi.org/10.1038/nphoton.2015.23).
- [145] Chen, C.; Youngblood, N.; Peng, R.; Yoo, D.; Mohr, D.A.; Johnson, T.W.; Oh, S.H.; Li, M. Three-dimensional integration of black phosphorus photodetector with silicon photonics and nanoplasmonics. *Nano Lett.* **2017**, *17*, 985–991. DOI: [10.1021/acs.nanolett.6b04332](https://doi.org/10.1021/acs.nanolett.6b04332).
- [146] Yin, Y.; Cao, R.; Guo, J.; Liu, C.; Li, J.; Feng, X.; Wang, H.; Du, W.; Qadir, A.; Zhang, H.; Ma, Y.; Gao, S.; Xu, Y.; Shi, Y.; Tong, L.; Dai, D. High-speed and high-responsivity hybrid silicon/black-phosphorus waveguide photodetectors at 2  $\mu\text{m}$ . *Laser Photon. Rev.* **2019**, *13*, 1900032.
- [147] Flöry, N.; Ma, P.; Salamin, Y.; Emboras, A.; Taniguchi, T.; Watanabe, K.; Leuthold, J.; Novotny, L. Waveguide-integrated Van Der Waals heterostructure photodetector at telecom wavelengths with high speed and high responsivity. *Nat. Nanotechnol.* **2020**, *15*, 118–124. DOI: [10.1038/s41565-019-0602-z](https://doi.org/10.1038/s41565-019-0602-z).
- [148] Tian, R.; Gan, X.; Li, C.; Chen, X.; Hu, S.; Gu, L.; Van Thourhout, D.; Castellanos-Gomez, A.; Sun, Z.; Zhao, J. Chip-integrated Van Der Waals PN heterojunction photodetector with low dark current and high responsivity. *Light Sci. Appl.* **2022**, *11*, 101.
- [149] Xia, Z.; Song, H.; Kim, M.; Zhou, M.; Chang, T.-H.; Liu, D.; Yin, X.; Xiong, K.; Mi, H.; Wang, X.; Xia, F.; Yu, Z.; Ma, Z. (Jack); Gan, Q. Single-crystalline germanium nanomembrane photodetectors on foreign nanocavities. *Sci. Adv.* **2017**, *3*, e1602783. DOI: [10.1126/sciadv.1602783](https://doi.org/10.1126/sciadv.1602783).
- [150] Ma, Y.; Dong, B.; Wei, J.; Chang, Y.; Huang, L.; Ang, K.; Lee, C. High-responsivity mid-infrared black phosphorus slow light waveguide photodetector. *Adv. Opt. Mater.* **2020**, *8*, 2000337. DOI: [10.1002/adom.202000337](https://doi.org/10.1002/adom.202000337).
- [151] Ma, Y.; Dong, B.; Li, B.; Wei, J.; Chang, Y.; Ho, C.P.; Lee, C. Mid-infrared slow light engineering and tuning in 1-D grating waveguide. *IEEE J. Select. Topics Quantum Electron.* **2018**, *24*, 1–8. DOI: [10.1109/JSTQE.2018.2827659](https://doi.org/10.1109/JSTQE.2018.2827659).
- [152] Ma, Y.; Dong, B.; Li, B.; Ang, K.-W.; Lee, C. Dispersion engineering and thermo-optic tuning in mid-infrared photonic crystal slow light waveguides on silicon-on-insulator. *Opt. Lett.* **2018**, *43*, 5504–5507. DOI: [10.1364/OL.43.005504](https://doi.org/10.1364/OL.43.005504).
- [153] Tian, R.; Gu, L.; Ji, Y.; Li, C.; Chen, Y.; Hu, S.; Li, Z.; Gan, X.; Zhao, J. Black phosphorus photodetector enhanced by a planar photonic crystal cavity. *ACS Photon.* **2021**, *8*, 3104–3110. DOI: [10.1021/acsp Photonics.1c01168](https://doi.org/10.1021/acsp Photonics.1c01168).
- [154] Ma, P.; Salamin, Y.; Baeuerle, B.; Josten, A.; Heni, W.; Emboras, A.; Leuthold, J. Plasmonically enhanced graphene photodetector featuring 100 gbit/s data reception, high responsivity, and compact size. *ACS Photon.* **2019**, *6*, 154–161. DOI: [10.1021/acsp Photonics.8b01234](https://doi.org/10.1021/acsp Photonics.8b01234).
- [155] Liu, C.; Guo, J.; Yu, L.; Xiang, Y.; Xiang, H.; Li, J.; Dai, D. High-speed and high-responsivity silicon/black-phosphorus hybrid plasmonic waveguide avalanche photodetector. *ACS Photon.* **2022**, *9*, 1764–1774. DOI: [10.1021/acsp Photonics.2c00244](https://doi.org/10.1021/acsp Photonics.2c00244).
- [156] Ding, Y.; Cheng, Z.; Zhu, X.; Yvind, K.; Dong, J.; Galili, M.; Hu, H.; Mortensen, N.A.; Xiao, S.; Oxenløwe, L.K. Ultra-compact integrated graphene plasmonic photodetector with bandwidth above 110 GHz. *Nanophotonics* **2020**, *9*, 317–325. DOI: [10.1515/nanoph-2019-0167](https://doi.org/10.1515/nanoph-2019-0167).
- [157] Ma, Z.; Kikunaga, K.; Wang, H.; Sun, S.; Amin, R.; Maiti, R.; Tahersima, M.H.; Dalir, H.; Miscuglio, M.; Sorger, V.J. Compact graphene plasmonic slot photodetector on silicon-on-insulator with high responsivity. *ACS Photon.* **2020**, *7*, 932–940. DOI: [10.1021/acsp Photonics.9b01452](https://doi.org/10.1021/acsp Photonics.9b01452).
- [158] Liu, X.; Liu, W.; Ren, Z.; Ma, Y.; Dong, B.; Zhou, G.; Lee, C. Progress of optomechanical micro/nano sensors : A review. *Int. J. Optomechatronics* **2021**, *15*, 120–159. DOI: [10.1080/15599612.2021.1986612](https://doi.org/10.1080/15599612.2021.1986612).
- [159] Qiao, Q.; Xia, J.; Lee, C.; Zhou, G. Applications of photonic crystal nanobeam cavities for sensing. *Micromachines* **2018**, *9*, 541. DOI: [10.3390/mi9110541](https://doi.org/10.3390/mi9110541).
- [160] Kim, D.; Hall, N.A. Towards a sub 15-dBA optical micromachined microphone. *J. Acoust. Soc. Am.* **2014**, *135*, 2664–2673. DOI: [10.1121/1.4871181](https://doi.org/10.1121/1.4871181).
- [161] Hall, N.A.; Okandan, M.; Littrell, R.; Serkland, D.K.; Keeler, G.A.; Peterson, K.; Bicen, B.; Garcia, C.T.; Degertekin, F.L. Micromachined accelerometers with optical interferometric read-out and integrated electrostatic actuation. *J. Microelectromech. Syst.* **2008**, *17*, 37–44. DOI: [10.1109/JMEMS.2007.910243](https://doi.org/10.1109/JMEMS.2007.910243).
- [162] Bicen, B.; Jolly, S.; Jeelani, K.; Garcia, C.T.; Hall, N.A.; Degertekin, F.L.; Su, Q.; Cui, W.; Miles, R.N. Integrated optical displacement detection and electrostatic actuation for directional optical microphones with micromachined biomimetic diaphragms. *IEEE Sensors J.* **2009**, *9*, 1933–1941. DOI: [10.1109/JSEN.2009.2031810](https://doi.org/10.1109/JSEN.2009.2031810).

- [163] Zinoviev, K.; Dominguez, C.; Plaza, J.A.; Busto, V.J.C.; Lechuga, L.M. A novel optical waveguide micro-cantilever sensor for the detection of nanomechanical forces. *J. Lightwave Technol.* **2006**, *24*, 2132–2138. DOI: [10.1109/JLT.2006.872315](https://doi.org/10.1109/JLT.2006.872315).
- [164] Ollier, E.; Philippe, P.; Chabrol, C.; Mottier, P. Micro-opto-mechanical vibration sensor integrated on silicon. *J. Lightwave Technol.* **1999**, *17*, 26–29. DOI: [10.1109/50.737417](https://doi.org/10.1109/50.737417).
- [165] Yao, M.; Zhang, Y.; Ouyang, X.; Ping Zhang, A.; Tam, H.-Y.; Wai, P.K.A. Ultracompact optical fiber acoustic sensors based on a fiber-top spirally-suspended optomechanical microresonator. *Opt. Lett.* **2020**, *45*, 3516–3519. DOI: [10.1364/OL.393900](https://doi.org/10.1364/OL.393900).
- [166] Chen, M. q.; Zhao, Y.; Wei, H. m.; Zhu, C. l.; Krishnaswamy, S. 3D printed castle style Fabry-Perot micro-cavity on optical fiber tip as a highly sensitive humidity sensor. *Sens. Actuat. B Chem.* **2021**, *328*, 128981. DOI: [10.1016/j.snb.2020.128981](https://doi.org/10.1016/j.snb.2020.128981).
- [167] Wu, G.; Datar, R.H.; Hansen, K.M.; Thundat, T.; Cote, R.J.; Majumdar, A. Bioassay of prostate-specific antigen (PSA) using microcantilevers. *Nat. Biotechnol.* **2001**, *19*, 856–860. DOI: [10.1038/nbt0901-856](https://doi.org/10.1038/nbt0901-856).
- [168] Fritz, J.; Baller, M.K.; Lang, H.P.; Rothuizen, H.; Vettiger, P.; Meyer, E.; Güntherodt, H.J.; Gerber, C.; Gimzewski, J.K. Translating biomolecular recognition into nanomechanics. *Science* **2000**, *288*, 316–318. DOI: [10.1126/science.288.5464.316](https://doi.org/10.1126/science.288.5464.316).
- [169] McKendry, R.; Zhang, J.; Arntz, Y.; Strunz, T.; Hegner, M.; Lang, H.P.; Baller, M.K.; Certa, U.; Meyer, E.; Güntherodt, H.J.; Gerber, C. Multiple label-free biodetection and quantitative DNA-binding assays on a nanomechanical cantilever array. *Proc. Natl. Acad. Sci. U. S. A.* **2002**, *99*, 9783–9788. DOI: [10.1073/pnas.152330199](https://doi.org/10.1073/pnas.152330199).
- [170] Zhang, J.; Lang, H.P.; Huber, F.; Bietsch, A.; Grange, W.; Certa, U.; Mckendry, R.; Güntherodt, H.-J.; Hegner, M.; Gerber, C. Rapid and label-free nanomechanical detection of biomarker transcripts in human RNA. *Nat. Nanotechnol.* **2006**, *1*, 214–220. DOI: [10.1038/nnano.2006.134](https://doi.org/10.1038/nnano.2006.134).
- [171] Luo, J.; Liu, S.; Chen, P.; Lu, S.; Zhang, Q.; Chen, Y.; Du, B.; Tang, J.; He, J.; Liao, C.; Wang, Y. Fiber optic hydrogen sensor based on a Fabry-Perot interferometer with a fiber Bragg grating and a nanofilm. *Lab Chip* **2021**, *21*, 1752–1758. DOI: [10.1039/d1lc00012h](https://doi.org/10.1039/d1lc00012h).
- [172] Aspelmeyer, M.; Kippenberg, T.J.; Marquardt, F. Cavity optomechanics. *Rev. Mod. Phys.* **2014**, *86*, 1391–1452. DOI: [10.1103/RevModPhys.86.1391](https://doi.org/10.1103/RevModPhys.86.1391).
- [173] Krause, A.G.; Winger, M.; Blasius, T.D.; Lin, Q.; Painter, O. A high-resolution microchip optomechanical accelerometer. *Nat. Photon.* **2012**, *6*, 768–772. DOI: [10.1038/nphoton.2012.245](https://doi.org/10.1038/nphoton.2012.245).
- [174] Zhou, F.; Bao, Y.; Madugani, R.; Long, D.A.; Gorman, J.J.; LeBrun, T.W. Broadband thermomechanically limited sensing with an optomechanical accelerometer. *Optica* **2021**, *8*, 350–356. DOI: [10.1364/OPTICA.413117](https://doi.org/10.1364/OPTICA.413117).
- [175] Davuluri, S.; Li, K.; Li, Y. Gyroscope with two-dimensional optomechanical mirror. *New. J. Phys.* **2017**, *19*, 113004. DOI: [10.1088/1367-2630/aa8afb](https://doi.org/10.1088/1367-2630/aa8afb).
- [176] He, L.; Li, H.; Li, M. Optomechanical measurement of photon spin angular momentum and optical torque in integrated photonic devices. *Sci. Adv.* **2016**, *2*, e1600485. DOI: [10.1126/sciadv.1600485](https://doi.org/10.1126/sciadv.1600485).
- [177] Fogliano, F.; Besga, B.; Reigue, A.; Heringlake, P.; Mercier de Lépinay, L.; Vaneph, C.; Reichel, J.; Pigeau, B.; Arcizet, O. Mapping the cavity optomechanical interaction with subwavelength-sized ultrasensitive nanomechanical force sensors. *Phys. Rev. X* **2021**, *11*, 021009. DOI: [10.1103/PhysRevX.11.021009](https://doi.org/10.1103/PhysRevX.11.021009).
- [178] Fogliano, F.; Besga, B.; Reigue, A.; Mercier de Lépinay, L.; Heringlake, P.; Gouriou, C.; Eyraud, E.; Wernsdorfer, W.; Pigeau, B.; Arcizet, O. Ultrasensitive nano-optomechanical force sensor operated at dilution temperatures. *Nat. Commun.* **2021**, *12*, 4124. DOI: [10.1038/s41467-021-24318-y](https://doi.org/10.1038/s41467-021-24318-y).
- [179] Paraíso, T.K.; Kalaei, M.; Zang, L.; Pfeifer, H.; Marquardt, F.; Painter, O. Position-squared coupling in a tunable photonic crystal optomechanical cavity. *Phys. Rev. X* **2015**, *5*, 041024. DOI: [10.1103/PhysRevX.5.041024](https://doi.org/10.1103/PhysRevX.5.041024).
- [180] Xia, J.; Qiao, Q.; Sun, H.; Huang, Y.; Chau, F.S.; Zhou, G. Ultrasensitive nanoscale optomechanical electrometer using photonic crystal cavities. *Nanophotonics* **2022**, *11*, 1629–1642. DOI: [10.1515/nanoph-2021-0820](https://doi.org/10.1515/nanoph-2021-0820).
- [181] Liu, T.; Pagliano, F.; van Veldhoven, R.; Pogoretskiy, V.; Jiao, Y.; Fiore, A. Integrated nano-optomechanical displacement sensor with ultrawide optical bandwidth. *Nat. Commun.* **2020**, *11*, 4679. DOI: [10.1038/s41467-020-18579-2](https://doi.org/10.1038/s41467-020-18579-2).
- [182] Basiri-Esfahani, S.; Armin, A.; Forstner, S.; Bowen, W.P. Precision ultrasound sensing on a chip. *Nat. Commun.* **2019**, *10*, 132. DOI: [10.1038/s41467-018-08038-4](https://doi.org/10.1038/s41467-018-08038-4).
- [183] Shi, Q.; Wang, T.; Lee, C. MEMS based broadband piezoelectric ultrasonic energy harvester (PUEH) for enabling self-powered implantable biomedical devices. *Sci. Rep.* **2016**, *6*, 24946. DOI: [10.1038/srep24946](https://doi.org/10.1038/srep24946).
- [184] Wissmeyer, G.; Pleitez, M.A.; Rosenthal, A.; Ntziachristos, V. Looking at sound: Optoacoustics with all-optical ultrasound detection. *Light Sci. Appl.* **2018**, *7*, 53.
- [185] Tombez, L.; Zhang, E.J.; Orcutt, J.S.; Kamlapurkar, S.; Green, W.M.J. Methane absorption spectroscopy on a silicon photonic chip. *Optica* **2017**, *4*, 1322–1325. DOI: [10.1364/OPTICA.4.001322](https://doi.org/10.1364/OPTICA.4.001322).

- [186] Fard, S.T.; Donzella, V.; Schmidt, S.A.; Flueckiger, J.; Grist, S.M.; Talebi Fard, P.; Wu, Y.; Bojko, R.J.; Kwok, E.; Jaeger, N.A.F.; Ratner, D.M.; Chrostowski, L. Performance of ultra-thin SOI-based resonators for sensing applications. *Opt. Express* **2014**, *22*, 14166–14179. DOI: [10.1364/OE.22.014166](https://doi.org/10.1364/OE.22.014166).
- [187] Gaur, G.; Hu, S.; Mernaugh, R.L.; Kravchenko, I.I.; Retterer, S.T.; Weiss, S.M. Label-free detection of Herceptin® using suspended silicon microring resonators. *Sens. Actuat. B Chem.* **2018**, *275*, 394–401. DOI: [10.1016/j.snb.2018.07.081](https://doi.org/10.1016/j.snb.2018.07.081).
- [188] Liu, Q.; Tu, X.; Kim, K.W.; Kee, J.S.; Shin, Y.; Han, K.; Yoon, Y.-J.; Lo, G.-Q.; Park, M.K. Highly sensitive Mach–Zehnder interferometer biosensor based on silicon nitride slot waveguide. *Sens. Actuat. B Chem.* **2013**, *188*, 681–688. DOI: [10.1016/j.snb.2013.07.053](https://doi.org/10.1016/j.snb.2013.07.053).
- [189] Flueckiger, J.; Schmidt, S.; Donzella, V.; Sherwali, A.; Ratner, D.M.; Chrostowski, L.; Cheung, K.C. Sub-wavelength grating for enhanced ring resonator biosensor. *Opt. Express* **2016**, *24*, 15672–15686. DOI: [10.1364/OE.24.015672](https://doi.org/10.1364/OE.24.015672).
- [190] Lai, W.-C.; Chakravarty, S.; Zou, Y.; Chen, R.T. Multiplexed detection of xylene and trichloroethylene in water by photonic crystal absorption spectroscopy. *Opt. Lett.* **2013**, *38*, 3799–3802. DOI: [10.1364/OL.38.003799](https://doi.org/10.1364/OL.38.003799).
- [191] Luan, E.; Yun, H.; Laplatine, L.; Dattner, Y.; Ratner, D.M.; Cheung, K.C.; Chrostowski, L. Enhanced sensitivity of subwavelength multibox waveguide microring resonator label-free biosensors. *IEEE J. Select. Topics Quantum Electron.* **2019**, *25*, 1–11. DOI: [10.1109/JSTQE.2018.2821842](https://doi.org/10.1109/JSTQE.2018.2821842).
- [192] Lai, W.-C.; Chakravarty, S.; Wang, X.; Lin, C.; Chen, R.T. Photonic crystal slot waveguide absorption spectrometer for on-chip near-infrared spectroscopy of xylene in water. *Appl. Phys. Lett.* **2011**, *98*, 023304.
- [193] Katiyi, A.; Karabchevsky, A. Si nanostrip optical waveguide for on-chip broadband molecular overtone spectroscopy in near-infrared. *ACS Sens.* **2018**, *3*, 618–623. DOI: [10.1021/acssensors.7b00867](https://doi.org/10.1021/acssensors.7b00867).
- [194] Zou, Y.; Chakravarty, S.; Chung, C.-J.; Xu, X.; Chen, R.T. Mid-infrared silicon photonic waveguides and devices [invited]. *Photon. Res.* **2018**, *6*, 254–276. DOI: [10.1364/PRJ.6.000254](https://doi.org/10.1364/PRJ.6.000254).
- [195] Yazici, M.S.; Dong, B.; Hasan, D.; Sun, F.; Lee, C. Integration of MEMS IR detectors with MIR waveguides for sensing applications. *Opt. Express* **2020**, *28*, 11524–11537. DOI: [10.1364/OE.381279](https://doi.org/10.1364/OE.381279).
- [196] Lin, P.T.; Giammarco, J.; Borodinov, N.; Savchak, M.; Singh, V.; Kimerling, L.C.; Tan, D.T.H.; Richardson, K.A.; Luzinov, I.; Agarwal, A. Label-free water sensors using hybrid polymer–dielectric mid-infrared optical waveguides. *ACS Appl Mater Interfaces* **2015**, *7*, 11189–11194. DOI: [10.1021/acsami.5b01013](https://doi.org/10.1021/acsami.5b01013).
- [197] Ottonello-Briano, F.; Errando-Herranz, C.; Rödjegård, H.; Martin, H.; Sohlström, H.; Gylfason, K.B. Carbon dioxide absorption spectroscopy with a mid-infrared silicon photonic waveguide. *Opt. Lett.* **2020**, *45*, 109–112. DOI: [10.1364/OL.45.000109](https://doi.org/10.1364/OL.45.000109).
- [198] Singh, N.; Casas-Bedoya, A.; Hudson, D.D.; Read, A.; Mägi, E.; Eggleton, B.J. Mid-IR absorption sensing of heavy water using a silicon-on-sapphire waveguide. *Opt. Lett.* **2016**, *41*, 5776–5779. DOI: [10.1364/OL.41.005776](https://doi.org/10.1364/OL.41.005776).
- [199] Chen, Y.; Lin, H.; Hu, J.; Li, M. Heterogeneously integrated silicon photonics for the mid-infrared and spectroscopic sensing. *ACS Nano* **2014**, *8*, 6955–6961. DOI: [10.1021/nn501765k](https://doi.org/10.1021/nn501765k).
- [200] Mittal, V.; Nedeljkovic, M.; Carpenter, L.G.; Khokhar, A.Z.; Chong, H.M.H.; Mashanovich, G.Z.; Bartlett, P.N.; Wilkinson, J.S. Waveguide absorption spectroscopy of bovine serum albumin in the mid-infrared fingerprint region. *ACS Sens.* **2019**, *4*, 1749–1753. DOI: [10.1021/acssensors.9b00215](https://doi.org/10.1021/acssensors.9b00215).
- [201] Benítez, N.T.; Baumgartner, B.; Missinne, J.; Radosavljevic, S.; Wacht, D.; Hugger, S.; Leszcz, P.; Lendl, B.; Roelkens, G. Mid-IR sensing platform for trace analysis in aqueous solutions based on a germanium-on-silicon waveguide chip with mesoporous silica coating for analyte enrichment. *Opt. Express* **2020**, *28*, 27013–27027. DOI: [10.1364/OE.399646](https://doi.org/10.1364/OE.399646).
- [202] Robinson, J.T.; Preston, K.; Painter, O.; Lipson, M. First-principle derivation of gain in high-index-contrast waveguides. *Opt. Express* **2008**, *16*, 16659–16669. DOI: [10.1364/oe.16.016659](https://doi.org/10.1364/oe.16.016659).
- [203] Lin, P.T.; Kwok, S.W.; Lin, H.G.; Singh, V.; Kimerling, L.C.; Whitesides, G.M.; Agarwal, A. Mid-infrared spectrometer using opto-nano fluidic slot-waveguide for label-free on-chip chemical sensing. *Nano Lett.* **2014**, *14*, 231–238. DOI: [10.1021/nl403817z](https://doi.org/10.1021/nl403817z).
- [204] Lin, P.T.; Singh, V.; Hu, J.; Richardson, K.; Musgraves, J.D.; Luzinov, I.; Hensley, J.; Kimerling, L.C.; Agarwal, A. Chip-scale mid-infrared chemical sensors using air-clad pedestal silicon waveguides. *Lab Chip* **2013**, *13*, 2161–2166. DOI: [10.1039/c3lc50177a](https://doi.org/10.1039/c3lc50177a).
- [205] Liu, W.; Ma, Y.; Chang, Y.; Dong, B.; Wei, J.; Ren, Z.; Lee, C. Suspended silicon waveguide platform with subwavelength grating metamaterial cladding for long-wave infrared sensing applications. *Nanophotonics* **2021**, *10*, 1861–1870. DOI: [10.1515/nanoph-2021-0029](https://doi.org/10.1515/nanoph-2021-0029).
- [206] Vlk, M.; Datta, A.; Alberti, S.; Yallew, H.D.; Mittal, V.; Murugan, G.S.; Jágerská, J. Extraordinary evanescent field confinement waveguide sensor for mid-infrared trace gas spectroscopy. *Light Sci. Appl* **2021**, *10*, 26.

- [207] Zou, Y.; Chakravarty, S.; Wray, P.; Chen, R.T. Mid-infrared holey and slotted photonic crystal waveguides in silicon-on-sapphire for chemical warfare simulant detection. *Sens. Actuat. B Chem.* **2015**, *221*, 1094–1103. DOI: [10.1016/j.snb.2015.07.061](https://doi.org/10.1016/j.snb.2015.07.061).
- [208] Yoo, K.M.; Midkiff, J.; Rostamian, A.; Chung, C.; Dalir, H.; Chen, R.T. InGaAs membrane waveguide: A promising platform for monolithic integrated mid-infrared optical gas sensor. *ACS Sens.* **2020**, *5*, 861–869. DOI: [10.1021/acssensors.0c00180](https://doi.org/10.1021/acssensors.0c00180).
- [209] Zhou, H.; Li, D.; Hui, X.; Mu, X. Infrared metamaterial for surface-enhanced infrared absorption spectroscopy: Pushing the frontier of ultrasensitive on-chip sensing. *Int. J. Optomechatronics* **2021**, *15*, 97–119. DOI: [10.1080/15599612.2021.1953199](https://doi.org/10.1080/15599612.2021.1953199).
- [210] Cubukcu, E.; Zhang, S.; Park, Y.; Bartal, G.; Zhang, X. Split ring resonator sensors for infrared detection of single molecular monolayers. *Appl. Phys. Lett.* **2009**, *95*, 043113.
- [211] Neubrech, F.; Pucci, A.; Cornelius, T.W.; Karim, S.; García-Etxarri, A.; Aizpurua, J. Resonant plasmonic and vibrational coupling in a tailored nanoantenna for infrared detection. *Phys. Rev. Lett.* **2008**, *101*, 157403. DOI: [10.1103/PhysRevLett.101.157403](https://doi.org/10.1103/PhysRevLett.101.157403).
- [212] Huck, C.; Vogt, J.; Sendner, M.; Hengstler, D.; Neubrech, F.; Pucci, A. Plasmonic enhancement of infrared vibrational signals: Nanoslits versus nanorods. *ACS Photon.* **2015**, *2*, 1489–1497. DOI: [10.1021/acsp Photonics.5b00390](https://doi.org/10.1021/acsp Photonics.5b00390).
- [213] Hasan, D.; Ho, C.P.; Lee, C. Thermally tunable absorption-induced transparency by a quasi 3D bow-tie nanostructure for nonplasmonic and volumetric refractive index sensing at mid-IR. *Adv. Opt. Mater.* **2016**, *4*, 943–952. DOI: [10.1002/adom.201600014](https://doi.org/10.1002/adom.201600014).
- [214] Hasan, D.; Pitchappa, P.; Wang, J.; Wang, T.; Yang, B.; Ho, C.P.; Lee, C. Novel CMOS-compatible Mo–AlN–Mo platform for metamaterial-based mid-IR absorber. *ACS Photon.* **2017**, *4*, 302–315. DOI: [10.1021/acsp Photonics.6b00672](https://doi.org/10.1021/acsp Photonics.6b00672).
- [215] Hasan, D.; Lee, C. Hybrid metamaterial absorber platform for sensing of CO<sub>2</sub> gas at mid-IR. *Adv. Sci.* **2018**, *5*, 1700581.
- [216] Zhou, H.; Hui, X.; Li, D.; Hu, D.; Chen, X.; He, X.; Gao, L.; Huang, H.; Lee, C.; Mu, X. Metal–organic framework-surface-enhanced infrared absorption platform enables simultaneous on-chip sensing of greenhouse gases. *Adv. Sci.* **2020**, *7*, 2001173. DOI: [10.1002/advs.202001173](https://doi.org/10.1002/advs.202001173).
- [217] Li, D.; Zhou, H.; Hui, X.; He, X.; Huang, H.; Zhang, J.; Mu, X.; Lee, C.; Yang, Y. Multifunctional chemical sensing platform based on dual-resonant infrared plasmonic perfect absorber for on-chip detection of poly(ethyl cyanoacrylate). *Adv. Sci.* **2021**, *8*, 2101879. DOI: [10.1002/advs.202101879](https://doi.org/10.1002/advs.202101879).
- [218] Yoo, D.; Mohr, D.A.; Vidal-Codina, F.; John-Herpin, A.; Jo, M.; Kim, S.; Matson, J.; Caldwell, J.D.; Jeon, H.; Nguyen, N.; Martin-Moreno, L.; Peraire, J.; Altug, H.; Oh, S. High-contrast infrared absorption spectroscopy via mass-produced coaxial zero-mode resonators with sub-10 nm gaps. *Nano Lett.* **2018**, *18*, 1930–1936. DOI: [10.1021/acs.nanolett.7b05295](https://doi.org/10.1021/acs.nanolett.7b05295).
- [219] Cetin, A.E.; Etezadi, D.; Altug, H. Accessible nearfields by nanoantennas on nanop pedestals for ultrasensitive vibrational spectroscopy. *Adv. Opt. Mater.* **2014**, *2*, 866–872. DOI: [10.1002/adom.201400171](https://doi.org/10.1002/adom.201400171).
- [220] Wei, J.; Li, Y.; Chang, Y.; Hasan, D.M.N.; Dong, B.; Ma, Y.; Qiu, C.-W.; Lee, C. Ultrasensitive transmissive infrared spectroscopy via loss engineering of metallic nanoantennas for compact devices. *ACS Appl. Mater. Interfaces* **2019**, *11*, 47270–47278. DOI: [10.1021/acsa mi.9b18002](https://doi.org/10.1021/acsa mi.9b18002).
- [221] Zhou, H.; Li, D.; Ren, Z.; Mu, X.; Lee, C. Loss-induced phase transition in mid-infrared plasmonic metamaterials for ultrasensitive vibrational spectroscopy. *InfoMat* **2022**, *4*, e12349. DOI: [10.1002/inf2.12349](https://doi.org/10.1002/inf2.12349).
- [222] Nugroho, F.A.A.; Darmadi, I.; Cusinato, L.; Susarrey-Arce, A.; Schreuders, H.; Bannenberg, L.J.; da Silva Fanta, A.B.; Kadhodazadeh, S.; Wagner, J.B.; Antosiewicz, T.J.; Hellman, A.; Zhdanov, V.P.; Dam, B.; Langhammer, C. Metal–polymer hybrid nanomaterials for plasmonic ultrafast hydrogen detection. *Nat. Mater.* **2019**, *18*, 489–495. DOI: [10.1038/s41563-019-0325-4](https://doi.org/10.1038/s41563-019-0325-4).
- [223] Zhou, H.; Ren, Z.; Xu, C.; Xu, L.; Lee, C. MOF/polymer-integrated multi-hotspot mid-infrared nanoantennas for sensitive detection of CO<sub>2</sub> gas. *Nanomicro Lett.* **2022**, *14*, 207. DOI: [10.1007/s40820-022-00950-1](https://doi.org/10.1007/s40820-022-00950-1).
- [224] Tittl, A.; John-Herpin, A.; Leitis, A.; Arvelo, E.; R and Altug, H. Metasurface-based molecular biosensing aided by artificial intelligence. *Angew. Chem. Int. Ed. Engl.* **2019**, *58*, 14810–14822. DOI: [10.1002/anie.201901443](https://doi.org/10.1002/anie.201901443).
- [225] John-Herpin, A.; Kavungal, D.; von Mücke, L.; Altug, H. Infrared metasurface augmented by deep learning for monitoring dynamics between all major classes of biomolecules. *Adv. Mater.* **2021**, *33*, e2006054. DOI: [10.1002/adma.202006054](https://doi.org/10.1002/adma.202006054).
- [226] Zhou, H.; Ren, Z.; Li, D.; Xu, C.; Mu, X.; Lee, C. Dynamic construction of refractive index-dependent vibrations using surface plasmon-phonon polaritons. *Nat. Commun.* **2023**, *14*, 7316. DOI: [10.1038/s41467-023-43127-z](https://doi.org/10.1038/s41467-023-43127-z).
- [227] Ren, Z.; Zhang, Z.; Wei, J.; Dong, B.; Lee, C. Wavelength-multiplexed hook nanoantennas for machine learning enabled mid-infrared spectroscopy. *Nat. Commun.* **2022**, *13*, 3859. DOI: [10.1038/s41467-022-31520-z](https://doi.org/10.1038/s41467-022-31520-z).

- [228] Li, Z.; Zhang, H.; Nguyen, B.T.T.; Luo, S.; Liu, P.Y.; Zou, J.; Shi, Y.; Cai, H.; Yang, Z.; Jin, Y.; Hao, Y.; Zhang, Y.; Liu, A.-Q. Smart ring resonator-based sensor for multicomponent chemical analysis via machine learning. *Photon. Res.* **2021**, *9*, B38–B44. DOI: [10.1364/PRJ.411825](https://doi.org/10.1364/PRJ.411825).
- [229] Zhou, J.; Zhang, Z.; Dong, B.; Ren, Z.; Liu, W.; Lee, C. Midinfrared spectroscopic analysis of aqueous mixtures using artificial-intelligence-enhanced metamaterial waveguide sensing platform. *ACS Nano*. **2022**, *17*, 711–724. DOI: [10.1021/acsnano.2c10163](https://doi.org/10.1021/acsnano.2c10163).
- [230] Kapfinger, S.; Reichert, T.; Lichtmannecker, S.; Müller, K.; Finley, J.J.; Wixforth, A.; Kaniber, M.; Krenner, H.J. Dynamic acousto-optic control of a strongly coupled photonic molecule. *Nat. Commun.* **2015**, *6*, 8540. DOI: [10.1038/ncomms9540](https://doi.org/10.1038/ncomms9540).
- [231] Liang, Q.; Wang, Q.; Zhang, Q.; Wei, J.; Lim, S.X.; Zhu, R.; Hu, J.; Wei, W.; Lee, C.; Sow, C.; Zhang, W.; Wee, A.T.S. High-performance, room temperature, ultra-broadband photodetectors based on air-stable PdSe<sub>2</sub>. *Adv. Mater.* **2019**, *31*, 1807609.
- [232] Chen, P.-L.; Chen, Y.; Chang, T.-Y.; Li, W.-Q.; Li, J.-X.; Lee, S.; Fang, Z.; Li, M.; Majumdar, A.; Liu, C.-H. Waveguide-integrated Van Der Waals heterostructure mid-infrared photodetector with high performance. *ACS Appl. Mater. Interfaces* **2022**, *14*, 24856–24863. DOI: [10.1021/acsami.2c01094](https://doi.org/10.1021/acsami.2c01094).
- [233] Weber, P.; Güttinger, J.; Noury, A.; Vergara-Cruz, J.; Bachtold, A. Force sensitivity of multilayer graphene optomechanical devices. *Nat. Commun.* **2016**, *7*, 12496. DOI: [10.1038/ncomms12496](https://doi.org/10.1038/ncomms12496).
- [234] Zobenica, Ž.; van der Heijden, R.W.; Petruzzella, M.; Pagliano, F.; Leijssen, R.; Xia, T.; Midolo, L.; Cotrufo, M.; Cho, Y.; van Otten, F.W.M.; Verhagen, E.; Fiore, A. Integrated nano-opto-electro-mechanical sensor for spectrometry and nanometrology. *Nat. Commun.* **2017**, *8*, 2216. DOI: [10.1038/s41467-017-02392-5](https://doi.org/10.1038/s41467-017-02392-5).
- [235] Yang, Z.; Albrow-Owen, T.; Cai, W.; Hasan, T. Miniaturization of optical spectrometers. *Science* **2021**, *371*, eabe0722. DOI: [10.1126/science.abe0722](https://doi.org/10.1126/science.abe0722).
- [236] Muneeb, M.; Vasiliev, A.; Ruocco, A.; Malik, A.; Chen, H.; Nedeljkovic, M.; Penades, J.S.; Cerutti, L.; Rodriguez, J.B.; Mashanovich, G.Z.; Smit, M.K.; Tourni, E.; Roelkens, G. III-V-on-silicon integrated micro-spectrometer for the 3 μm wavelength range. *Opt. Express* **2016**, *24*, 9465–9472. DOI: [10.1364/OE.24.009465](https://doi.org/10.1364/OE.24.009465).
- [237] Pervez, N.K.; Cheng, W.; Jia, Z.; Cox, M.P.; Edrees, H.M.; Kyriassis, I. Photonic crystal spectrometer. *Opt. Express* **2010**, *18*, 8277–8285. DOI: [10.1364/OE.18.008277](https://doi.org/10.1364/OE.18.008277).
- [238] Emadi, A.; Wu, H.; de Graaf, G.; Wolffenbuttel, R. Design and implementation of a sub-nm resolution microspectrometer based on a linear-variable optical filter. *Opt. Express* **2012**, *20*, 489–507. DOI: [10.1364/OE.20.000489](https://doi.org/10.1364/OE.20.000489).
- [239] Ebermann, M.; Neumann, N.; Hiller, K.; Seifert, M.; Meinig, M.; Kurth, S. Tunable MEMS Fabry-Pérot filters for infrared microspectrometers: A review. *Proc. SPIE* **2016**, 9760, 97600H. DOI: [10.1117/12.2209288](https://doi.org/10.1117/12.2209288).
- [240] Velasco, A.V.; Cheben, P.; Bock, P.J.; Deläge, A.; Schmid, J.H.; Lapointe, J.; Janz, S.; Calvo, M.L.; Xu, D.-X.; Florjańczyk, M.; Vachon, M. High-resolution Fourier-transform spectrometer chip with microphotonic silicon spiral waveguides. *Opt. Lett.* **2013**, *38*, 706–708. DOI: [10.1364/OL.38.000706](https://doi.org/10.1364/OL.38.000706).
- [241] Zheng, S.N.; Zou, J.; Cai, H.; Song, J.F.; Chin, L.K.; Liu, P.Y.; Lin, Z.P.; Kwong, D.L.; Liu, A.Q. Microring resonator-assisted Fourier transform spectrometer with enhanced resolution and large bandwidth in single chip solution. *Nat. Commun.* **2019**, *10*, 2349. DOI: [10.1038/s41467-019-10282-1](https://doi.org/10.1038/s41467-019-10282-1).
- [242] Bao, J.; Bawendi, M.G. A colloidal quantum dot spectrometer. *Nature* **2015**, *523*, 67–70. DOI: [10.1038/nature14576](https://doi.org/10.1038/nature14576).
- [243] Wang, Z.; Yi, S.; Chen, A.; Zhou, M.; Luk, T.S.; James, A.; Nogan, J.; Ross, W.; Joe, G.; Shahsafi, A.; Wang, K.X.; Kats, M.A.; Yu, Z. Single-shot on-chip spectral sensors based on photonic crystal slabs. *Nat. Commun.* **2019**, *10*, 1020. DOI: [10.1038/s41467-019-08994-5](https://doi.org/10.1038/s41467-019-08994-5).
- [244] Li, A.; Fainman, Y. On-chip spectrometers using stratified waveguide filters. *Nat. Commun.* **2021**, *12*, 2704. DOI: [10.1038/s41467-021-23001-6](https://doi.org/10.1038/s41467-021-23001-6).
- [245] Meng, J.; Cadusch, J.J.; Crozier, K.B. Detector-only spectrometer based on structurally colored silicon nanowires and a reconstruction algorithm. *Nano Lett.* **2020**, *20*, 320–328. DOI: [10.1021/acs.nanolett.9b03862](https://doi.org/10.1021/acs.nanolett.9b03862).
- [246] Yang, Z.; Albrow-Owen, T.; Cui, H.; Alexander-Webber, J.; Gu, F.; Wang, X.; Wu, T.; Zhuge, M.; Williams, C.; Wang, P.; Zayats, A.V.; Cai, W.; Dai, L.; Hofmann, S.; Overend, M.; Tong, L.; Yang, Q.; Sun, Z.; Hasan, T. Single-nanowire spectrometers. *Science* **2019**, *365*, 1017–1020. DOI: [10.1126/science.aax8814](https://doi.org/10.1126/science.aax8814).
- [247] Podmore, H.; Scott, A.; Cheben, P.; Velasco, A.V.; Schmid, J.H.; Vachon, M.; Lee, R. Demonstration of a compressive-sensing Fourier-transform on-chip spectrometer. *Opt. Lett.* **2017**, *42*, 1440–1443. DOI: [10.1364/OL.42.001440](https://doi.org/10.1364/OL.42.001440).
- [248] Kita, D.M.; Miranda, B.; Favela, D.; Bono, D.; Michon, J.; Lin, H.; Gu, T.; Hu, J. High-performance and scalable on-chip digital Fourier transform spectroscopy. *Nat. Commun.* **2018**, *9*, 4405. DOI: [10.1038/s41467-018-06773-2](https://doi.org/10.1038/s41467-018-06773-2).



- [249] Chang, Y.; Xu, S.; Dong, B.; Wei, J.; Le, X.; Ma, Y.; Zhou, G.; Lee, C. Development of triboelectric-enabled tunable Fabry-Pérot photonic-crystal-slab filter towards wearable mid-infrared computational spectrometer. *Nano Energy* **2021**, *89*, 106446. DOI: [10.1016/j.nanoen.2021.106446](https://doi.org/10.1016/j.nanoen.2021.106446).
- [250] Yuan, S.; Naveh, D.; Watanabe, K.; Taniguchi, T.; Xia, F. A wavelength-scale black phosphorus spectrometer. *Nat. Photon.* **2021**, *15*, 601–607. DOI: [10.1038/s41566-021-00787-x](https://doi.org/10.1038/s41566-021-00787-x).
- [251] Yoon, H.H.; Fernandez, H.A.; Nigmatulin, F.; Cai, W.; Yang, Z.; Cui, H.; Ahmed, F.; Cui, X.; Uddin, M.G.; Minot, E.D.; Lipsanen, H.; Kim, K.; Hakonen, P.; Hasan, T.; Sun, Z. Miniaturized spectrometers with a tunable Van Der Waals junction. *Science* **2022**, *378*, 296–299. DOI: [10.1126/science.add8544](https://doi.org/10.1126/science.add8544).
- [252] Deng, W.; Zheng, Z.; Li, J.; Zhou, R.; Chen, X.; Zhang, D.; Lu, Y.; Wang, C.; You, C.; Li, S.; Sun, L.; Wu, Y.; Li, X.; An, B.; Liu, Z.; Wang, Q.; Duan, X.; Zhang, Y. Electrically tunable two-dimensional heterojunctions for miniaturized near-infrared spectrometers. *Nat. Commun.* **2022**, *13*, 4627. DOI: [10.1038/s41467-022-32306-z](https://doi.org/10.1038/s41467-022-32306-z).
- [253] Wang, H.; Chen, S.; Chen, X. Room-temperature self-powered infrared spectrometer based on a single black phosphorus heterojunction diode. *Nano Lett.* **2024**, *24*, 326–330. DOI: [10.1021/acs.nanolett.3c04044](https://doi.org/10.1021/acs.nanolett.3c04044).
- [254] Wang, J.; Pan, B.; Wang, Z.; Zhang, J.; Zhou, Z.; Yao, L.; Wu, Y.; Ren, W.; Wang, J.; Ji, H.; Yu, J.; Chen, B. Single-pixel p-graded-n junction spectrometers. *Nat. Commun.* **2024**, *15*, 1773. DOI: [10.1038/s41467-024-46066-5](https://doi.org/10.1038/s41467-024-46066-5).
- [255] Xu, H.; Qin, Y.; Hu, G.; Tsang, H.K. Breaking the resolution-bandwidth limit of chip-scale spectrometry by harnessing a dispersion-engineered photonic molecule. *Light Sci. Appl.* **2023**, *12*, 64.
- [256] Yao, C.; Xu, K.; Zhang, W.; Chen, M.; Cheng, Q.; Penty, R. Integrated reconstructive spectrometer with programmable photonic circuits. *Nat. Commun.* **2023**, *14*, 6376. DOI: [10.1038/s41467-023-42197-3](https://doi.org/10.1038/s41467-023-42197-3).
- [257] Xu, H.; Qin, Y.; Hu, G.; Tsang, H.K. Cavity-enhanced scalable integrated temporal random-speckle spectrometry. *Optica* **2023**, *10*, 1177–1188. DOI: [10.1364/OPTICA.492572](https://doi.org/10.1364/OPTICA.492572).
- [258] Qiao, Q.; Liu, X.; Ren, Z.; Dong, B.; Xia, J.; Sun, H.; Lee, C.; Zhou, G. MEMS-enabled on-chip computational mid-infrared spectrometer using silicon photonics. *ACS Photon.* **2022**, *9*, 2367–2377. DOI: [10.1021/acsp Photonics.2c00381](https://doi.org/10.1021/acsp Photonics.2c00381).
- [259] Zhang, E.J.; Martin, Y.; Orcutt, J.S.; Xiong, C.; Glodde, M.; Marchack, N.; Duch, E.A.; Barwicz, T.; Schares, L.; Green, W.M. Monolithically integrated silicon photonic chip sensor for near-infrared trace-gas spectroscopy. *Proc. SPIE* **2019**, *11010*, 110100B.
- [260] Su, P.; Han, Z.; Kita, D.; Becla, P.; Lin, H.; Deckoff-Jones, S.; Richardson, K.; Kimerling, L.C.; Hu, J.; Agarwal, A. Monolithic on-chip mid-IR methane gas sensor with waveguide-integrated detector. *Appl. Phys. Lett.* **2019**, *114*, 051103.
- [261] Altug, H.; Oh, S.H.; Maier, S.A.; Homola, J. Advances and applications of nanophotonic biosensors. *Nat. Nanotechnol.* **2022**, *17*, 5–16. DOI: [10.1038/s41565-021-01045-5](https://doi.org/10.1038/s41565-021-01045-5).
- [262] Le, T.H.H.; Tanaka, T. Plasmonics-nanofluidics hybrid metamaterial: An ultrasensitive platform for infrared absorption spectroscopy and quantitative measurement of molecules. *ACS Nano* **2017**, *11*, 9780–9788. DOI: [10.1021/acsnano.7b02743](https://doi.org/10.1021/acsnano.7b02743).
- [263] Xu, J.; Du, Y.; Tian, Y.; Wang, C. Progress in wafer bonding technology towards MEMS, high-power electronics, optoelectronics, and optofluidics. *Int. J. Optomechatronics* **2020**, *14*, 94–118. DOI: [10.1080/15599612.2020.1857890](https://doi.org/10.1080/15599612.2020.1857890).
- [264] Xu, J.; Ren, Z.; Dong, B.; Liu, X.; Wang, C.; Tian, Y.; Lee, C. Nanometer-scale heterogeneous interfacial sapphire wafer bonding for enabling plasmonic-enhanced nanofluidic mid-infrared spectroscopy. *ACS Nano* **2020**, *14*, 12159–12172. DOI: [10.1021/acsnano.0c05794](https://doi.org/10.1021/acsnano.0c05794).
- [265] Kaushal, H.; Kaddoum, G. Optical communication in space: Challenges and mitigation techniques. *IEEE Commun. Surv. Tutorials* **2017**, *19*, 57–96. DOI: [10.1109/COMST.2016.2603518](https://doi.org/10.1109/COMST.2016.2603518).
- [266] Bifano, T. Adaptive imaging mems deformable mirrors. *Nat. Photon.* **2011**, *5*, 21–23. DOI: [10.1038/nphoton.2010.297](https://doi.org/10.1038/nphoton.2010.297).
- [267] Li, L.; Stankovic, V.; Stankovic, L.; Li, L.; Cheng, S.; Uttamchandani, D. Single pixel optical imaging using a scanning MEMS mirror. *J. Micromech. Microeng.* **2011**, *21*, 025022. DOI: [10.1088/0960-1317/21/2/025022](https://doi.org/10.1088/0960-1317/21/2/025022).
- [268] Wang, D.; Watkins, C.; Xie, H. MEMS mirrors for LiDAR: A review. *Micromachines* **2020**, *11*, 456. DOI: [10.3390/mi11050456](https://doi.org/10.3390/mi11050456).
- [269] Aljasem, K.; Froehly, L.; Seifert, A.; Zappe, H. Scanning and tunable micro-optics for endoscopic optical coherence tomography. *J. Microelectromech. Syst.* **2011**, *20*, 1462–1472. DOI: [10.1109/JMEMS.2011.2167656](https://doi.org/10.1109/JMEMS.2011.2167656).
- [270] Chen, T.-H.; Fardel, R.; Arnold, C.B. Ultrafast z-scanning for high-efficiency laser micro-machining. *Light Sci. Appl.* **2018**, *7*, 17181. DOI: [10.1038/lsa.2017.181](https://doi.org/10.1038/lsa.2017.181).
- [271] Jia, K.; Pal, S.; Xie, H. An electrothermal tip-tilt-piston micromirror based on folded dual s-shaped bimorphs. *J. Microelectromech. Syst.* **2009**, *18*, 1004–1015. DOI: [10.1109/JMEMS.2009.2023838](https://doi.org/10.1109/JMEMS.2009.2023838).

- [272] Wang, D.; Zhang, J.; Liu, L.; Yan, Z.; Wang, P.; Ding, Y.; Xie, H.; Zhang, J.; Liu, L.; Yan, Z.; Wang, P.; Ding, Y.; Xie, H. Application of OCT for osteonecrosis using an endoscopic probe based on an electro-thermal MEMS scanning mirror. *Int. J. Optomechatronics* **2021**, *15*, 87–96. DOI: [10.1080/15599612.2021.1923876](https://doi.org/10.1080/15599612.2021.1923876).
- [273] Manh, C.H.; Hane, K. Vacuum operation of comb-drive micro display mirrors. *J. Micromech. Microeng.* **2009**, *19*, 105018. DOI: [10.1088/0960-1317/19/10/105018](https://doi.org/10.1088/0960-1317/19/10/105018).
- [274] Chen, H.; Chen, A.; Sun, W.J.; Sun, Z.D.; Yeow, J.T.W. Closed-loop control of a 2-D MEMS micromirror with sidewall electrodes for a laser scanning microscope system. *Int. J. Optomechatronics* **2016**, *10*, 1–13. DOI: [10.1080/15599612.2015.1095956](https://doi.org/10.1080/15599612.2015.1095956).
- [275] Koh, K.H.; Kobayashi, T.; Hsiao, F.L.; Lee, C. Characterization of piezoelectric PZT beam actuators for driving 2D scanning micromirrors. *Sens. Actuat. A Phys.* **2010**, *162*, 336–347. DOI: [10.1016/j.sna.2010.04.021](https://doi.org/10.1016/j.sna.2010.04.021).
- [276] Koh, K.H.; Kobayashi, T.; Xie, J.; Yu, A.; Lee, C. Novel piezoelectric actuation mechanism for a gimbal-less mirror in 2D raster scanning applications. *J. Micromech. Microeng.* **2011**, *21*, 075001. DOI: [10.1088/0960-1317/21/7/075001](https://doi.org/10.1088/0960-1317/21/7/075001).
- [277] Urey, H.; Holmstrom, S.; Yalcinkaya, A.D. Electromagnetically actuated FR4 scanners. *IEEE Photon. Technol. Lett.* **2008**, *20*, 30–32. DOI: [10.1109/LPT.2007.911522](https://doi.org/10.1109/LPT.2007.911522).
- [278] Yalcinkaya, A.D.; Urey, H.; Brown, D.; Montague, T.; Sprague, R. Two-axis electromagnetic microscanner for high resolution displays. *J. Microelectromech. Syst.* **2006**, *15*, 786–794. DOI: [10.1109/JMEMS.2006.879380](https://doi.org/10.1109/JMEMS.2006.879380).
- [279] Brown, G.; Li, L.; Bauer, R.; Liu, J.; Uttamchandani, D. A two-axis hybrid MEMS scanner incorporating electrothermal and electrostatic actuators. In *2010 International Conference on Optical MEMS and Nanophotonics*; Sapporo, Japan; 09–12 August 2010; IEEE: Piscataway, NJ, 2010; pp 115–116. DOI: [10.1109/OMEMS.2010.5672156](https://doi.org/10.1109/OMEMS.2010.5672156).
- [280] Li, L.; Bauer, R.; Brown, G.; Uttamchandani, D. A symmetric hybrid MEMS scanner with electrothermal and electrostatic actuators. In *16th International Conference on Optical MEMS and Nanophotonics*; Istanbul, Turkey; 08–11 August 2011; IEEE: Piscataway, NJ, 2011; pp 163–164. DOI: [10.1109/OMEMS.2011.6031038](https://doi.org/10.1109/OMEMS.2011.6031038).
- [281] Lerch, P.; Kara Slimane, C.; Romanowicz, B.; Renaud, P. Modelization and characterization of asymmetrical thermal micro-actuators. *J. Micromech. Microeng.* **1996**, *6*, 134–137. DOI: [10.1088/0960-1317/6/1/033](https://doi.org/10.1088/0960-1317/6/1/033).
- [282] Lai, Y.J.; Lee, C.; Wu, C.Y.; Chen, W.C.; Chen, C.; Lin, Y.S.; Fang, W.; Huang, R.S. Development of electrothermal actuator with optimized motion characteristics. *Jpn. J. Appl. Phys.* **2003**, *42*, 4067–4073. DOI: [10.1143/JJAP.42.4067](https://doi.org/10.1143/JJAP.42.4067).
- [283] DeVoe, D.L. Thermal issues in MEMS and microscale systems. *IEEE Trans. Comp. Packag. Technol.* **2002**, *25*, 576–583. DOI: [10.1109/TCAPT.2003.809110](https://doi.org/10.1109/TCAPT.2003.809110).
- [284] Yeh J.A.; Jiang, S.S.; Lee, C. MOEMS variable optical attenuators using rotary comb drive actuators. *IEEE Photon. Technol. Lett.* **2006**, *18*, 1170–1172. DOI: [10.1109/LPT.2006.873959](https://doi.org/10.1109/LPT.2006.873959).
- [285] Koh, K.H.; Lee, C.; Kobayashi, T. A piezoelectric-driven three-dimensional MEMS VOA using attenuation mechanism with combination of rotational and translational effects. *J. Microelectromech. Syst.* **2010**, *19*, 1370–1379. DOI: [10.1109/JMEMS.2010.2076785](https://doi.org/10.1109/JMEMS.2010.2076785).
- [286] Koh, K.H.; Kobayashi, T.; Lee, C. A 2-D MEMS scanning mirror based on dynamic mixed mode excitation of a piezoelectric PZT thin film S-shaped actuator. *Opt. Express* **2011**, *19*, 13812–13824. DOI: [10.1364/OE.19.013812](https://doi.org/10.1364/OE.19.013812).
- [287] Koh, K.H.; Kobayashi, T.; Lee, C. Investigation of piezoelectric driven MEMS mirrors based on single and double S-shaped PZT actuator for 2-D scanning applications. *Sensors Actuat. A Phys.* **2012**, *184*, 149–159. DOI: [10.1016/j.sna.2012.06.018](https://doi.org/10.1016/j.sna.2012.06.018).
- [288] Koh, K.H.; Qian, Y.; Lee, C. Design and characterization of a 3D MEMS VOA driven by hybrid electromagnetic and electrothermal actuation mechanisms. *J. Micromech. Microeng.* **2012**, *22*, 105031. DOI: [10.1088/0960-1317/22/10/105031](https://doi.org/10.1088/0960-1317/22/10/105031).
- [289] Koh, K.H.; Soon, B.W.; Tsai, J.M.; Danner, A.J.; Lee, C. Study of hybrid driven micromirrors for 3-D variable optical attenuator applications. *Opt. Express* **2012**, *20*, 21598–21611. DOI: [10.1364/OE.20.021598](https://doi.org/10.1364/OE.20.021598).
- [290] Lin, Y.-S.; Ma, F.; Lee, C. Three-dimensional movable metamaterial using electric split-ring resonators. *Opt. Lett.* **2013**, *38*, 3126–3128. DOI: [10.1364/OL.38.003126](https://doi.org/10.1364/OL.38.003126).
- [291] Ma, F.; Lin, Y.-S.; Zhang, X.; Lee, C. Tunable multiband terahertz metamaterials using a reconfigurable electric split-ring resonator array. *Light Sci. Appl.* **2014**, *3*, e171–e171. DOI: [10.1038/lsa.2014.52](https://doi.org/10.1038/lsa.2014.52).
- [292] Pitchappa, P.; Manjappa, M.; Ho, C.P.; Singh, R.; Singh, N.; Lee, C. Active control of electromagnetically induced transparency analog in terahertz MEMS metamaterial. *Adv. Opt. Mater.* **2016**, *4*, 541–547. DOI: [10.1002/adom.201500676](https://doi.org/10.1002/adom.201500676).

- [293] Pitchappa, P.; Ho, C.P.; Cong, L.; Singh, R.; Singh, N.; Lee, C. Reconfigurable digital metamaterial for dynamic switching of terahertz anisotropy. *Adv. Opt. Mater.* **2016**, *4*, 391–398. DOI: [10.1002/adom.201500588](https://doi.org/10.1002/adom.201500588).
- [294] Shirmanesh, G.K.; Sokhoyan, R.; Wu, P.C.; Wu, P.C.; Atwater, H.A.; Atwater, H.A. Electro-optically tunable multifunctional metasurfaces. *ACS Nano* **2020**, *14*, 6912–6920. DOI: [10.1021/acsnano.0c01269](https://doi.org/10.1021/acsnano.0c01269).
- [295] Zhao, X.; Schalch, J.; Zhang, J.; Seren, H.R.; Duan, G.; Averitt, R.D.; Zhang, X. Electromechanically tunable metasurface transmission waveplate at terahertz frequencies. *Optica* **2018**, *5*, 303–310. DOI: [10.1364/OPTICA.5.000303](https://doi.org/10.1364/OPTICA.5.000303).
- [296] Manjappa, M.; Pitchappa, P.; Wang, N.; Lee, C.; Singh, R. Active control of resonant cloaking in a terahertz MEMS metamaterial. *Adv. Opt. Mater.* **2018**, *6*, 1800141. DOI: [10.1002/adom.201800141](https://doi.org/10.1002/adom.201800141).
- [297] Lin, Y.S.; Xu, Z. Reconfigurable metamaterials for optoelectronic applications. *Int. J. Optomechatronics* **2020**, *14*, 78–93. DOI: [10.1080/15599612.2020.1834655](https://doi.org/10.1080/15599612.2020.1834655).
- [298] Pitchappa, P.; Ho, C.P.; Dhakar, L.; Lee, C. Microelectromechanically reconfigurable interpixelated metamaterial for independent tuning of multiple resonances at terahertz spectral region. *Optica* **2015**, *2*, 571–578. DOI: [10.1364/OPTICA.2.000571](https://doi.org/10.1364/OPTICA.2.000571).
- [299] Arbabi, E.; Arbabi, A.; Kamali, S.M.; Horie, Y.; Faraji-Dana, M.; Faraon, A. MEMS-tunable dielectric metasurface lens. *Nat. Commun.* **2018**, *9*, 812. DOI: [10.1038/s41467-018-03155-6](https://doi.org/10.1038/s41467-018-03155-6).
- [300] Kwon, H.; Faraon, A. NEMS-tunable dielectric chiral metasurfaces. *ACS Photon.* **2021**, *8*, 2980–2986. DOI: [10.1021/acsp Photonics.1c00898](https://doi.org/10.1021/acsp Photonics.1c00898).
- [301] Seok, T.J.; Quack, N.; Han, S.; Muller, R.S.; Wu, M.C. Large-scale broadband digital silicon photonic switches with vertical adiabatic couplers: Supplementary material. *Optica* **2016**, *3*, 64–70. DOI: [10.1364/OPTICA.3.000064](https://doi.org/10.1364/OPTICA.3.000064).
- [302] Akihama, Y.; Hane, K. Single and multiple optical switches that use freestanding silicon nanowire waveguide couplers. *Light Sci. Appl.* **2012**, *1*, e16–e16. DOI: [10.1038/lssa.2012.16](https://doi.org/10.1038/lssa.2012.16).
- [303] Takabayashi, A.Y.; Sattari, H.; Edinger, P.; Verheyen, P.; Gylfason, K.B.; Bogaerts, W.; Quack, N. Broadband compact single-pole double-throw silicon photonic MEMS switch. *J. Microelectromech. Syst.* **2021**, *30*, 322–329. DOI: [10.1109/JMEMS.2021.3060182](https://doi.org/10.1109/JMEMS.2021.3060182).
- [304] Han, S.; Beguelin, J.; Ochikubo, L.; Jacobs, J.; Seok, T.J.; Yu, K.; Quack, N.; Kim, C.-K.; Muller, R.S.; Wu, M.C.  $32 \times 32$  Silicon photonic MEMS switch with gap-adjustable directional couplers fabricated in commercial CMOS foundry. *J. Opt. Microsyst.* **2021**, *1*, 024003.
- [305] Qiao, Q.; Yazici, M.S.; Dong, B.; Liu, X.; Lee, C.; Zhou, G. Multifunctional mid-infrared photonic switch using a MEMS-based tunable waveguide coupler. *Opt. Lett.* **2020**, *45*, 5620–5623. DOI: [10.1364/OL.400132](https://doi.org/10.1364/OL.400132).
- [306] Quack, N.; Sattari, H.; Takabayashi, A.Y.; Zhang, Y.; Verheyen, P.; Bogaerts, W.; Edinger, P.; Errando-Herranz, C.; Gylfason, K.B. MEMS-enabled silicon photonic integrated devices and circuits. *IEEE J. Quantum Electron.* **2020**, *56*, 1–10. DOI: [10.1109/JQE.2019.2946841](https://doi.org/10.1109/JQE.2019.2946841).
- [307] Quack, N.; Takabayashi, A.Y.; Sattari, H.; Edinger, P.; Jo, G.; Bleiker, S.J.; Errando-Herranz, C.; Gylfason, K.B.; Niklaus, F.; Khan, U.; Verheyen, P.; Mallik, A.K.; Lee, J.S.; Jezzini, M.; Morrissey, P.; Antony, C.; O'Brien, P.; Bogaerts, W. Integrated silicon photonic MEMS. *Microsyst. Nanoeng.* **2023**, *9*, 27.
- [308] Bogaerts, W.; Sattari, H.; Edinger, P.; Takabayashi, A.Y.; Zand, I.; Wang, X.; Ribeiro, A.; Jezzini de Anda, M.A.; Errando-Herranz, C.; Talli, G.; Saurav, K.; Garcia Porcel, M.A.; Verheyen, P.; Abasahl, B.; Niklaus, F.; Quack, N.; Gylfason, K.B.; O'Brien, P.; Khan, M.U.. MORPHIC: Programmable photonic circuits enabled by silicon photonic MEMS. In *Silicon Photonics XV*; Reed, G.T.; Knights, A.P., Eds.; SPIE: Bellingham, WA; 2020; vol 11285; pp. 1128503. DOI: [10.1117/12.2540934](https://doi.org/10.1117/12.2540934).
- [309] Bogaerts, W.; Pérez, D.; Capmany, J.; Miller, D.A.B.; Poon, J.; Englund, D.; Morichetti, F.; Melloni, A. Programmable photonic circuits. *Nature* **2020**, *586*, 207–216. DOI: [10.1038/s41586-020-2764-0](https://doi.org/10.1038/s41586-020-2764-0).
- [310] Errando-Herranz, C.; Takabayashi, A.Y.; Edinger, P.; Sattari, H.; Gylfason, K.B.; Quack, N. MEMS for photonic integrated circuits. *IEEE J. Select. Topics Quantum Electron.* **2020**, *26*, 1–16. DOI: [10.1109/JSTQE.2019.2943384](https://doi.org/10.1109/JSTQE.2019.2943384).
- [311] Dong, M.; Clark, G.; Leenheer, A.J.; Zimmermann, M.; Dominguez, D.; Menssen, A.J.; Heim, D.; Gilbert, G.; Englund, D.; Eichenfield, M. High-speed programmable photonic circuits in a cryogenically compatible, visible–near-infrared 200 mm CMOS architecture. *Nat. Photon.* **2021**, *16*, 59–65. DOI: [10.1038/s41566-021-00903-x](https://doi.org/10.1038/s41566-021-00903-x).
- [312] Stegmaier, M.; Ríos, C.; Bhaskaran, H.; Wright, C.D.; Pernice, W.H.P. Nonvolatile all-optical  $1 \times 2$  switch for chipscale photonic networks. *Adv. Opt. Mater.* **2017**, *5*, 1600346.
- [313] Zhang, H.; Zhou, L.; Lu, L.; Xu, J.; Wang, N.; Hu, H.; Rahman, B.M.A.; Zhou, Z.; Chen, J. Miniature multilevel optical memristive switch using phase change material. *ACS Photon.* **2019**, *6*, 2205–2212. DOI: [10.1021/acsp Photonics.9b00819](https://doi.org/10.1021/acsp Photonics.9b00819).

- [314] Abdollahramezani, S.; Hemmatyar, O.; Taghinejad, H.; Krasnok, A.; Kiarashinejad, Y.; Zandehshahvar, M.; Alù, A.; Adibi, A. Tunable nanophotonics enabled by chalcogenide phase-change materials. *Nanophotonics* **2020**, *9*, 1189–1241. DOI: [10.1515/nanoph-2020-0039](https://doi.org/10.1515/nanoph-2020-0039).
- [315] Fang, Z.; Chen, R.; Zheng, J.; Majumdar, A. Non-volatile reconfigurable silicon photonics based on phase-change materials. *IEEE J. Select. Topics Quantum Electron.* **2022**, *28*, 1–17. DOI: [10.1109/JSTQE.2021.3120713](https://doi.org/10.1109/JSTQE.2021.3120713).
- [316] Wu, C.; Yu, H.; Li, H.; Zhang, X.; Takeuchi, I.; Li, M. Low-loss integrated photonic switch using subwavelength patterned phase change material. *ACS Photon.* **2019**, *6*, 87–92. DOI: [10.1021/acsp Photonics.8b01516](https://doi.org/10.1021/acsp Photonics.8b01516).
- [317] Ríos, C.; Stegmaier, M.; Hosseini, P.; Wang, D.; Scherer, T.; Wright, C.D.; Bhaskaran, H.; Pernice, W.H.P. Integrated all-photonic non-volatile multi-level memory. *Nat. Photon.* **2015**, *9*, 725–732. DOI: [10.1038/nphoton.2015.182](https://doi.org/10.1038/nphoton.2015.182).
- [318] Cheng, Z.; Ríos, C.; Pernice, W.H.P.; Wright, C.D.; Bhaskaran, H. On-chip photonic synapse. *Sci. Adv.* **2017**, *3*, e1700160. DOI: [10.1126/sciadv.1700160](https://doi.org/10.1126/sciadv.1700160).
- [319] Feldmann, J.; Youngblood, N.; Karpov, M.; Gehring, H.; Li, X.; Stappers, M.; Le Gallo, M.; Fu, X.; Lukashchuk, A.; Raja, A.S.; Liu, J.; Wright, C.D.; Sebastian, A.; Kippenberg, T.J.; Pernice, W.H.P.; Bhaskaran, H. Parallel convolutional processing using an integrated photonic tensor core. *Nature* **2021**, *589*, 52–58. DOI: [10.1038/s41586-020-03070-1](https://doi.org/10.1038/s41586-020-03070-1).
- [320] Feldmann, J.; Youngblood, N.; Wright, C.D.; Bhaskaran, H.; Pernice, W.H.P. All-optical spiking neurosynaptic networks with self-learning capabilities. *Nature* **2019**, *569*, 208–214. DOI: [10.1038/s41586-019-1157-8](https://doi.org/10.1038/s41586-019-1157-8).
- [321] Dregely, D.; Lindfors, K.; Lippitz, M.; Engheta, N.; Totzeck, M.; Giessen, H. Imaging and steering an optical wireless nanoantenna link. *Nat. Commun.* **2014**, *5*, 4354. DOI: [10.1038/ncomms5354](https://doi.org/10.1038/ncomms5354).
- [322] Wolf, O.; Campione, S.; Benz, A.; Ravikumar, A.P.; Liu, S.; Luk, T.S.; Kadlec, E.A.; Shaner, E.A.; Klem, J.F.; Sinclair, M.B.; Brener, I. Phased-array sources based on nonlinear metamaterial nanocavities. *Nat. Commun.* **2015**, *6*, 7667. DOI: [10.1038/ncomms8667](https://doi.org/10.1038/ncomms8667).
- [323] Wei, X.Y.; Wang, X.; Kuang, S.Y.; Su, L.; Li, H.Y.; Wang, Y.; Pan, C.; Wang, Z.L.; Zhu, G. Dynamic triboelectrification-induced electroluminescence and its use in visualized sensing. *Adv. Mater.* **2016**, *28*, 6656–6664. DOI: [10.1002/adma.201600604](https://doi.org/10.1002/adma.201600604).
- [324] Fang, H.; Tian, H.; Li, J.; Li, Q.; Dai, J.; Ren, T.L.; Dong, G.; Yan, Q. Self-powered flat panel displays enabled by motion-driven alternating current electroluminescence. *Nano Energy* **2016**, *20*, 48–56. DOI: [10.1016/j.nanoen.2015.12.001](https://doi.org/10.1016/j.nanoen.2015.12.001).
- [325] He, T.; Wang, H.; Wang, J.; Tian, X.; Wen, F.; Shi, Q.; Ho, J.S.; Lee, C. Self-sustainable wearable textile nano-energy nano-system (NENS) for next-generation healthcare applications. *Adv. Sci.* **2019**, *6*, 1901437.
- [326] Zhu, M.; Shi, Q.; He, T.; Yi, Z.; Ma, Y.; Yang, B.; Chen, T.; Lee, C. Self-powered and self-functional cotton sock using piezoelectric and triboelectric hybrid mechanism for healthcare and sports monitoring. *ACS Nano* **2019**, *13*, 1940–1952. DOI: [10.1021/acsnano.8b08329](https://doi.org/10.1021/acsnano.8b08329).
- [327] He, T.; Shi, Q.; Wang, H.; Wen, F.; Chen, T.; Ouyang, J.; Lee, C. Beyond energy harvesting – multi-functional triboelectric nanosensors on a textile. *Nano Energy* **2019**, *57*, 338–352. DOI: [10.1016/j.nanoen.2018.12.032](https://doi.org/10.1016/j.nanoen.2018.12.032).
- [328] Kwak, S.S.; Yoon, H.J.; Kim, S.W. Textile-based triboelectric nanogenerators for self-powered wearable electronics. *Adv. Funct. Mater.* **2019**, *29*, 1804533.
- [329] Dong, B.; Shi, Q.; He, T.; Zhu, S.; Zhang, Z.; Sun, Z.; Ma, Y.; Kwong, D.; Lee, C. Wearable triboelectric/aluminum nitride nano-energy-nano-system with self-sustainable photonic modulation and continuous force sensing. *Adv. Sci.* **2020**, *7*, 1903636.
- [330] Dong, B.; Yang, Y.; Shi, Q.; Xu, S.; Sun, Z.; Zhu, S.; Zhang, Z.; Kwong, D.L.; Zhou, G.; Ang, K.W.; Lee, C. Wearable triboelectric-human-machine interface (THMI) using robust nanophotonic readout. *ACS Nano* **2020**, *14*, 8915–8930. DOI: [10.1021/acsnano.0c03728](https://doi.org/10.1021/acsnano.0c03728).
- [331] Sun, Z.; Zhu, M.; Lee, C. Progress in the triboelectric human-machine interfaces (HMIs)-Moving from smart gloves to AI/haptic enabled HMI in the 5G/IoT era. *Nanoenergy Adv.* **2021**, *1*, 81–121. DOI: [10.3390/nanoenergyadv1010005](https://doi.org/10.3390/nanoenergyadv1010005).
- [332] Wen, F.; Zhang, Z.; He, T.; Lee, C. AI enabled sign language recognition and VR space bidirectional communication using triboelectric smart glove. *Nat. Commun.* **2021**, *12*, 5378. DOI: [10.1038/s41467-021-25637-w](https://doi.org/10.1038/s41467-021-25637-w).
- [333] Zhang, Z.; He, T.; Zhu, M.; Sun, Z.; Shi, Q.; Zhu, J.; Dong, B.; Yuce, M.R.; Lee, C. Deep learning-enabled triboelectric smart socks for IoT-based gait analysis and VR applications. *NPJ Flex. Electron.* **2020**, *4*, 29.
- [334] Shi, Q.; Zhang, Z.; He, T.; Sun, Z.; Wang, B.; Feng, Y.; Shan, X.; Salam, B.; Lee, C. Deep learning enabled smart mats as a scalable floor monitoring system. *Nat. Commun.* **2020**, *11*, 4609. DOI: [10.1038/s41467-020-18471-z](https://doi.org/10.1038/s41467-020-18471-z).

- [335] Zhou, H.; Dong, J.; Cheng, J.; Dong, W.; Huang, C.; Shen, Y.; Zhang, Q.; Gu, M.; Qian, C.; Chen, H.; Ruan, Z.; Zhang, X. Photonic matrix multiplication lights up photonic accelerator and beyond. *Light Sci. Appl.* **2022**, *11*, 30.
- [336] Shastri, B.J.; Tait, A.N.; Ferreira de Lima, T.; Pernice, W.H.P.; Bhaskaran, H.; Wright, C.D.; Prucnal, P.R. Photonics for artificial intelligence and neuromorphic computing. *Nat. Photon.* **2021**, *15*, 102–114. DOI: [10.1038/s41566-020-00754-y](https://doi.org/10.1038/s41566-020-00754-y).
- [337] Dong, B.; Aggarwal, S.; Zhou, W.; Ali, U.E.; Farmakidis, N.; Lee, J.S.; He, Y.; Li, X.; Kwong, D.; Wright, C.D.; Pernice, W.H.P.; Bhaskaran, H. Higher-dimensional processing using a photonic tensor core with continuous-time data. *Nat. Photon.* **2023**, *17*, 1080–1088. DOI: [10.1038/s41566-023-01313-x](https://doi.org/10.1038/s41566-023-01313-x).
- [338] Van Acoleyen, K.; Bogaerts, W.; Jágerská, J.; Le Thomas, N.; Houdré, R.; Baets, R. Off-chip beam steering with a one-dimensional optical phased array on silicon-on-insulator. *Opt. Lett.* **2009**, *34*, 1477–1479. DOI: [10.1364/ol.34.001477](https://doi.org/10.1364/ol.34.001477).
- [339] Van Acoleyen, K.; Rogier, H.; Baets, R. Two-dimensional optical phased array antenna on silicon-on-insulator. *Opt. Express* **2010**, *18*, 13655–13660. DOI: [10.1364/OE.18.013655](https://doi.org/10.1364/OE.18.013655).
- [340] Doylend, J.K.; Heck, M.J.R.; Bovington, J.T.; Peters, J.D.; Coldren, L.A.; Bowers, J.E. Two-dimensional free-space beam steering with an optical phased array on silicon-on-insulator. *Opt. Express* **2011**, *19*, 21595–21604. DOI: [10.1364/OE.19.021595](https://doi.org/10.1364/OE.19.021595).
- [341] Kwong, D.; Hosseini, A.; Zhang, Y.; Chen, R.T.  $1 \times 12$  Unequally spaced waveguide array for actively tuned optical phased array on a silicon nanomembrane. *Appl. Phys. Lett.* **2011**, *99*, 051104.
- [342] Sun, J.; Timurdogan, E.; Yaacobi, A.; Hosseini, E.S.; Watts, M.R. Large-scale nanophotonic phased array. *Nature* **2013**, *493*, 195–199. DOI: [10.1038/nature11727](https://doi.org/10.1038/nature11727).
- [343] Aflatouni, F.; Abiri, B.; Rekhi, A.; Hajimiri, A. Nanophotonic coherent imager. *Opt. Express* **2015**, *23*, 5117–5125. DOI: [10.1364/OE.23.005117](https://doi.org/10.1364/OE.23.005117).
- [344] Inoue, D.; Ichikawa, T.; Kawasaki, A.; Yamashita, T. Demonstration of a new optical scanner using silicon photonics integrated circuit. *Opt. Express* **2019**, *27*, 2499–2508. DOI: [10.1364/OE.27.002499](https://doi.org/10.1364/OE.27.002499).
- [345] Li, C.; Cao, X.; Wu, K.; Li, X.; Chen, J. Lens-based integrated 2D beam-steering device with defocusing approach and broadband pulse operation for lidar application. *Opt. Express* **2019**, *27*, 32970–32983. DOI: [10.1364/OE.27.032970](https://doi.org/10.1364/OE.27.032970).
- [346] Wang, Y.; Zhou, G.; Zhang, X.; Kwon, K.; Blanche, P.-A.; Triesault, N.; Yu, K.; Wu, M.C. 2D broadband beamsteering with large-scale MEMS optical phased array. *Optica* **2019**, *6*, 557–562. DOI: [10.1364/OPTICA.6.000557](https://doi.org/10.1364/OPTICA.6.000557).
- [347] Miller, S.A.; Chang, Y.-C.; Phare, C.T.; Shin, M.C.; Zadka, M.; Roberts, S.P.; Stern, B.; Ji, X.; Mohanty, A.; Jimenez Gordillo, O.A.; Dave, U.D.; Lipson, M. Large-scale optical phased array using a low-power multipass silicon photonic platform. *Optica* **2020**, *7*, 3–6. DOI: [10.1364/OPTICA.7.000003](https://doi.org/10.1364/OPTICA.7.000003).
- [348] Kim, T.; Bhargava, P.; Poulton, C.V.; Notaros, J.; Yaacobi, A.; Timurdogan, E.; Baiocco, C.; Fahrenkopf, N.; Kruger, S.; Ngai, T.; Timalina, Y.; Watts, M.R.; Stojanovic, V. A single-chip optical phased array in a wafer-scale silicon photonics/CMOS 3D-integration platform. *IEEE J. Solid-State Circuits* **2019**, *54*, 3061–3074. DOI: [10.1109/JSSC.2019.2934601](https://doi.org/10.1109/JSSC.2019.2934601).
- [349] Fatemi, R.; Khachatryan, A.; Hajimiri, A. A nonuniform sparse 2-D large-FOV optical phased array with a low-power PWM drive. *IEEE J. Solid-State Circuits* **2019**, *54*, 1200–1215. DOI: [10.1109/JSSC.2019.2896767](https://doi.org/10.1109/JSSC.2019.2896767).
- [350] Cao, X.; Qiu, G.; Wu, K.; Li, C.; Chen, J. Lidar system based on lens assisted integrated beam steering. *Opt. Lett.* **2020**, *45*, 5816–5819. DOI: [10.1364/OL.401486](https://doi.org/10.1364/OL.401486).
- [351] Ito, H.; Kusunoki, Y.; Maeda, J.; Akiyama, D.; Kodama, N.; Abe, H.; Tetsuya, R.; Baba, T. Wide beam steering by slow-light waveguide gratings and a prism lens. *Optica* **2020**, *7*, 47–52. DOI: [10.1364/OPTICA.381484](https://doi.org/10.1364/OPTICA.381484).
- [352] Abe, H.; Takeuchi, M.; Takeuchi, G.; Ito, H.; Yokokawa, T.; Kondo, K.; Furukado, Y.; Baba, T. Two-dimensional beam-steering device using a doubly periodic Si photonic-crystal waveguide. *Opt. Express* **2018**, *26*, 9389–9397. DOI: [10.1364/OE.26.009389](https://doi.org/10.1364/OE.26.009389).
- [353] Zhang, X.; Kwon, K.; Henriksson, J.; Luo, J.; Wu, M.C. A large-scale microelectromechanical-systems-based silicon photonics LiDAR. *Nature* **2022**, *603*, 253–258. DOI: [10.1038/s41586-022-04415-8](https://doi.org/10.1038/s41586-022-04415-8).
- [354] Bogaerts, W.; Rahim, A. Programmable photonics: An opportunity for an accessible large-volume PIC ecosystem. *IEEE J. Select. Topics Quantum Electron.* **2020**, *26*, 1–17. DOI: [10.1109/JSTQE.2020.2982980](https://doi.org/10.1109/JSTQE.2020.2982980).
- [355] Kim, D.U.; Park, Y.J.; Kim, D.Y.; Jeong, Y.; Lim, M.G.; Hong, M.S.; Her, M.J.; Rah, Y.; Choi, D.J.; Han, S.; Yu, K. Programmable photonic arrays based on microelectromechanical elements with femtowatt-level standby power consumption. *Nat. Photon.* **2023**, *17*, 1089–1096. DOI: [10.1038/s41566-023-01327-5](https://doi.org/10.1038/s41566-023-01327-5).
- [356] Zhang, L.; Dong, J.; Ding, F. Strategies, status, and challenges in wafer scale single crystalline two-dimensional materials synthesis. *Chem. Rev.* **2021**, *121*, 6321–6372. DOI: [10.1021/acs.chemrev.0c01191](https://doi.org/10.1021/acs.chemrev.0c01191).
- [357] Xu, X.; Guo, T.; Kim, H.; Hota, M.K.; Alsaadi, R.S.; Lanza, M.; Zhang, X.; Alshareef, H.N. Growth of 2D materials at the wafer scale. *Adv. Mater.* **2022**, *34*, e2108258. DOI: [10.1002/adma.202108258](https://doi.org/10.1002/adma.202108258).



- [358] Mišeikis, V.; Coletti, C. Wafer-scale integration of graphene for waveguide-integrated optoelectronics. *Appl. Phys. Lett.* **2021**, *119*, 050501.
- [359] Chang, T.Y.; Chen, Y.; Luo, D.I.; Li, J.X.; Chen, P.L.; Lee, S.; Fang, Z.; Li, W.Q.; Zhang, Y.Y.; Li, M.; Majumdar, A.; Liu, C.H. Black phosphorus mid-infrared light-emitting diodes integrated with silicon photonic waveguides. *Nano Lett.* **2020**, *20*, 6824–6830. DOI: [10.1021/acs.nanolett.0c02818](https://doi.org/10.1021/acs.nanolett.0c02818).
- [360] Huang, L.; Dong, B.; Yu, Z.G.; Zhou, J.; Ma, Y.; Zhang, Y.-W.; Lee, C.; Ang, K.-W. Mid-infrared modulators integrating silicon and black phosphorus photonics. *Mater. Today Adv.* **2021**, *12*, 100170. DOI: [10.1016/j.mtadv.2021.100170](https://doi.org/10.1016/j.mtadv.2021.100170).
- [361] Geiger, S.; Michon, J.; Liu, S.; Qin, J.; Ni, J.; Hu, J.; Gu, T.; Lu, N. Flexible and stretchable photonics: The next stretch of opportunities. *ACS Photon.* **2020**, *7*, 2618–2635. DOI: [10.1021/acsp Photonics.0c00983](https://doi.org/10.1021/acsp Photonics.0c00983).
- [362] Seo, J.H.; Swinnich, E.; Zhang, Y.Y.; Kim, M. Low dimensional freestanding semiconductors for flexible optoelectronics: Materials, synthesis, process, and applications. *Mater. Res. Lett.* **2020**, *8*, 123–144. DOI: [10.1080/21663831.2020.1718231](https://doi.org/10.1080/21663831.2020.1718231).
- [363] Yao, K.; Unni, R.; Zheng, Y. Intelligent nanophotonics: Merging photonics and artificial intelligence at the nanoscale. *Nanophotonics* **2019**, *8*, 339–366. DOI: [10.1515/nanoph-2018-0183](https://doi.org/10.1515/nanoph-2018-0183).
- [364] Midolo, L.; Schliesser, A.; Fiore, A. Nano-opto-electro-mechanical systems. *Nat. Nanotechnol.* **2018**, *13*, 11–18. DOI: [10.1038/s41565-017-0039-1](https://doi.org/10.1038/s41565-017-0039-1).
- [365] Wang, J.; Sciarrino, F.; Laing, A.; Thompson, M.G. Integrated photonic quantum technologies. *Nat. Photon.* **2020**, *14*, 273–284. DOI: [10.1038/s41566-019-0532-1](https://doi.org/10.1038/s41566-019-0532-1).
- [366] Kim, M.; Jacob, Z.; Rho, J. Recent advances in 2D, 3D and higher-order topological photonics. *Light Sci. Appl.* **2020**, *9*, 130.
- [367] Zhu, Y.; Tang, T.; Zhao, S.; Joralmon, D.; Poit, Z.; Ahire, B.; Keshav, S.; Raje, A.R.; Blair, J.; Zhang, Z.; Li, X. Recent advancements and applications in 3D printing of functional optics. *Addit. Manuf.* **2022**, *52*, 102682. DOI: [10.1016/j.addma.2022.102682](https://doi.org/10.1016/j.addma.2022.102682).